Duke University
Durham
North Carolina 27706

NEUTRON ELASTIC AND INELASTIC SCATTERING STUDIES ON ^{54}Fe, ^{56}Fe, ^{63}Cu and ^{65}Cu

by

Sadiq Mohammed El-Kadi
Department of Physics
Duke University

Date: April 10, 1981

Approved:

Richard L Walter
Richard L. Walter, Supervisor

Edward G. Bilpuch

W Pardon

Lawrence Rowan

Dissertation submitted in partial fulfillment of the requirements for the degree of Doctor of Philosophy in the Department of Physics in the Graduate School of Duke University

1981

Abstract

Physics - Nuclear

NEUTRON ELASTIC AND INELASTIC SCATTERING STUDIES ON ^{54}Fe, ^{56}Fe, ^{63}Cu and ^{65}Cu

by

Sadiq Mohammed El-Kadi
Department of Physics
Duke University

Date: April 10, 1981

Approved:

Richard L Walter
Richard L. Walter, Supervisor

Edward G. Bilpuch

W Fowler

Lawrence Cranberg

An abstract of a dissertation submitted in partial fulfillment of the requirements for the degree of Doctor of Philosophy in the Department of Physics in the Graduate School of Duke University

1981

ABSTRACT

Neutron differential elastic and inelastic scattering cross sections have been obtained for an incident neutron energy range between 8 and 14 MeV for ^{54}Fe, ^{56}Fe, ^{63}Cu and ^{65}Cu. These measurements provide cross section data for nuclear fusion reactor design.

Elastic scattering cross sections have been analysed using a spherical optical model to obtain global parameters that can predict necessary neutron elastic scattering cross sections in the mass and energy ranges of the present work. The global parameters have been used to calculate the volume integral and the rms radius of the central real potential. The matter radii as well as the neutron radii then have been deduced.

Coupled channels (CC) calculations were performed for elastic and inelastic scattering data assuming the harmonic vibrational model. The anharmonicity effect on the predictions of the cross section has been considered for ^{56}Fe by inserting the reorientation matrix element in the CC calculations. Good fits have been obtained for both elastic and inelastic scattering cross sections of ^{54}Fe and ^{56}Fe. The quadrupole deformation parameters obtained are in good

agreement with those deduced from Coulomb excitation measurements.

The coupled channels calculations for ^{63}Cu and ^{65}Cu isotopes have been carried out using the weak particle-core coupling model. The quadrupole deformation parameters obtained are comparable with the corresponding deformations for the even core nuclei.

ACKNOWLEDGMENTS

I would like to express my deep appreciation and sincere thanks to my advisor, Dr. Richard L. Walter, for his patience, kind assistance and supervision of this study. Special thanks and appreciations go to Dr. F. O. Purser for his advice through out the course of this study, for his support and for paying special interest on checking this text. I would like also to thank TUNL Director Dr. E. G. Bilpuch for giving me the opportunity to work with time-of-flight program and for giving me the assistantship that in part allowed me to complete this work.

I would like to express my thanks to Dr. C. R. Gould, Dr. C. E. Nelson, Dr. H. H. Hogue, Dr. R. C. Byrd and Dr. G. Glendinning for many helpful discussions and advice. I would like to thank Dr. J. P. Delaroche for his guidance in performing coupled channel calculations. Special thanks go also to Dr. A. Beyerle for his assistance in performing the measurments and for his valuable discussion and assistance in scripting this dissertation. My thanks go also to R. Pedroni for his assistance in taking the data and stripping some of it. Dr. L. W. Seagondollar and P. Thambidurai's assistance in taking the data are also appreciated. I would like to thank also Mrs. Dorthy(Mike) Bailey for drawing the figures and to Carey Floyd for photographing some of them.

I would like also to thank all the faculty, staff and graduate students in the physics department and TUNL who have been in any way given help before and during this work, especially Dr. R. Roberson and Dr. L. Evans.

My thanks also go to the Libyan people for their support before and during most of this work. I am in great debt to my wife Kameela and to my children for their patient understanding and love. My thanks and appreciation go to my brother and my parents for their continous support and patience.

Above all, my thanks to Allah for giving me the strength and the pacience to over come very serious difficulties I have faced.

This work was supported in part by the U.S. Department of Energy.

CONTENTS

LIST OF TABLES

List of Figures

Chapter I

INTRODUCTION

The neutron time-of-flight project at the Triangle Universities Nuclear Laboratory (TUNL) is an important program for supplying neutron data requirements for the magnetic fusion energy program of the U.S. Department of Energy. Prior to 1978 studies at TUNL concentrated on nuclei in the p-shell for neutron energies between 8 and 15 MeV (Hogue 1977 and Glendinning 1980) and consisted primarily of elastic scattering and iuelastic scattering to discrete states in the residual nucleus.

In 1978 the program was extended to cover elastic scattering and inelastic scattering to discrete states for a range of medium weight nuclei. The present work reports measurements of elastic and inelastic neutron cross sections for ^{54}Fe, ^{56}Fe, ^{63}Cu and ^{65}Cu at 8, 10, 12 and 14 MeV. The TUNL neutron time-of-flight program was extended further to include measurements of continuum neutron emission spectra for incident neutron energies between 7.5 and 12 MeV (Beyerle 1979). Both of these sets of measurements will provide cross-section data for elements that will be important constituents of the containment vessels, magnet coils, the heat transfer blanket, and auxiliary equipment associated

with a working fusion reactor designed to convert nuclear energy into a useable energy source.

A few neutron cross-section measurements exist at 8 and 14 MeV for natural iron, natural copper and ^{56}Fe (Holmqvist et al. 1970 and Leshchenko et al. 1972). The availability of precise neutron scattering data offers the opportunity to test various optical model parameter sets which have been proposed. The present data also provide a test of the adequacy of the isospin formulation both from the standpoint of comparisons with proton data and by the virtue of the isospin studied in this work.

The elastic scattering cross-section data in the present work were fitted with spherical optical model. The data were found to be sensitive to the spin-orbit parameters. This led to determining the spin-orbit parameters as well as the other optical model parameters by searching on each data set for each nucleus separately. Eventually global optical model potential parameters, resulting from fitting all the elastic data in the present work at once, were obtained. Results of the optical model analysis provide reasonable parameters to allow necessary data to be calculated for neutron energies in the vicinity of those of the present measurement. The rms radii of the central potentials were obtained for the isotopes of the present work from the geometry of the global set. The matter rms radii were then deduced and compared with previous work.

The neutron cross-section data reported in the present work will provide pre-requisite input for the neutron polarization studies which are underway at TUNL (Floyd 1980). These combined studies will provide a critical test of the spin-orbit parameters resulting from the present work.

Inelastic scattering data were obtained for scattering to the first excited state of ^{54}Fe and ^{56}Fe and to the combined group representing first- and higher-excited states of ^{63}Cu and ^{65}Cu . The accuracy of this data is poorer in quality than that for elastic scattering, and the accuracy decreased as the energy increased from 8 to 14 MeV because the relative separation of the states decreased and the background intensity increased.

The phenomenological coupled-channel (CC) formalism utilizing the harmonic vibrational model has been used to fit the elastic as well as inelastic scattering to first 2^+ state for ^{54}Fe and ^{56}Fe . The fits achieved were reasonably good. The quadrupole deformation parameters(β_2) obtained in the present work are comparable to those obtained from Coulomb excitation (CE) measurements. (LeVine et al. 1981)

An anharmonic vibrational picture for ^{56}Fe has also been considered in the present CC analysis by inserting the reorientation matrix element obtained from the measured values of the quadrupole moment $Q(2^+)$.

The data obtained from the Cu isotopes were also analysed using the same CC formalism in which the weak core particle coupling has been assumed. Good fits are also obtained and the β_2 deformation parameters were found to be in fair agreement with corresponding values obtained from CE measurements for the neighboring Ni isotopes.

The deformed potential parameterization obtained from the present work was used to predict the total cross sections (σ_T) for Fe and Cu isotopes in the energy region between 0.01 and 14.0 MeV. The results of these calculations are in good agreement with the experimental σ_T values. In addition the scattering radius (R') and the s-wave strength function (S_0) are calculated at 100 keV. The results of these calculations are in good agreement with corresponding available data except for ^{54}Fe in which the comparison of the strength functions is inadquate because of the nonstatistical structure in the neutron widths.

Chapter II

EXPERIMENTAL PROCEDURE

The data on the present work have been acquired using the TUNL Cyclo-graaff installation (figure 1) which has been discribed else where (Newson et al. 1974) and the Neutron Time-of-Flight facilities. The negative ion beam originates at the direct extraction negative ion source (DENIS 2), which is capable of producing about 85 μA d.c. of negative deuterium beam. Prior to injecting the beam into the FN Tandem Van de Graaff accelerator, the beam is chopped by passing through a standard High Voltage Engineering Corporation radio frequency chopper which sweeps it across a 0.375 inch diameter aperature at a frequency of 2 MHz. An auxiliary chopper is used to remove the retrace pulses. The chopped beam is then bunched by a two-gap klystron buncher to bursts of about 2 ns FWHM at the target. The accelerated positive beam is deflected by a 20^0-70^0 bending magnet through an angle of 38^0 , and transported to the time-of-flight target area to a deuterium gas cell via an all metal and ceramic beam line which is maintained at vacuum of approximately 10^{-7} Torr by combination of diffusion pumps, a titanium sublimation pump, and liquid nitrogen traps.

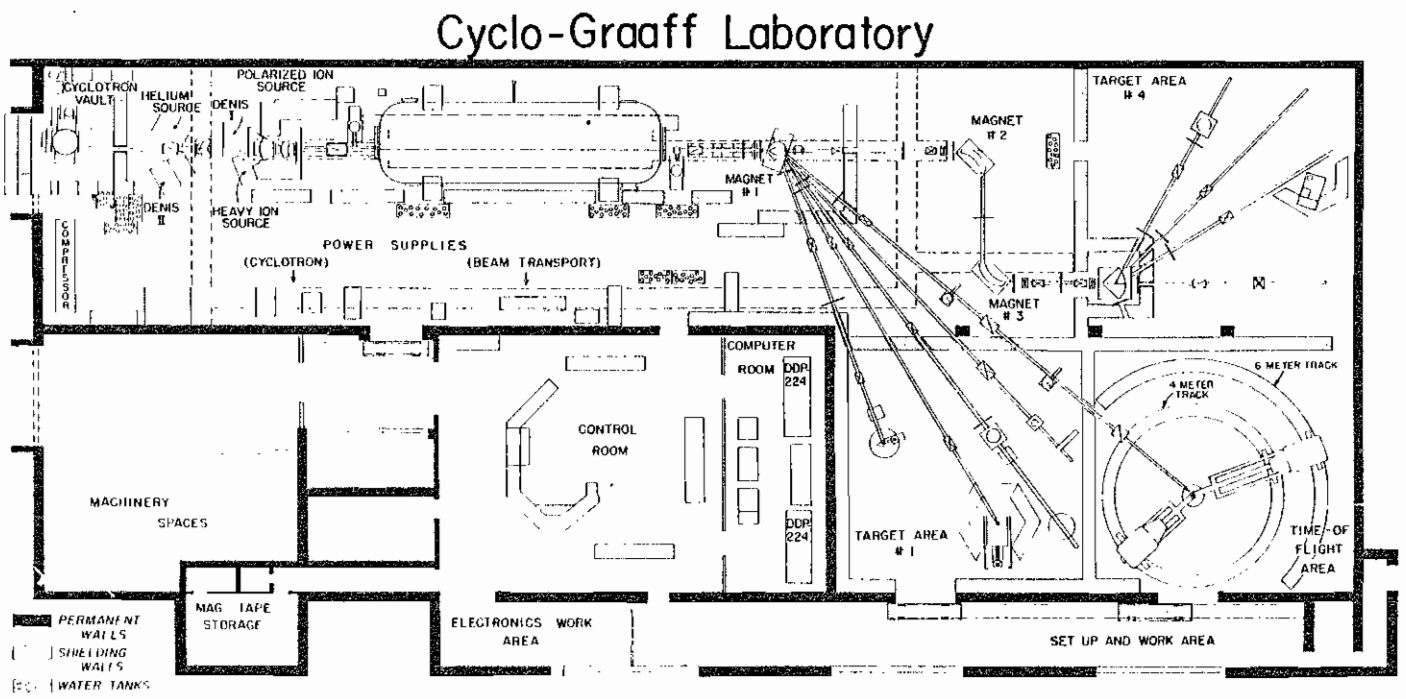

Figure 1 Floor plan of the Cyclo-Graaf accelerator laboratory.

Source neutrons were obtained from $^{2}H(d,n)^{3}He$ reaction using 3 bar high purity deuterium gas in a 2.92 cm long and 0.86 cm in diameter gas cell (figure 2) which was constructed of 0.045 cm thick stainless steel wall. To minimize the production of neutrons from other than target deuterium gas, a 0.031 cm tantalum cell liner and a 0.051 cm tantalum beam stop were used. The beam entrance window was made of 5.8 mg/cm2 Havar foil.

2.1 TIME-OF-FLIGHT SPECTROMETER

The time-of-flight (TOF) facility has been described in several publications (Hogue 1977, Glendinning 1980 and Seagondollar 1979). Briefly, it consists of two main detectors, a ceiling monitor detector and a zero degree monitor detector. One of the two main detectors is 2 inch thick by 3.5 inch diameter NE218 liquid scintillator coupled to a Philips 58DVP photomultiplier surrounded by a massive (4700 kg) shield of copper, lead and paraffin loaded with lithium carbonate. The collimator is a double truncated cone designed to permit the detector to view as little as possible of the volume surrounding the sample while viewing the sample completely. The double truncated cone design also allows one to minimize neutron scattering from the collimator walls (Glasgow 1974). The second main detector is similar to the described one except it is slightly larger (5 inches in diameter). The shield has 30 cm more material in the back of the

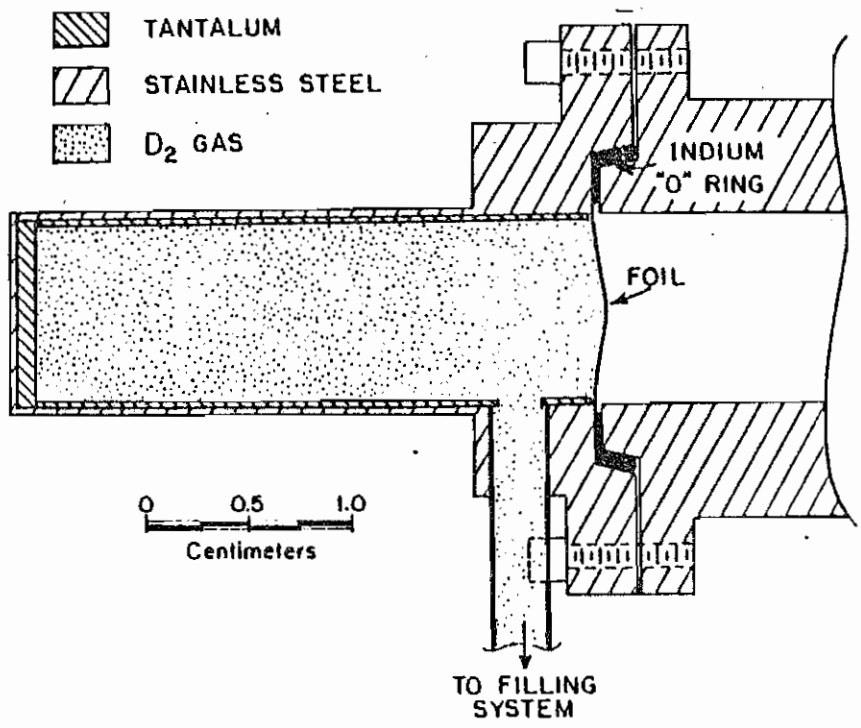

Figure 2 NTOF deuterium gas cell.

detector to reduce neutron background from wall scattering. Figure 3 is a schametic diagram of this detector and sheild.

Detector angles are measured by vernier scales accurate to aproximately 2' of arc. A geared-down one-half hp electric drive is located under each carriage to position either detector at any desired angle electrically.

Both detectors are used with a massive tungsten shadow bar positioned so that it shields the detectors from direct source-neutrons. The shadow bars were mounted on a stand in such a way that during the experimental run, the shadow bar position is determined by the angular position of a sprocket shaft which is calibrated vs. scattering angle. Figure 4 shows schematic diagram of the two main detectors with the geometry of the shadow bars and the pre-shielding to prevent detection of the direct source-neutrons.

The ceiling monitor detector is a 2-inch diameter by 2-inch thick NE218 scintillator with Phillips 56DVP photo tube and is provided with 50 kg copper shielding. The detector is mounted about 2.5 meters above the reaction plane at about 60^0 and views the neutron source directly. The yield of the $^2H(d,n)^3He$ group in this detector is used for normalizing different runs to one value of the incident flux of neutrons. That is, this yield is the primary relative measurement of the integrated neutron flux at the sample during counting intervals for the main detectors.

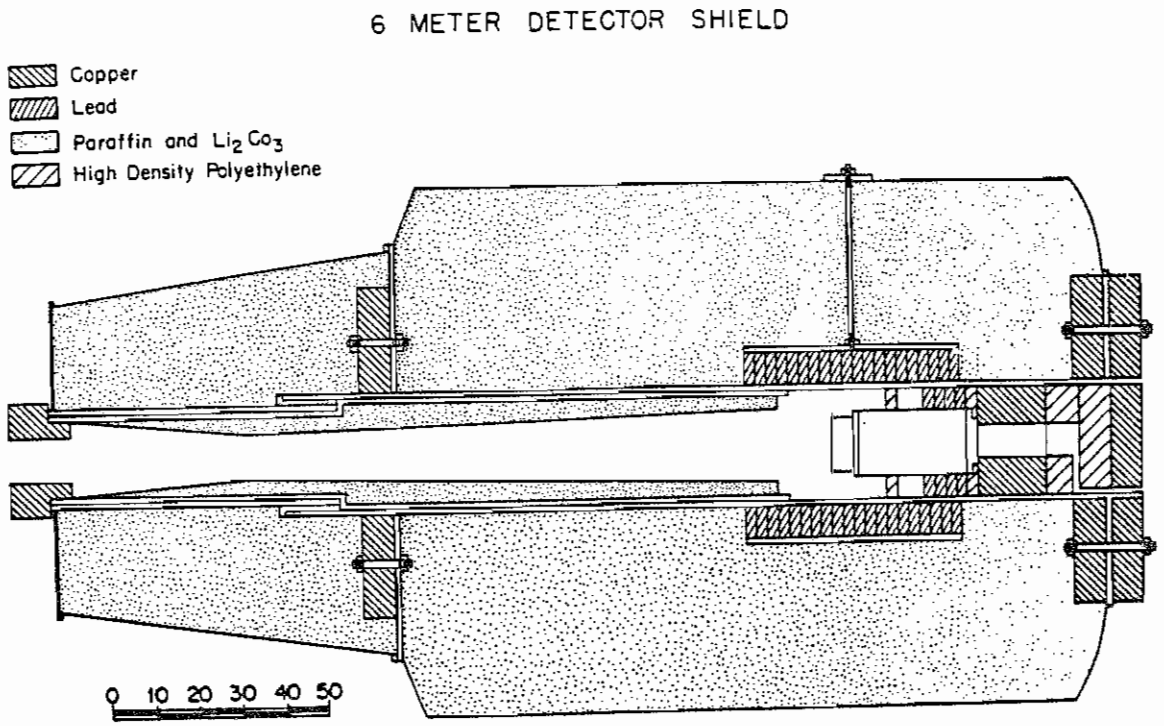

Figure 3 Cross section view of the 6-m neutron detector and its shielding.

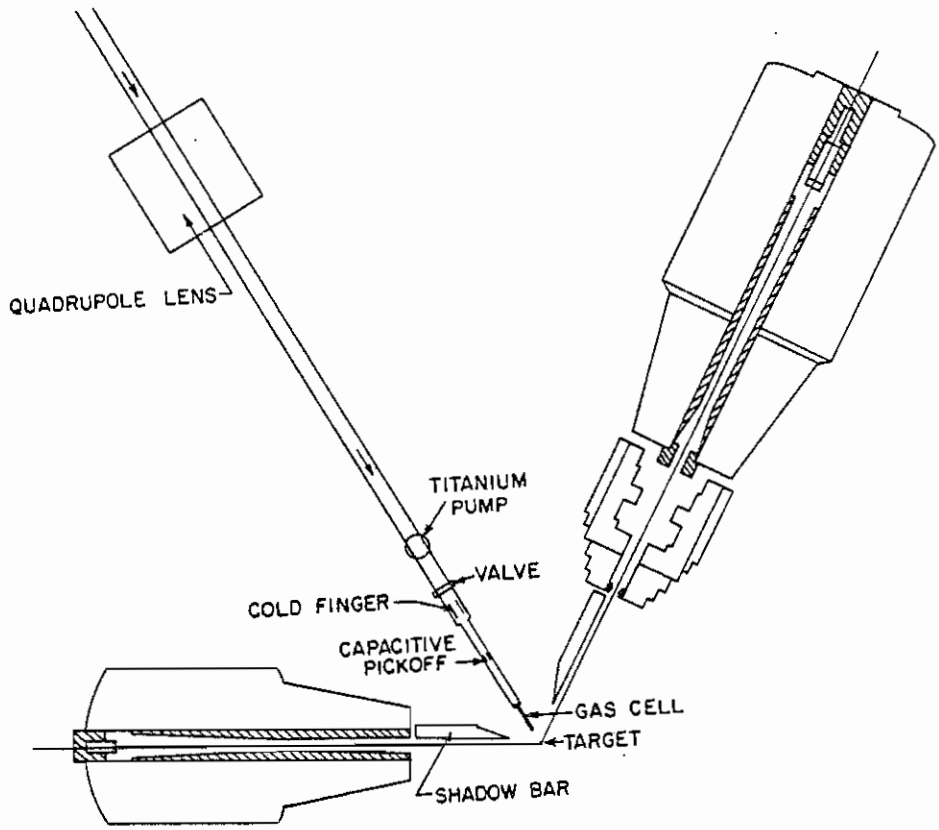

Figure 4 Schematic diagram of the geometry of the two main neutron detectors and their shadow bars.

The zero degree monitor detector is located along the axis of the incident deuteron beam and about four meters from the gas cell. The detector is a 2-inch diameter by 2-inch thick NE218 scintillator coupled to an RCA 8575 photomultiplier tube. The detector at zero degrees is used to determine the minimuum burst width during adjustment of the electronic timing and to monitor the change in the timing during the experiment.

2.2 ELECTRONICS

The electronic circuity used for taking the data of the present work is discussed in detail elsewhere (Beyerle 1980), and will be described briefly in this section. A block diagram of the electronic circuitry for one of the detectors used for taking the data of the present work is shown in figure 5. There are four essentially identical set-ups for the two main detectors and the two monitors.

A fast signal from the detector photomultiplier is used for both linear and pulse-shape-discrimination (PSD) signals. A linear signal is passed through an ORTEC 490B, and then through an ORTEC 427 delay amplifier. The single channel analyzer of the ORTEC 490B is used for setting the bias level of the experiment. A Canberra 1428 constant fraction discriminator (CFD) strobes the PSD and provides the start signal for a Canberra 1443 time to amplitude converter (TAC). The stop signal of the modules comes from the PSD

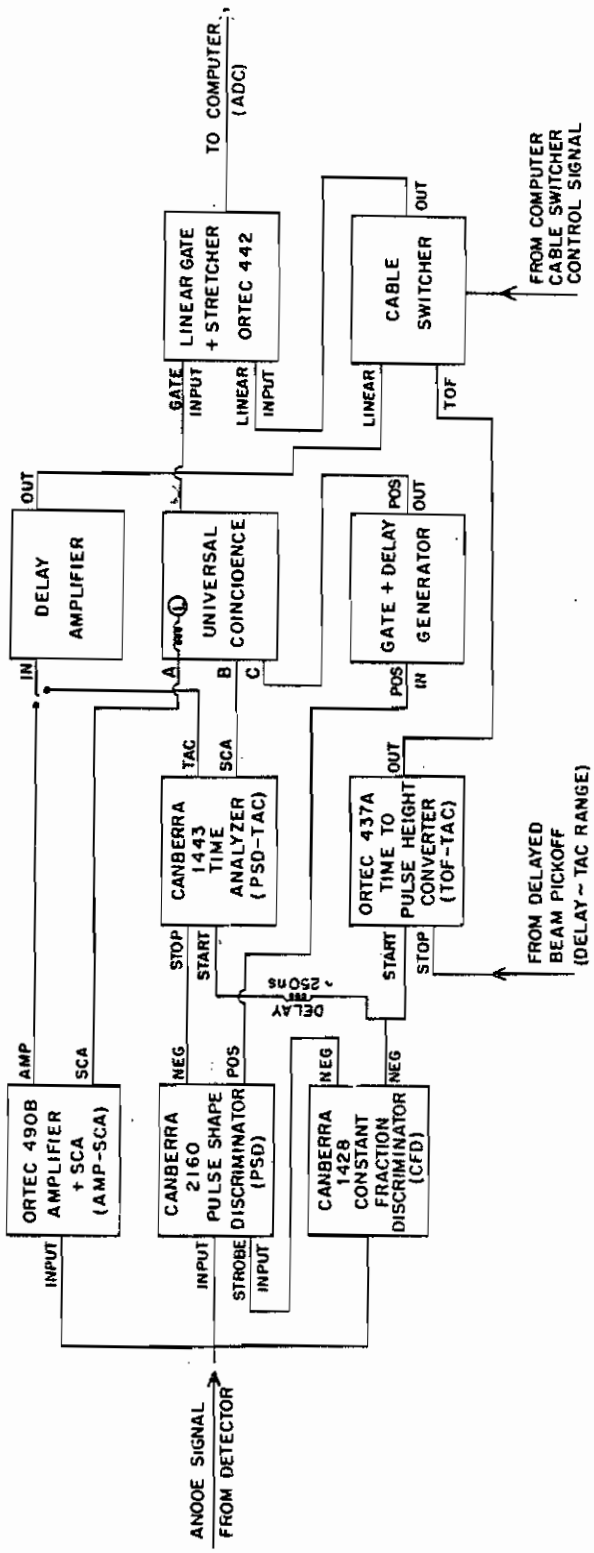

Figure 5 Block diagram of the electronics for one of the main detectors.

unit which is operated in the n+γ mode, with its SCA output used to select neutron and/or gamma ray events. The fast detector signal serves as the start signal for another time to amplitude converter, ORTEC 437A, which provides the neutron TOF signals. The stop signal is derived from a capacitive beam pulse pick-off unit. Any of the three signals, neutron TOF, neutron PSD or linear neutron energy signal can be gated through to an analogue-to-digital converter (ADC) subject to the logic requirements established in the ORTEC 418A universal coincidence unit.

Figure 6 is a pulse-height distribution from the Canberra 1428 PSD unit obtained at a bias of about 2 MeV equivalent neutron energy. As can be seen, neutron induced proton recoil events are well separated from events produced by gamma rays.

2.3 DETECTOR EFFICIENCIES

Prior to accumulating the present data set, a new detector and shield were added to the time of flight facility. In addition, the electronic set up was modified to incorporate Canberra Model 2160 pulse-shape discrimination modules whose greater dynamic range was required for proposed low bias (<500 keV) measurements of continuum neutron emission spectra. As a result of these changes, new efficiency determinations were required for both of the main neutron detectors used in the present work.

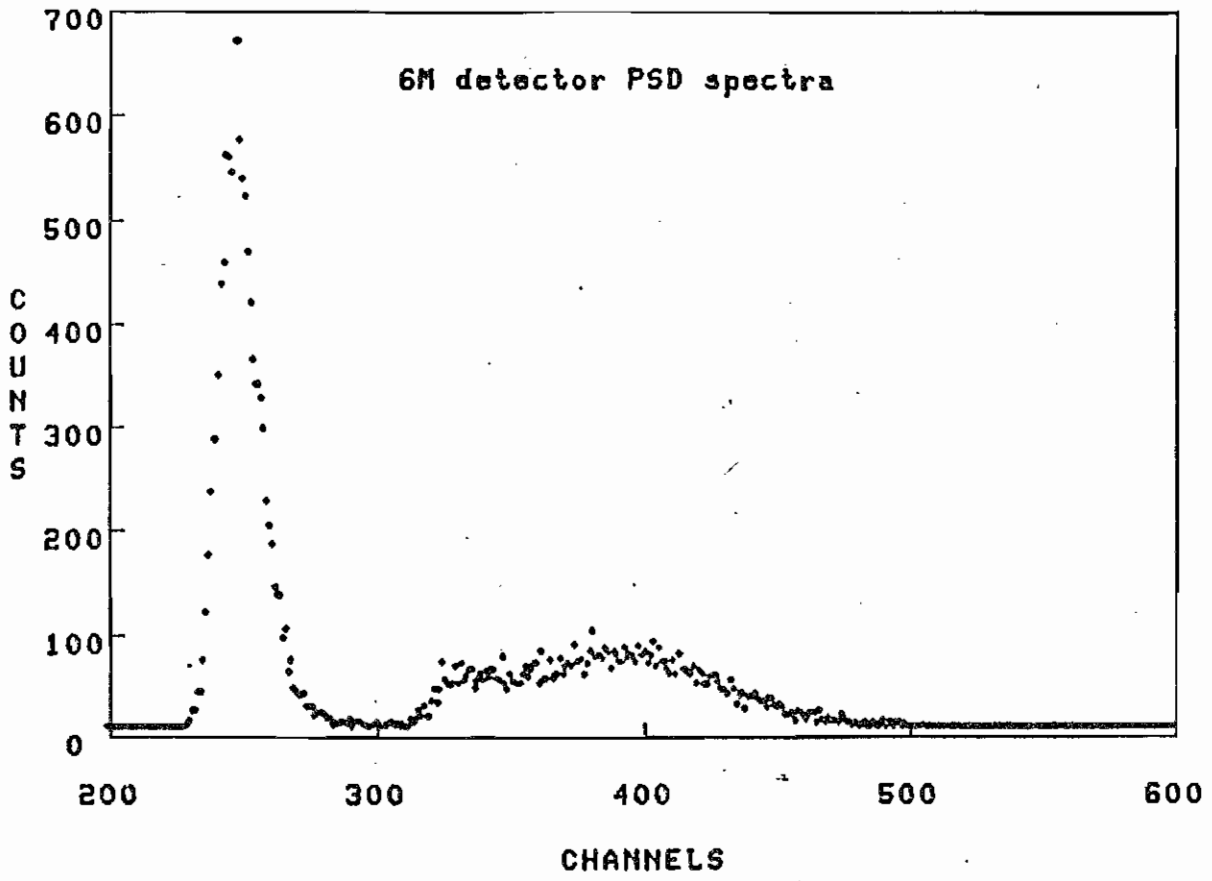

Figure 6 Pulse-height distribution of the PSD unit, the broad peak is from neutron events and the sharp peak is from gamma-ray events.

The detector efficiencies were determined in the same geometry used in the scattering studies so that shielding, collimation, and air column attenuation effects would be implicitly included. The efficiencies for two bias settings were determined by measuring the response functions of the detectors to monoenergetic neutrons produced in $^{2}H(d,n)^{3}He$, $^{3}H(p,n)^{3}He$ and $^{3}H(d,n)^{4}He$ reactions. Angular distributions were measured for two incident deuteron energies of 6.0 and 10.0 MeV for the $^{2}H(d,n)^{3}He$ reaction to cover the energy range from 2.0-13.0 MeV, and a $^{2}H(d,n)^{3}He$ 0^{0} excitation function was used to extend the range to 16.8 MeV. Angular distributions were measured for $^{3}H(p,n)^{3}He$ neutron source reaction at incident proton energies of 2.5, 5.0, and 10.0 MeV. The overlapping data sets spanned the neutron energy range from 300 keV to 16.8 MeV. The energy range was extended to 28.0 MeV by measuring angular distribution data from $^{3}H(d,n)^{4}He$ reaction at a deuteron energy of 10.0 MeV. The $^{2}H(d,n)^{3}He$ cross-section data as well as the 5.0 and 10.0 MeV cross-section data for $^{3}H(p,n)^{3}He$ were taken from (Drosg 1978). The cross-section data for $^{3}H(p,n)^{3}He$ neutron source reaction at 2.5 MeV and for $^{3}H(d,n)^{4}He$ reaction at 10.0 MeV were taken from Liskien and Paulsen (Liskien et al. 1973). The Legendre polynomial coefficients which are tabulated in these references were used to obtain laboratory cross-section tables.

In order to perform the efficiency measurements, the following minor changes were required in the experimental arrangement used in the scattering studies:

1. Shadow bars were removed.

2. An extender was inserted in the beam pipe to position the gas cell on the axis of rotation of the detectors

The monitor detector was used only as a check since data were normalized to integrated beam current.

The experimental procedure was similar to that employed in the scattering runs. The two time-of-flight spectra were simultaneously recorded for each of the two detectors, one with a neutron energy bias of aproximately 2.0 MeV, set at half-height of the Compton recoil edge of the 0.66 MeV ^{137}Cs gamma ray, and the other with a neutron energy bias of about 0.3 MeV, set at the minimum between the 26 and 59 keV gamma-ray peaks from ^{241}Am. These bias settings were carefully monitored during the course of the measurements. Spectra were taken for angles chosen to scan the energy range in about 400 keV steps. Three neutron source spectra are shown in figure 7. The top spectrum is from the $^{3}H(p,n)^{3}He$ reaction at an incident proton energy of 6.0 MeV at a laboratory angle of 45^{0}. The middle spectrum in the figure is that of $^{2}H(d,n)^{3}He$ at an incident deuteron energy of 10.0 MeV and at laboratory angle of 40^{0}. The bottom spectrum in the figure

is the spectrum of $^{3}H(d,n)^{4}He$ at a deuteron energy of 10.0 MeV for neutrons detected at 40^{0}. These spectra, as in the scattering experiments to be described later, were analyzed following the procedure for treating difference spectra. The mono-energetic peaks were summed using an off-line code which permitted fitting the small, underlying background to a smooth function. The areas-vs.-angles obtained were converted to efficiencies-vs.-energies as follows:

$$\eta(E_n) = \frac{Y(\theta)\Omega^{-1}}{Nn\sigma(\theta)}$$

where $Y(\theta)$ is the yield,

Ω is the solid angle subtended by the detector and

N is the number of incident particles.

n is the number of target gas per cm^2 .

$\sigma(\theta)$ is the cross section of the reaction being measured.

Several variables can be re-expressed in terms of the quantities that can be obtained at TUNL (Byrd 1978), and the above expression reduced to

$$\eta(\theta) = \frac{Y(\theta) \cdot flp^2 \cdot (273.2 + T)}{40.049 \cdot \sigma(\theta) \cdot BCI \cdot S \cdot nt \cdot D^2 \cdot L \cdot (14.7 + P)}$$

where flp is detector flight path in meters,

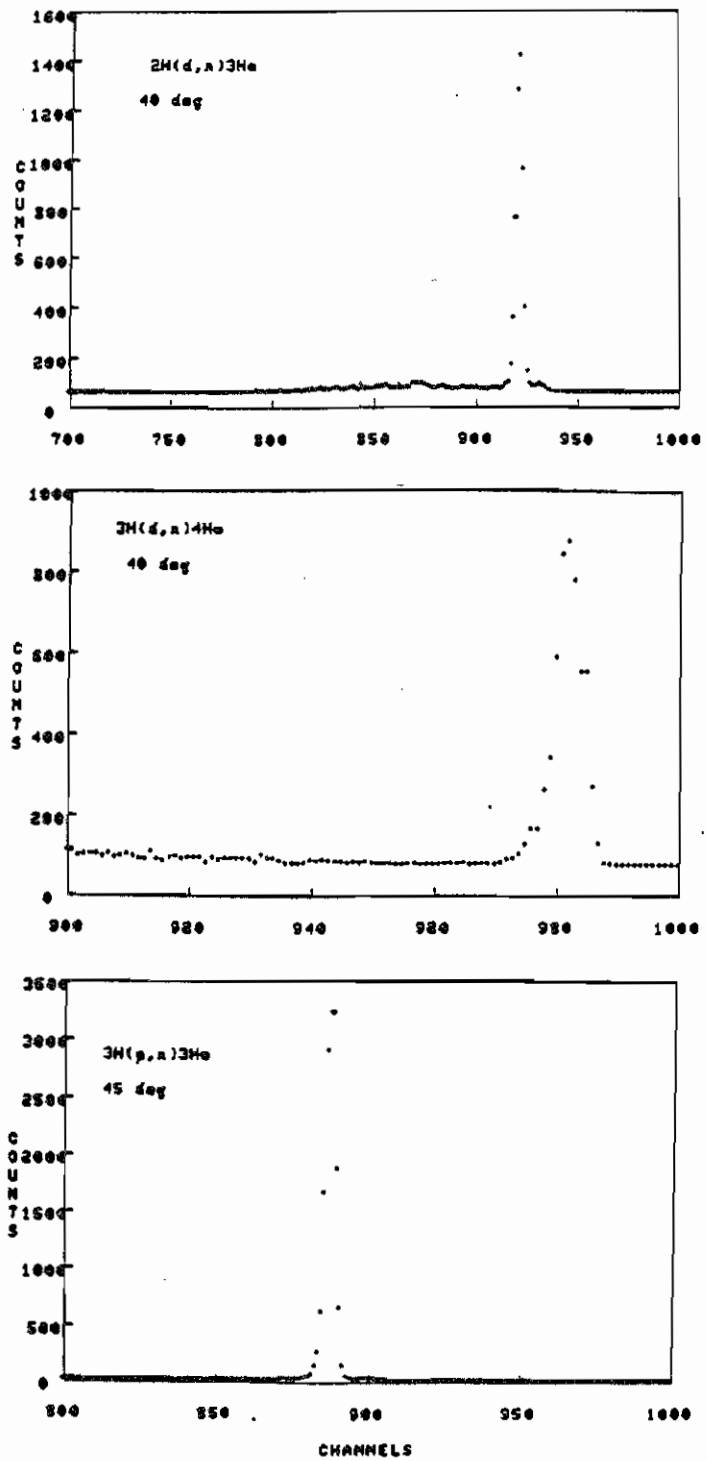

Figure 7 Neutron source spectra from the three source reactions used in the efficiency measurements (see text).

T is temperature (deg centigrade)

$\sigma(\theta)$ is cross section in mb/sr

S is beam current integrator scale in :A

BCI is the number of pulses from the beam current integrator module

nt is number of atoms per molecule

D is detector diameter (inch)

L is the gas cell length (inch)

P is the pressure of the gas in the gas cell (gauge reading) in lb/in^2.

The overlapping efficiency values obtained from $^2H(d,n)^3He$ reaction were found to be self consistent while the efficiency values derived from the $^3H(p,n)^3He$, and $^3H(d,n)^4He$ were consistently below that obtained from the $^2H(d,n)^3He$ data. This discrepancy was attributed to contamination of the tritium gas by hydrogen. The contamination was estimated by normalizing the efficiency values obtained from the neutron source reaction $^3H(p,n)^3He$ to the $^2H(d,n)^3He$ efficiency values and was found to be $(17.2\pm1.0)\%$.

Additional spectra were taken for one angle at differing flight paths to study the neutron attenuation in sample-to-detector air columns. The efficiency data were found to be the same within the assigned errors discussed below. This indicates that effects of neutron attenuation in the sample-to-detector air column are negligible in the TUNL time-of-flight system. Calculations for the attenuation in the air (assumed to be 100% nitrogen) confirm this conclusion.

Since we did not see any pronounced structure in the efficiency curves for either bias setting, smooth fits to the data were made using an expression similar to the one given by Drosg (Drosg 1972) with only a slight modification. The data were fitted to the following formula:

$$\eta(E) = F \cdot P$$

where $F = E_1(1 - e^{D\sigma(E)}) \cdot \{1 + B/E_2[1 - e^{1/2(D\sigma(E_2))}]\}$.

Here B and D are adjustable parameters given by:

$$E_1 = (E-B)/E$$

$$E_2 = E-B/2$$

Furthermore,

σ is the total cross section of the hydrogen

$$P = \sum_{i=0}^{n} A_i E_i$$

E is the neutron energy.

Three coefficients were found to be sufficient to fit the high bias data, while six or seven coefficients were needed to fit the low bias data. Some of the measured efficiency points for high bias and low bias for each of the two detectors as well as the fits to these points are shown in figure 8 and 9.

The errors on the efficiency data that were calculated included counting statistics, estimated errors from background subtraction, and estimated errors for the source cross sections. As a final check, the ratio of low- to high- bias efficiencies was measured at several energies by using the ratio of the yields from $^{1}H(n,n)^{1}H$ obtained from an auxiliary scattering experiment and was found to be consistent with the ratio of the efficiency curves at those points.

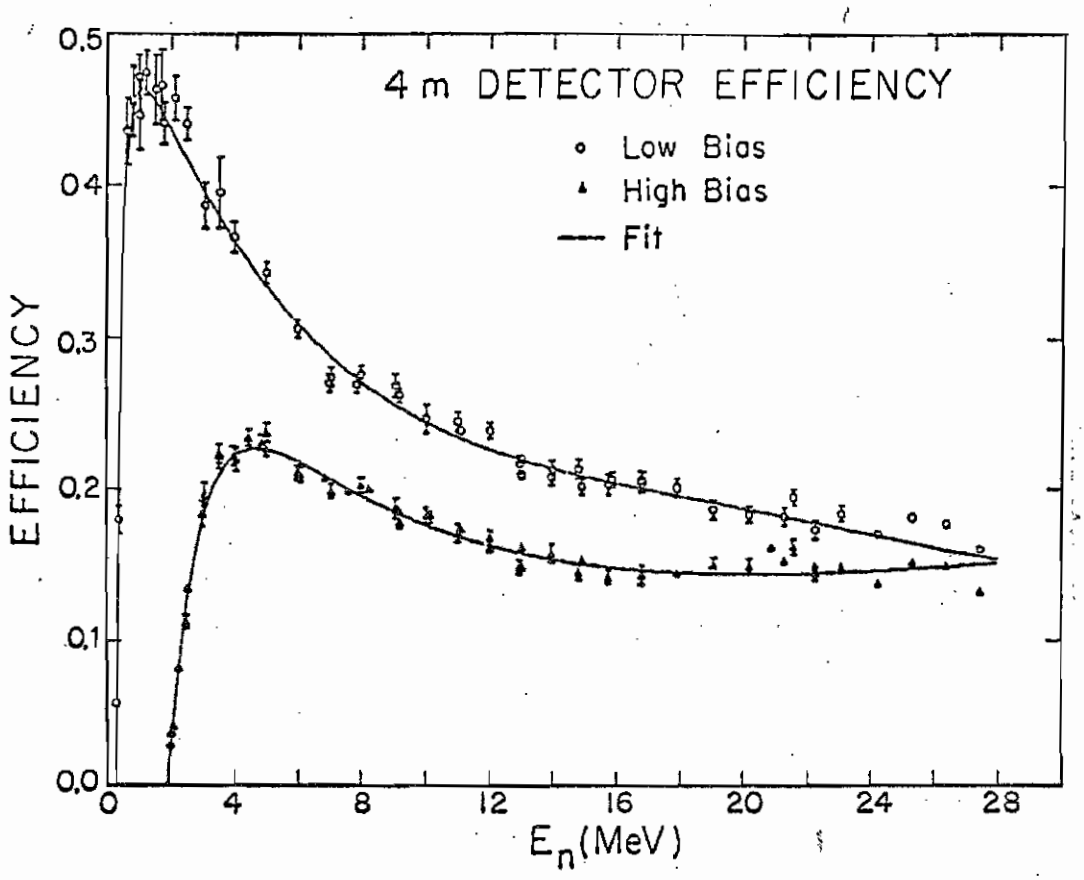

Figure 8 Low bias and high bias efficiency points for 4-m detector. The open circles are the low bias efficiencies points.

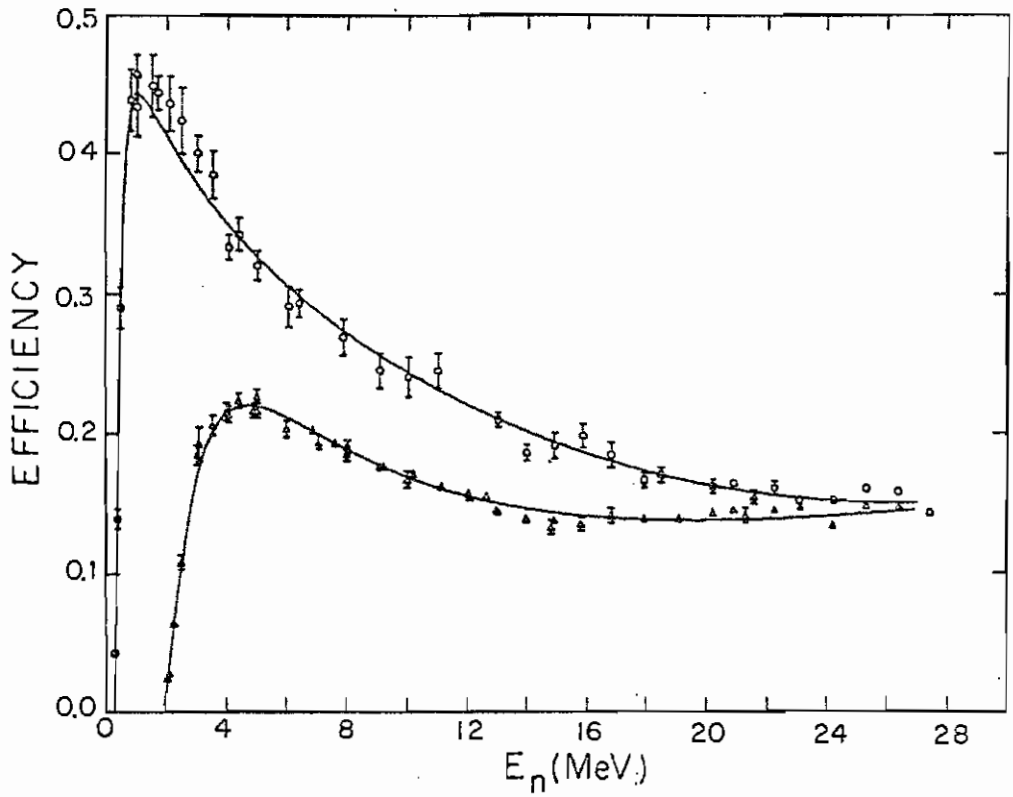

Figure 9 Low bias and high bias efficiencies for 6-m detector. Same symbols as the previous figure.

2.4 SCATTERING SAMPLES

The samples used in the present work were in the form of right circular cylinders. The physical data of these samples are given in table 1.

TABLE 1

Scattering sample properties

Sample	Radius (cm)	Height (cm)	Mass (gm)	Purity (%)
^{54}Fe	0.95	2.40	50.9	97.6
^{56}Fe	0.95	2.91	63.4	99.9
^{63}Cu	1.00	2.97	82.1	99.9
^{65}Cu	1.00	2.94	84.6	99.7
^{12}C	0.95	2.37	2.92	98.9
Polyethylene	0.72	1.16	3.41	--

The four scattering samples considered here are mounted in a chain of 'modules' which are connected to a steel cable of 0.4 mm diameter. This cable goes over precisely located upper and lower pulleys. The portion of the cable that goes over the upper pulley is attached to a one kg weight. The lower portion makes a 90^0 turn and goes to a 2.5 cm diame-

ter brass drum which is mounted on a shaft of a stepping motor. The cable makes about 6 turns around the drum and then goes to another one kg weight. Each sample was positioned vertically using a manual control of the driving circuit.

2.5 EXPERIMENTAL PROCEDURE

Data were accumulated using the 4-m and the 6-m detectors simultaneously. The flight paths of the two detectors were set at the maximum permissible, 3.711 meters and 5.670 meters. For each angle the four samples and a bare wire are measured as one set. The measurements were performed at the four energies 7.96, 9.94, 11.93, and 13.92 MeV, at angles from 30^0 to 155^0 in 5 degree increments. At 7.96 and 11.93 MeV odd angle data were taken using 4-m detector and the even angle data were taken by 6-m detector. For 9.94 MeV and 13.92 MeV the 6-m detector was used for measuring the forward angle data and the 4-m detector for measuring the back angle data, typically from 95^0 to 155^0. For each set, a 'sample-in' spectrum was taken and then a 'sample-out' taken with the bare of wire in place of sample. The next three samples used this same 'sample-out' background run. To minimize accelerator time, no measurements were taken with the deuterium gas removed from the cell. The data taking runs typically require about 2 hours to complete a four-sample set. Priority was placed on obtaining a certain minimum statistics on the elastic scattering data. At forward angles

the counting time could be reduced, but at the resulting expense of getting poor statistics on the inelastic data.

At least two polyethylene spectra were taken during the course of each angular distribution measurement. The detectors were placed at angles chosen to give maximum kinematic separation of the hydrogen peaks from that of carbon. The out count for polyethelene was taken using a carbon sample. Figure 10 shows a time-of-flight spectrum for a neutron energy of 10.0 MeV at 32^0. The middle peak is the hydrogen scattering group while the carbon elastic and inelastic to the 4.4 MeV state appears on the left and right of the hydrogen peak, respectively. The separation worsens as the neutron energy increases but the resolution is still sufficient at 14 MeV to obtain reliable normalization following the Monte Carlo calculations discribed below.

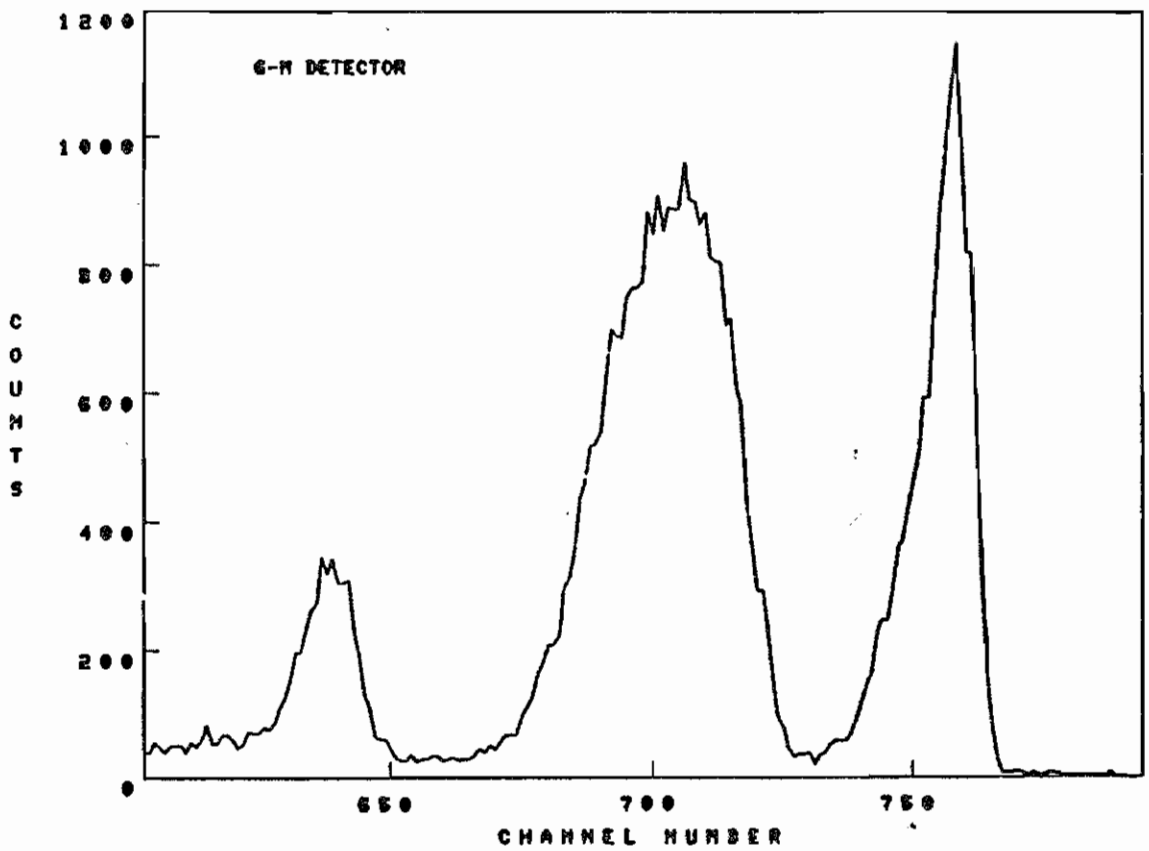

Figure 10 Time-of-flight spectrum for 10.0 MeV neutrons scattered by polyethylene at 32^0 .

Chapter III

DATA REDUCTION

The standard steps employed to derive differential cross section from measured time-of-flight spectra for the present work are described in this chapter

3.1 DIFFERENCE YIELDS

The neutron time-of-flight code NTOFA is used on the off-line TUNL computer to generate a neutron difference spectrum from the measured spectrum of the scattering sample and the associated wire spectrum. These spectra are stored on magnetic tape during the experiment. The expression used to generate the neutron difference spectrum is:

Diff = Bias + 'Sample in'counts -

FACC . 'sample out'counts/DTIN

where

Diff = the neutron difference spectrum

Bias = An arbitrary number of counts added to each channel of the spectrum to facilitate computer background subtraction

DTIN = fractional main detector live-time for the 'sample in' run

FACC = Ymon . (DTI . DTMO.)/(DTO . DTMI)

where

Ymon is the ratio of monitor detector yields obtained during 'sample in', and 'sample out' runs

DTI is main detector live-time during the sample in run

DTO is main detector live-time during the sample out run

DTMO is monitor live-time during the sample out run

DTMI is monitor live-time during the sample in run

Time-of-flight difference spectra for ^{54}Fe and ^{65}Cu at the angles of 30, 70 , and 150 degree for 8 MeV and 14 MeV are shown in figures 11 - 14.

In order to completely remove the background due to neutrons produced by deuterons interacting with the tantalum

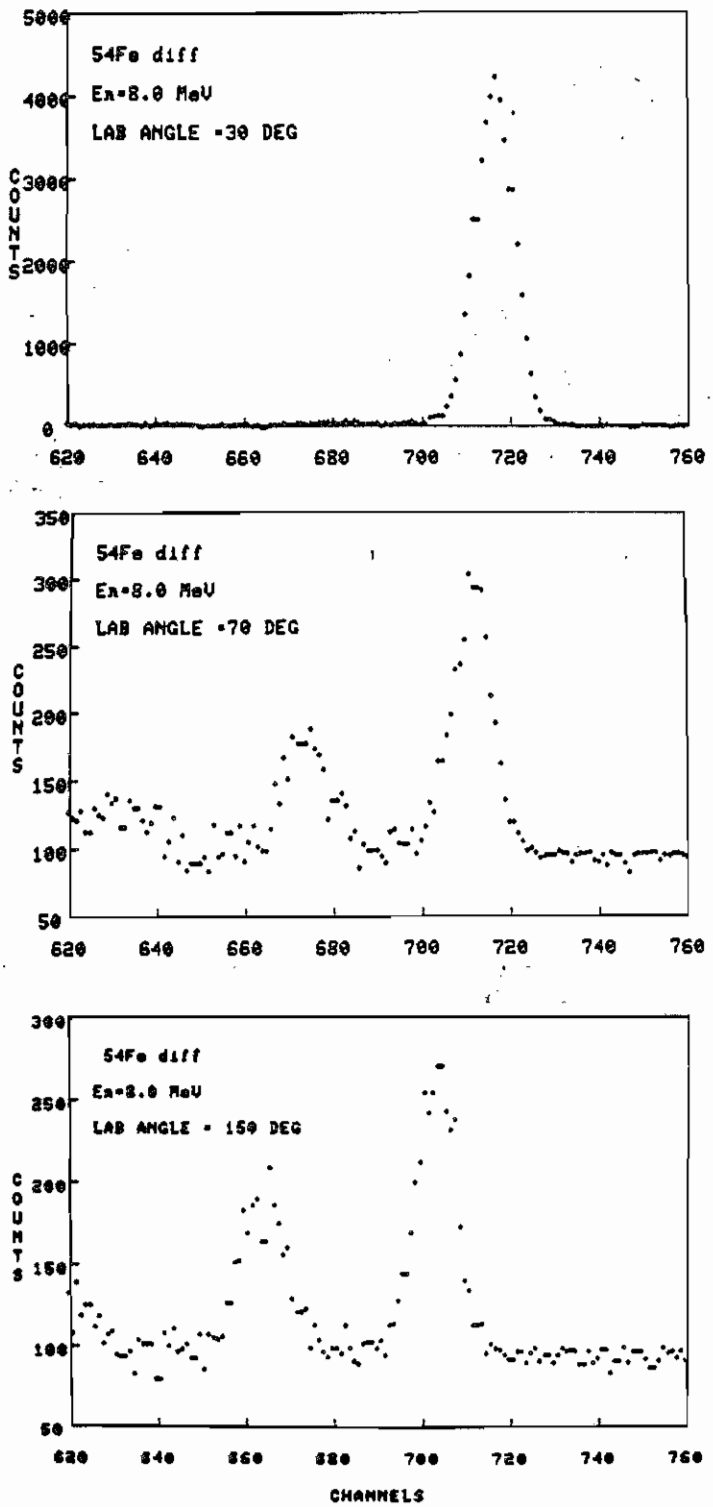

Figure 11 Neutron difference spectra for 8 MeV ^{54}Fe at 30^0, 70^0, and 150^0 (see section 2.5).

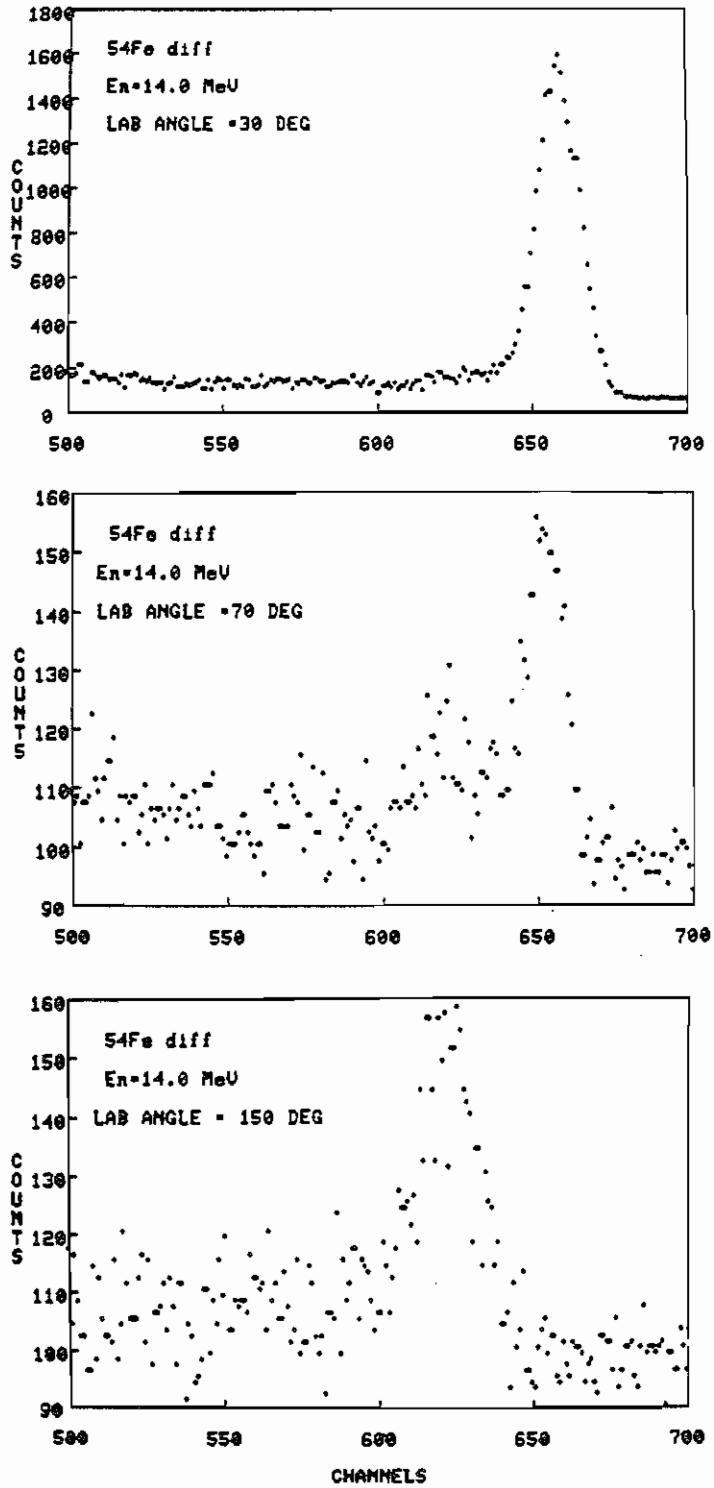

Figure 12 Neutron difference spectra for 14 MeV ^{54}Fe at 30^0, 70^0, and 150^0 (see section 2.5).

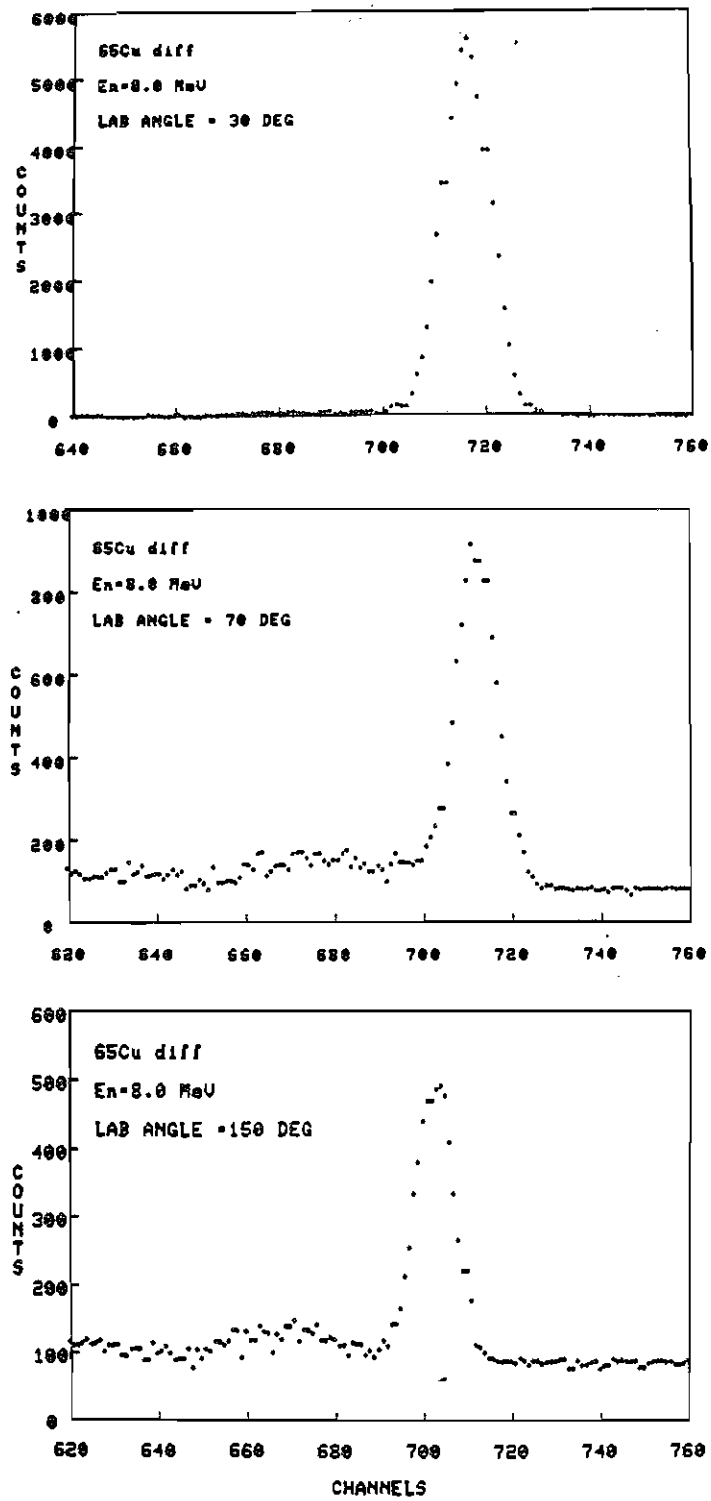

Figure 13 Neutron difference spetra for 8 MeV ^{65}Cu at 30^0, 70^0, and 150^0 (see section 2.5).

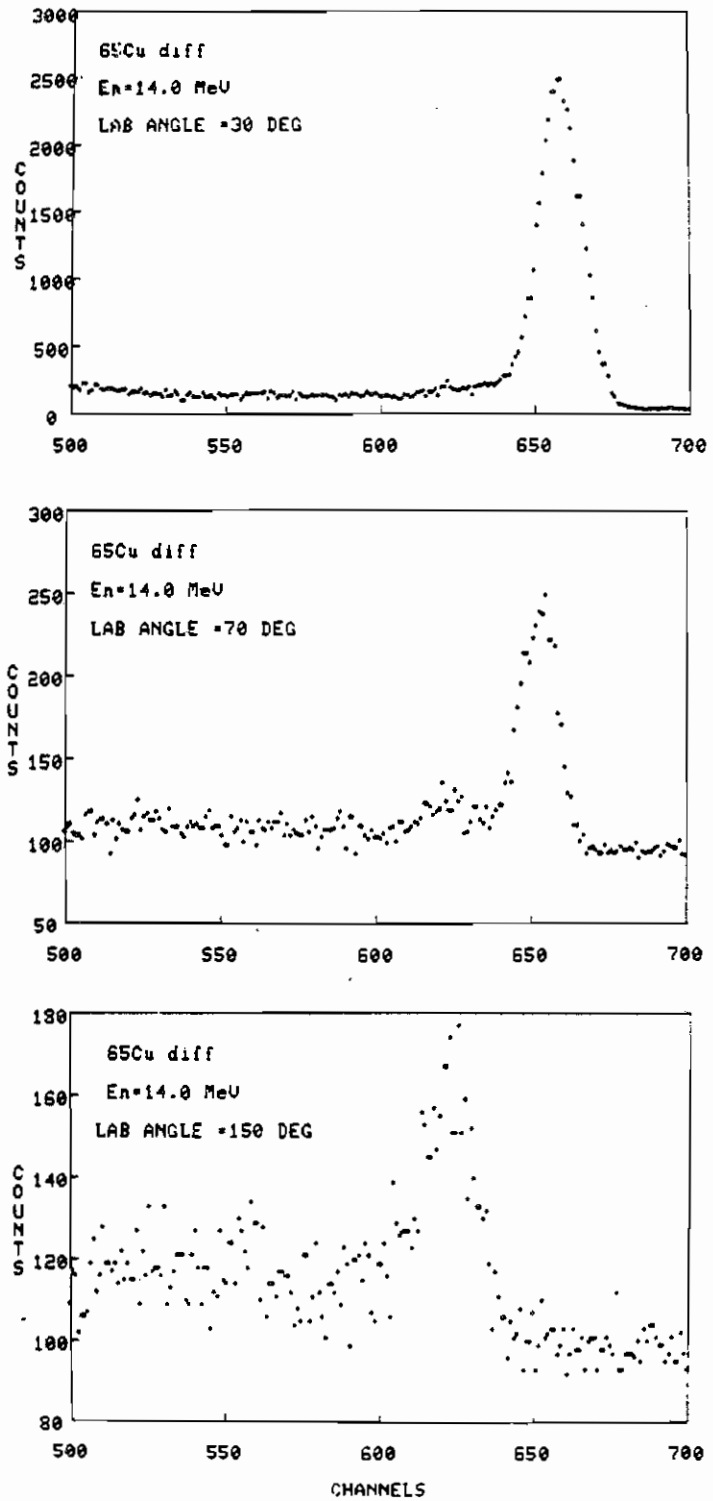

Figure 14 Neutron difference spectra for 14 MeV ^{65}Cu at 30^0, 70^0, and 150^0 (see section 2.5).

beam stop and scattered by sample, runs with an evacuated gas cell would be required. To save run time, the 'gas-out' runs were not taken, and this contribution to the spectrum was approximated by a low order polynomial (Hogue 1977).

In the present work a smooth background around the peak of interest [using a low order polynomial] was determined by setting windows on both sides of the peak, and making a polynomial fit to the counts in those windows. The function extended through the region of interest. A window containing the peak was then set. A window was also set in the ceiling monitor spectrum which was used to measure the yield from the $^{2}H(d,n)^{3}He$ reaction. A polynomial function was used also to describe the background lying under the peak of interest in the $^{2}H(d,n)^{3}He$ spectrum of the ceiling monitor.

The data reduction code NTOFA subtracts the area under the polynomial fit inside the peak window from the sum over the peak, and then generates a monitor normalized, dead time corrected, and background subtracted yield. The error on the extracted yield was determined by adding in quadrature the statistical error in the sample-in run to that in the sample-out background run.

The separation between the time-of-flight elastic peaks and the peaks due to first-excited states in ^{54}Fe and ^{56}Fe and due, to the combined first- and higher-order-excited states in ^{63}Cu and ^{65}Cu is poor at 12 and 14 MeV. At these

energies one window was assigned to the poorly resolved states in each spectra, and the yield extracted from the peaks inside the assigned windows. The double peak fitting code GAUSSN was then used to determine the ratio of the elastic and the inelastic yields. In the determination of the ratio, the separation between the centroids of the two peaks was estimated by plotting centroids vs. angle for each isotope, obtained in an initial pass through the data. Then, for the final GAUSSN fit, the separation was kept constant to within one channel. The fitting was carried out using two peaks of equal width in the case of ^{54}Fe and ^{56}Fe. For ^{63}Cu and ^{65}Cu, the inelastic peak was given a larger width in order to simulate the spectrum produced by the several inelastic groups from low-lying states. (These window choices for Cu isotopes will be discussed again in the section on coupled channels calculations.) The yield from each peak was deduced by using the following:

$$Yi(\theta) = Ygi(\theta) \cdot Ytof(\theta) / Yg(\theta)$$

where

$Yi(\theta)$ = the yield for the peak i

$Ytof(\theta)$ = the yield calculated by NTOFA

$Ygi(\theta)$ = the yield calculated by GAUSSN for peak i

$Y_g(\theta)$ = the sum of the two peaks found by GAUSSN.

3.2 NORMALIZATION

Yields extracted by the methods described above were converted to measured absolute differential cross section using the following expression:

$$\frac{d\sigma(\theta_1,E_i)}{d\Omega} = \frac{Y_S(\theta_1)}{Y_H(\theta_H)} \cdot \frac{1}{A(\theta_H)} \cdot \frac{n_H}{n_S} \cdot \frac{d\sigma(E_i,\theta_H)}{d\Omega}$$

where

$\frac{d\sigma(E_i,\theta_1)}{d\Omega}$ = differential cross section as a function of its energy E_i and angle θ_1.

$Y_S(\theta_1)$ = yield of a scattering sample at lab angle θ_1 of the group of interest in the difference spectrum.

$Y_H(\theta_H)$ = yield for the hydrogen group from polyethylene scatterer at lab angle θ_H

$A(\theta_H)$ = The hydrogen group correction factor obtained from the Monte Carlo computer code EFFIGY . This factor corrects for flux attenuation, multiple scattering, source anisotropy, and finite geometry effect (see section 3.3)

n_H = number of hydrogen nuclei in polyethylene scaterer

n_S = number of nuclei in the scattering sample

$\frac{d\sigma(E_i,\theta_H)}{d\Omega}$ = differential cross section for neutrons scattered at incident energy E_i through lab angle θ_H by hydrogen (Hopkins et al.1971).

The measured cross section normalized this way must be corrected for finite sample effects.

3.3 DATA CORRECTION

In the past cross-section measurements at TUNL (Hogue 1977 and Glendinning 1980) the correction factor to the hydrogen yields was calculated using the disc approximation (Kinney 1970), with the exception that the carbon non-elastic cross-section was used instead of the total cross section to account for first order multiple scattering correction (Hogue 1977).

The flux attenuation calculated by this approximation was compared to the flux attenuation calculated by Monte Carlo (Glendinning 1980), and the agreement was found to be good to at least 2.5%. In addition, using this approximation to correct for hydrogen group requires the fluence correction ratio F_p/F_s to be 1.0. For $^2H(d,n)^3He$ reaction as a neutron source, Velkley shows that $F_p/F_s=1.0\pm0.01$ (Velkely et al. 1975) if the height and diameter of the polyethelyne are chosen according to the folowing criteria:

$H_p^2(H_p^2+D_p^2) = H_s^2(H_s^2+D_s^2)$ where H_p and D_p are the height and diameter of the polyethylene scatterer, and H_s and D_s are corresponding quantities for sample.

For the present measurement we were able to avoid the restrictions of both the Velkley criterion and those required to make the disc approximation valid. A computer code, EFFIGY, developed at TUNL by H. Hogue in the analysis of ^{1}p-shell neutron data was used to directly determine the

correction factor $A(\theta_H)$, which contains the attenuation fluence factor for polyethylene and other factors relating to the geometry of the normalization. The code is capable of handling a multi-element scattering sample such as polyethylene. The calculation was performed as follows:

1. A time-of-flight spectrum of polyethelene was generated by the code using a table of cross sections submitted as a library to the code in the form of total cross-sections and reduced Legendre polynomial coefficients for elastic, and inelastic scattering for both hydrogen and carbon.

2. A 'sample out' time-of-flight spectrum was generated for a carbon scatterer containing the same number of carbon nuclei as the polyethylene scatterer.

3. Difference time-of-flight spectra were generated by subtracting the carbon spectra from that of polyethylene using a computer code SUBSPECT.

4. Time-of-flight windows were set for the generated neutron difference spectra, closely approximating the experimental windows.

5. The code EFFIGY then calculated the group yields for the assigned windows.

6. The ratio of the library cross section to the calculated group yield for a particular angle at a particular energy then gives the correction factor for polyethylene normalization yield at that angle and energy. This correction factor corrects the yield for attenuation, source anisotropy, multiple scattering, and finite geometry effects.

The correction factor calculation for polyethylene was carried out for the energy range between 8 and 14 MeV in 2 MeV steps for the $^{2}H(d,n)^{3}He$ neutron source reaction, and for angles between 30^{0} and 35^{0} in one degree steps. The results of the calculation are given in table 2. The extension of the calculation to cover angles between 25^{0} and 35^{0} for energies between 8 and 20 MeV is now underway at TUNL by Ron Pedroni.

Scattering data for the Cu and Fe samples were also corrected for the effects of attenuation, multiple scattering, detection efficiency, source anisotropy, and finite geometry using the same computer program EFFIGY. This code employs an iterative procedure for calculating correction factors for cross section, which is especially useful tool in the case where there are no well known angular distribution data available to be submitted as library to the code. The library submitted to the code for the calculation of the

TABLE 2

Multiple scattering correction factor $A(\theta_H)$ for the hydrogen yield

energy	8.0 MeV	10.0 MeV	12.0 MeV	14.0 MeV
30^0	1.228	1.219	1.232	1.212
31^0	1.231	1.215	1.233	1.210
32^0	1.235	1.212	1.231	1.209
33^0	1.237	1.210	1.239	1.210
34^0	1.242	1.208	1.238	1.211
35^0	1.247	1.209	1.238	1.212

correction factors for the cross-section data of the present work was formed for each particular sample by taking the observed yield, normalizing them to the hydrogen yields and correcting them approximately for the attenuation. The library is then used to simulate neutron scattering time-of-flight spectra. The user then selects data windows in the same manner that the experimental windows were set. The code then sums the counts between those windows, deduces calculated cross sections and compares them with measured

ones. The code uses these new values to update the library and recalculates in an iterative manner until it reaches agreement between the calculated distribution and the experimental one. Then the code lists the appropriate correction factors. Two to ten iterations were needed to reach suitable conversion in the present work.

The detected multiple scattering events to total scattering events as calculated in EFFIGY can be used to form a ratio vs. scattering angle. The results for ^{54}Fe and ^{65}Cu at 8, 10, 12, and 14 MeV for elastic and inelastic states are shown in figures 15 - 18. It is very clear from the figures that at the first scattering minimum at 8 and 10 MeV a very high percentage of the neutrons detected are from multiple scattering events.

The cross-section data for ^{65}Cu at 10 MeV, corrected for attenuation, source anisotropy multiple scattering, relative efficiencies, and finite geometry effects are compared to the uncorrected data of the same isotope at the same energy in figure 19. As can be seen the corrections are quite large. However, most of the effect is from attenuation in the scattering which is directly related to the total cross section for the sample. This factor is well determined and is nearly independent of the scattering angle.

The contribution of the compound elastic cross section to the elastic scattering cross section data for each isotope has been computed using the computer code OPTICS (Eastgate

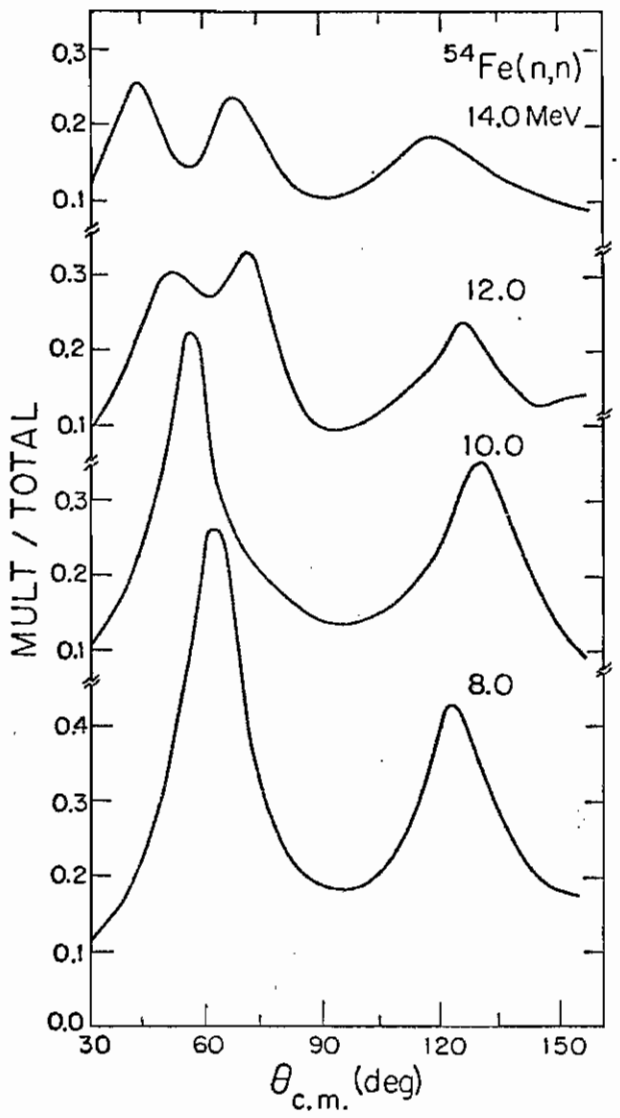

Figure 15 Ratio of multiple scattering to total scattering vs. angle of elastic scattering for ^{54}Fe at 8, 10, 12, 14 MEV.

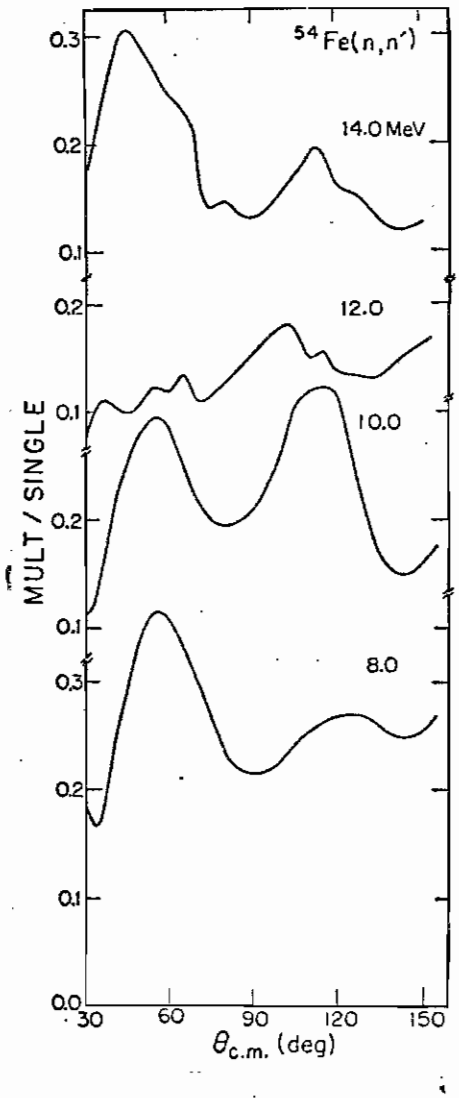

Figure 16 Ratio of multiple scattering to total scattering vs. angle of inelastic scattering for ^{54}Fe at 8, 10, 12, and 14 MeV.

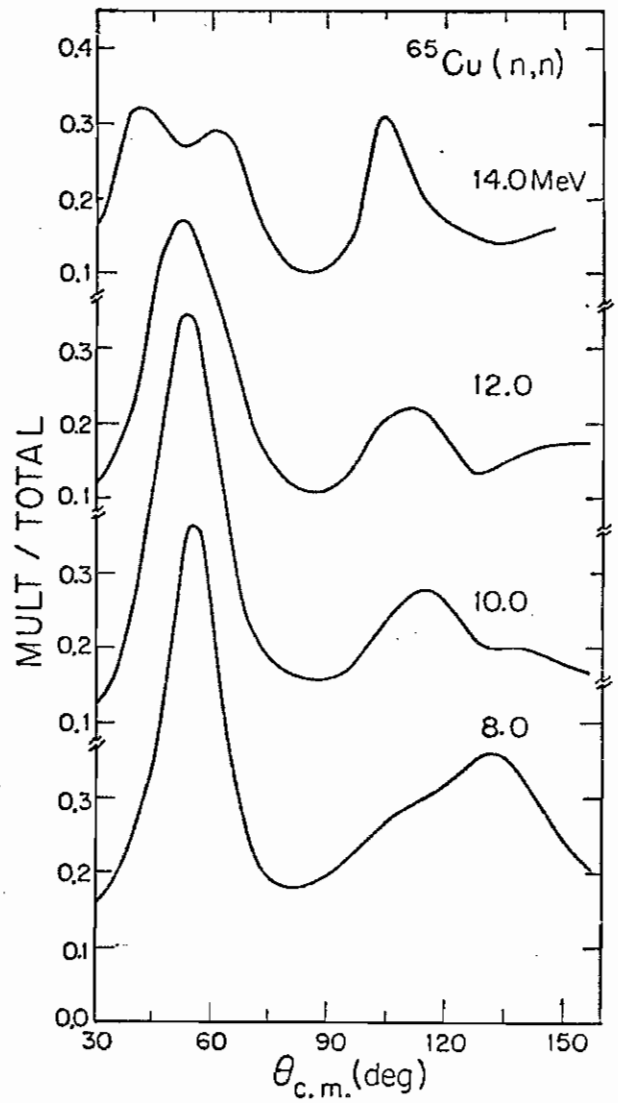

Figure 17 Ratio of multiple scattering to total scattering vs. angle of elastic scattering of ^{65}Cu at 8, 10, 12, and 14 MEV.

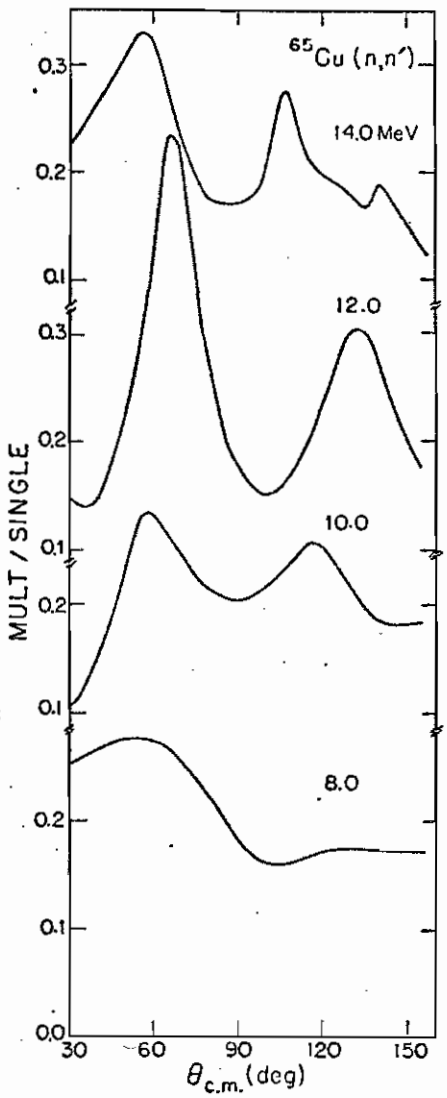

Figure 18 Ratio of multiple scattering to total scattering vs. angle of inelastic scattering of ^{65} CU at 8, 10, 12, and 14 MeV.

et al. 1973) for the energy range of the present work. This contribution was found to be less than 4% and has been neglected.

The uncertanties in the present experimental data are due to the contributions of two types of errors:

1. Relative errors. This type of error can result from the following:

   a) Angle uncertainty, which is the uncertianty due to aligning the scattering sample. It is assumed to be 0.2^0 for all the scattering samples of the present work.

   b) Statistical and background subtraction errors, which range from 1 to 10%.

   c) Monte Carlo correction uncertainties, which are between 1-15%.

   d) In the cases where the elastic and inelastic peaks overlapped, typically at 12 and 14 Mev, the separation of elastic from the inelastic scattering became more difficult and an extra error was assigned because of that.

2. Normalization errors. This type of error scales the angular distributions. It is the result of normalizing the data of the present work to the $^1H(n,n)^1H$ differential cross sections. As the incident energy

increases, the separation of the hydrogen elastic peaks from the elastic and the inelastic due to the first excited state of carbon becomes poorer. This implies an increase in the normalization errors. The uncertainties on the differential cross sections of hydrogen as well as the uncertainties on the correction factor for the hydrogen yields of the polyethylene resulting from Monte Carlo calculations also contribute to the normalization errors.

The results of the relative errors and the normalization errors are then added in quadrature to form the errors assigned to each cross section point in the present work. It is important to mention that some of the elastic scattering cross sections plots in this text have improper error bars attached to the cross section points. The cross section as well as the proper errors are given in Appendix B. In particular, the error bars for ^{65}Cu(n,n) at 10 MeV are shown with error bars about 1 to 3 times smaller than those in appendix A. For expediency and economy, these figures were not remade for the present illustration of the data.

3.4 DATA PRESENTATION

Center-of-mass elastic and inelastic differential cross-section data for ^{54}Fe, ^{56}Fe, ^{63}Cu, and ^{65}Cu at 8 to 14 MeV are presented in figure 20-27. The inelastic angular distributions at 8 and 10 MeV for ^{63}Cu are due to the excited

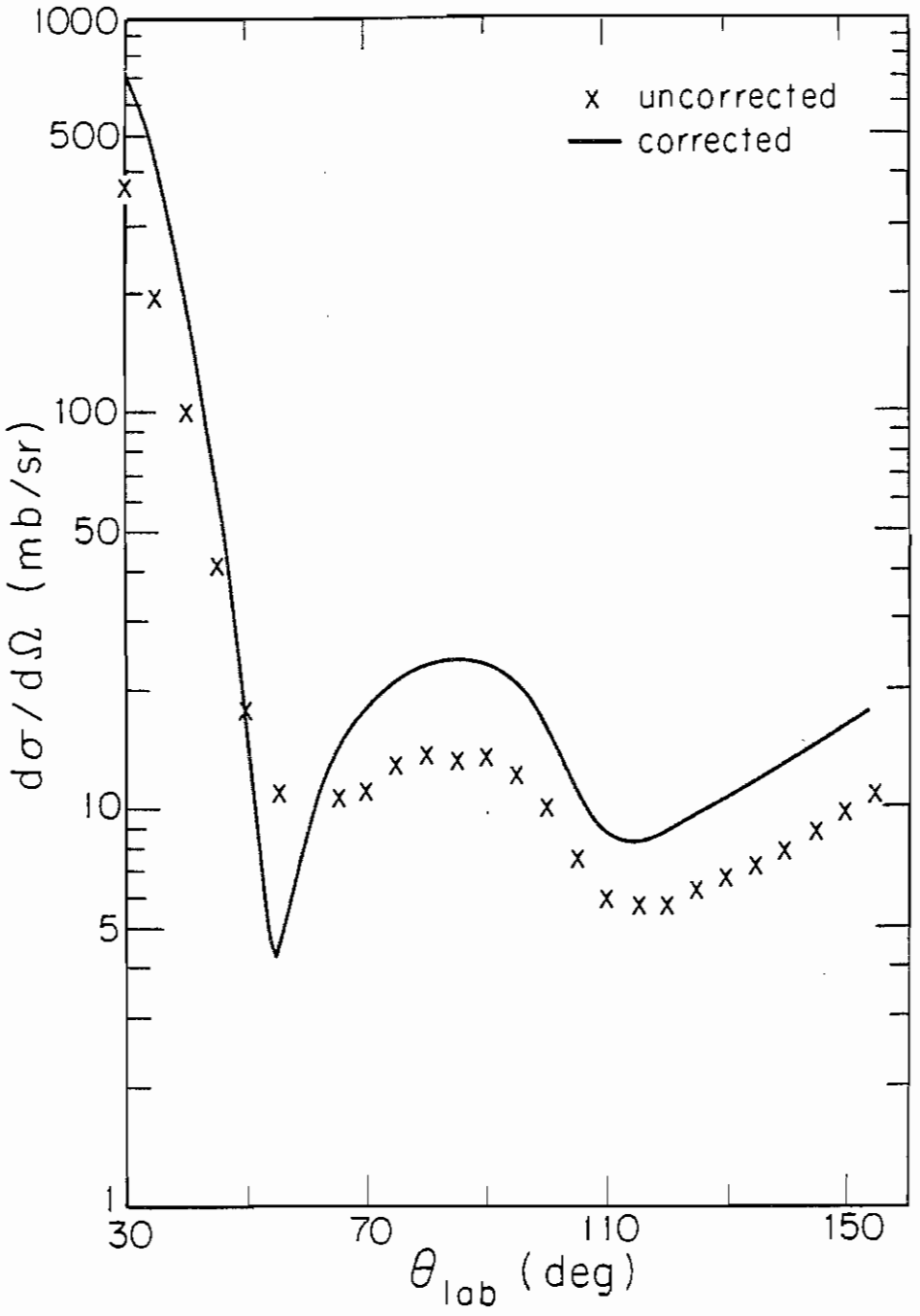

Figure 19 Comparison between 10 MeV ^{65}Cu uncorrected and corrected cross sections (see text).

states at 0.67, 0.962 and 1.327 MeV and for ^{65}Cu are due to the excited states at 0.771, 1.116 and 1.482 MeV. For 12 and 14 MeV the energy resolution gets poorer and the inelastic angular distributions are not only due to those states mentioned above but also due to the excited states at 1.412 and 1.547 MeV for ^{63}Cu and at 1.623 and 1.725 MeV for ^{65}Cu. The inelastic angular distributions resulting from summing these states are converted to the center-of-mass system as if only one inelastic state was present for each of the two copper isotopes with a Q-value between that of the excited states. The solid lines are the results of fitting each of the data sets with a sum of Legendre polynomials according to:

$$\frac{d\sigma(\theta)}{d\Omega} = \sum_{l=0}^{l_{max}} a_l P_l (\cos\theta).$$

The fits were carried out using the code ANPOW obtained from P. Guss at TUNL. The code has the ability to search for the maximium coefficient order, l_{max}, chosen according to the following criteria:

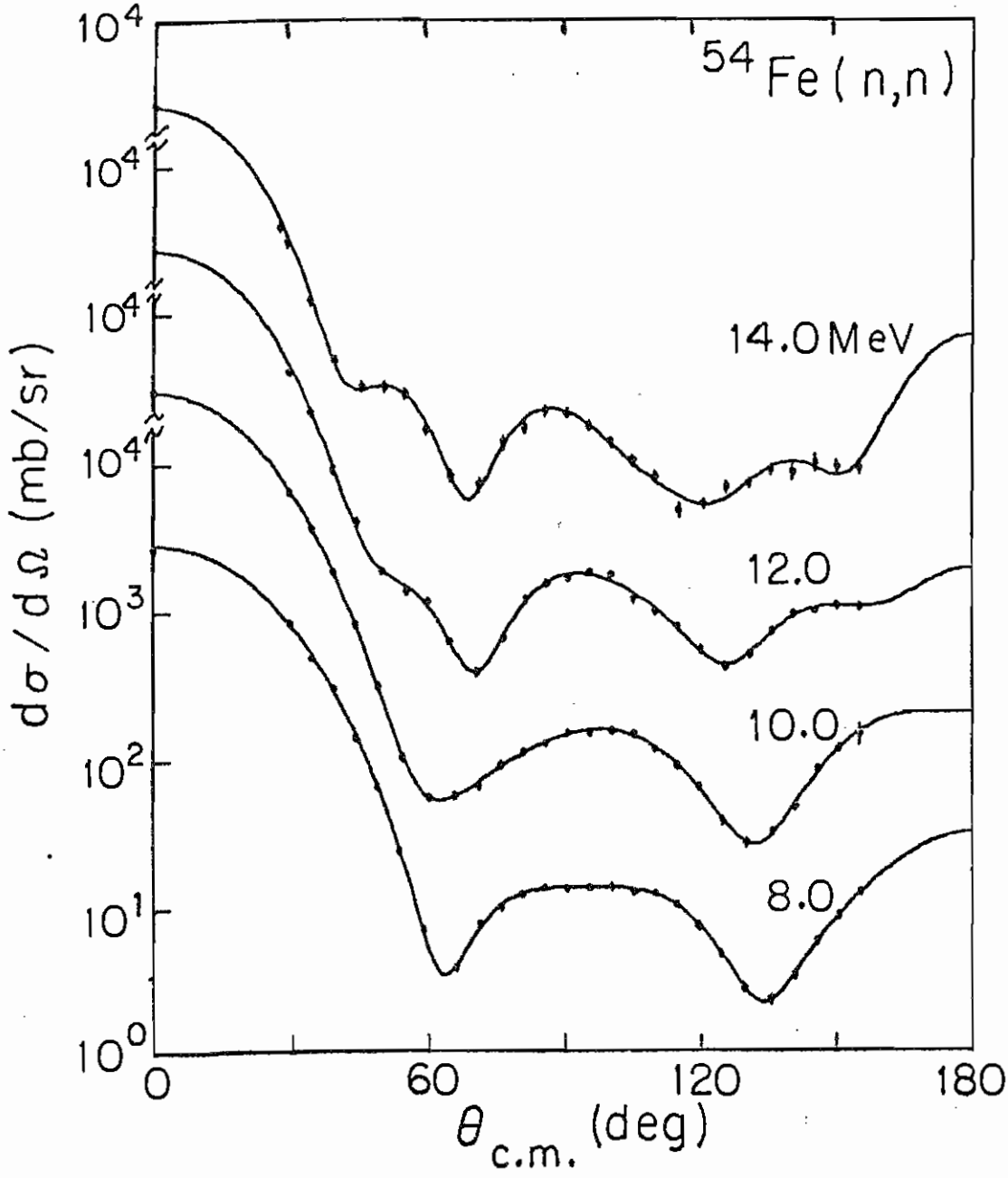

Figure 20 Legendre polynomial fit to the center-of-mass differential elastic scattering cross sections of ^{54}Fe.

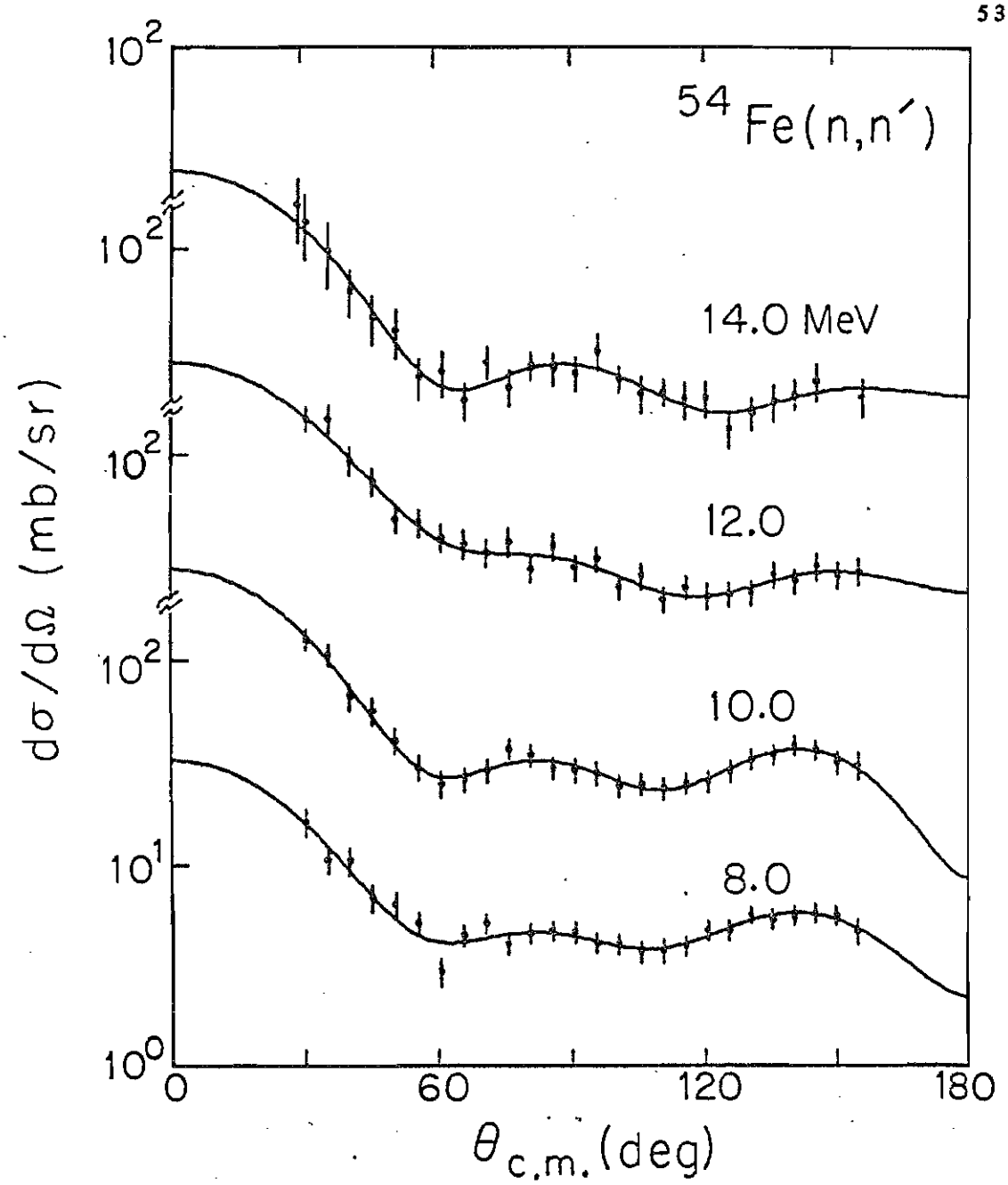

Figure 21 Legendre polynomial fit to the center-of-mass differential inelastic scattering cross sections of ^{54}Fe.

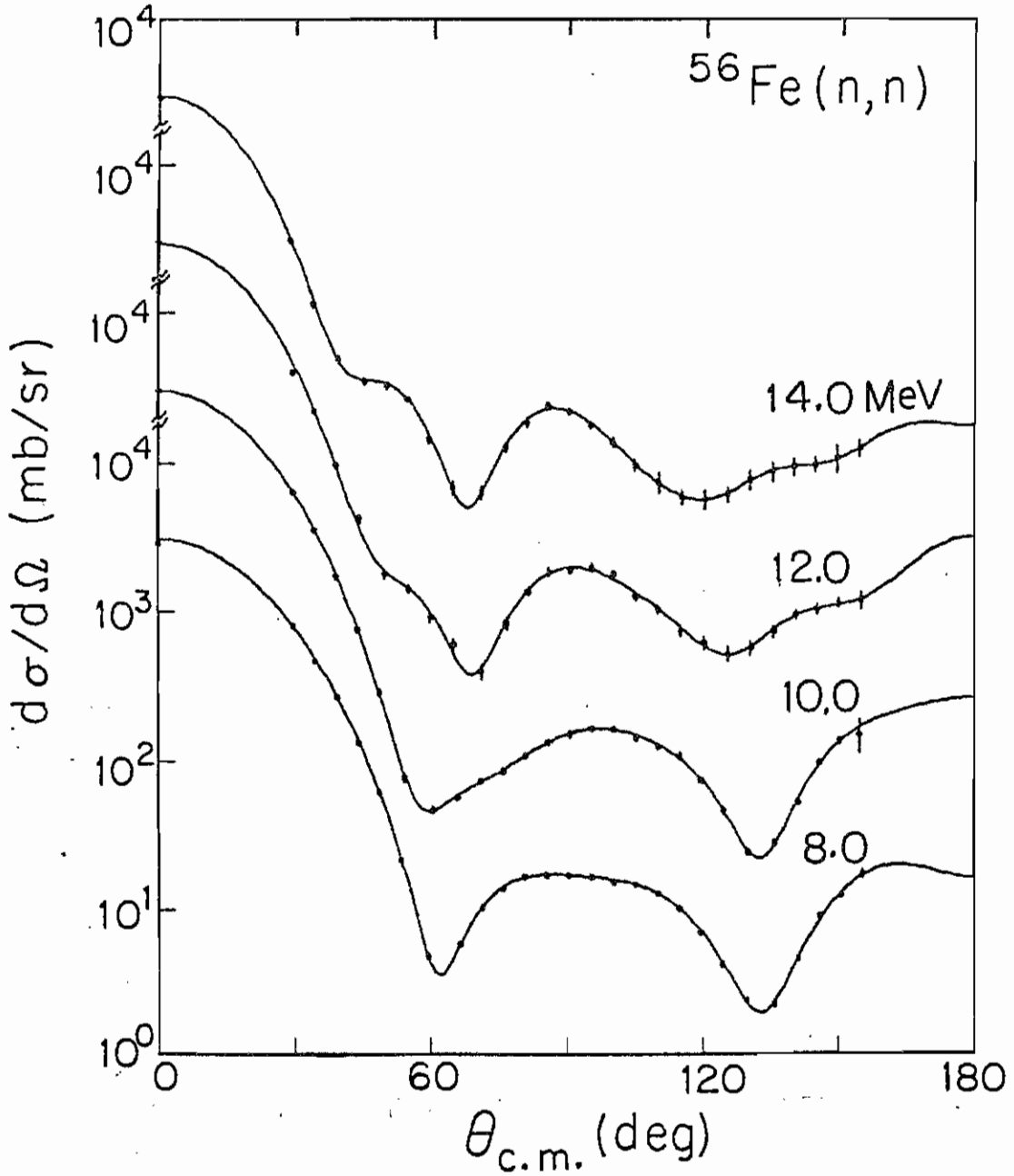

Figure 22 Legendre polynomial fit to the center-of-mass differential elastic scattering cross sections of ^{56}Fe.

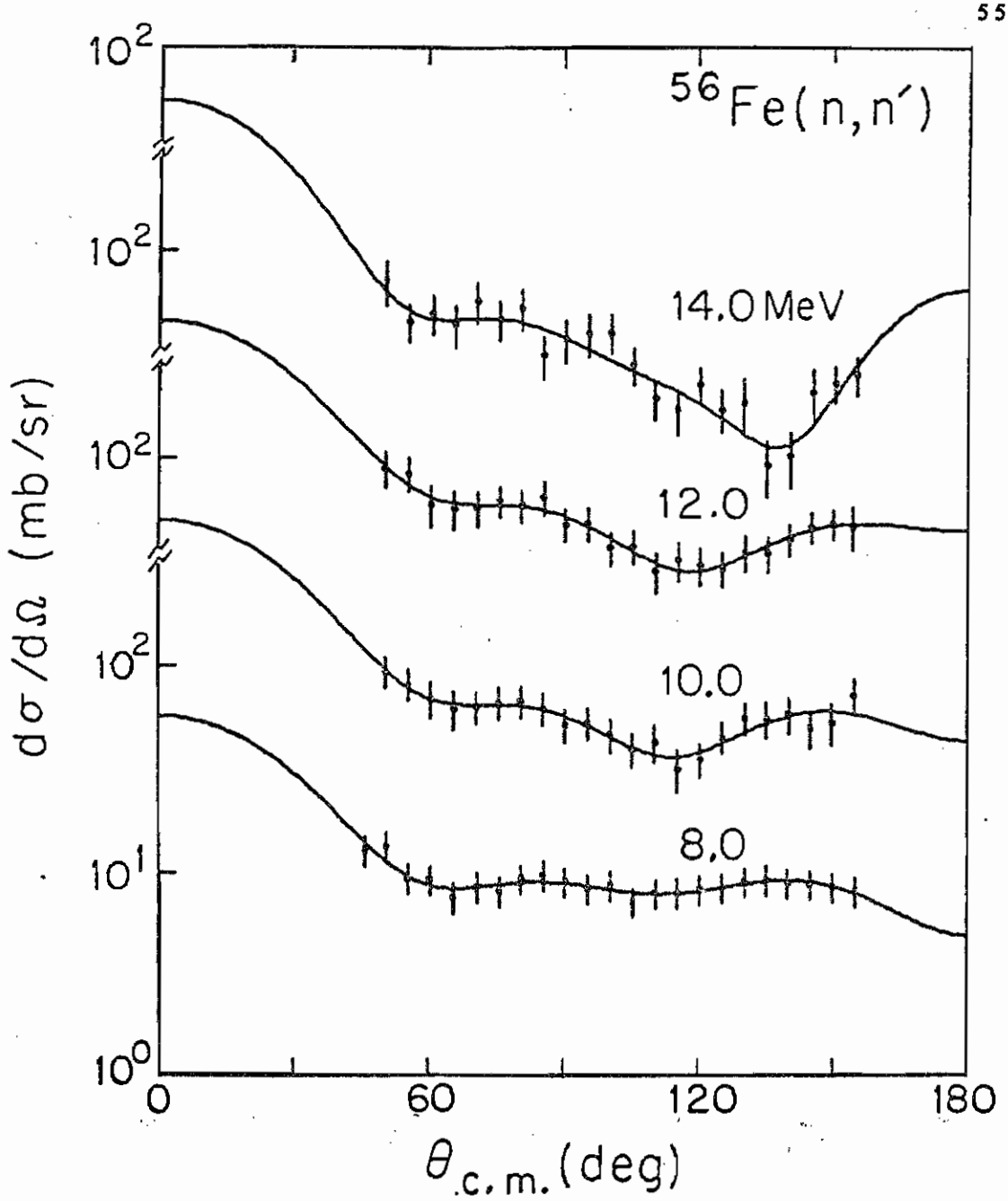

Figure 23 Legendre polynomial fit to the center-of-mass differential inelastic scattering cross sections of ^{56}Fe.

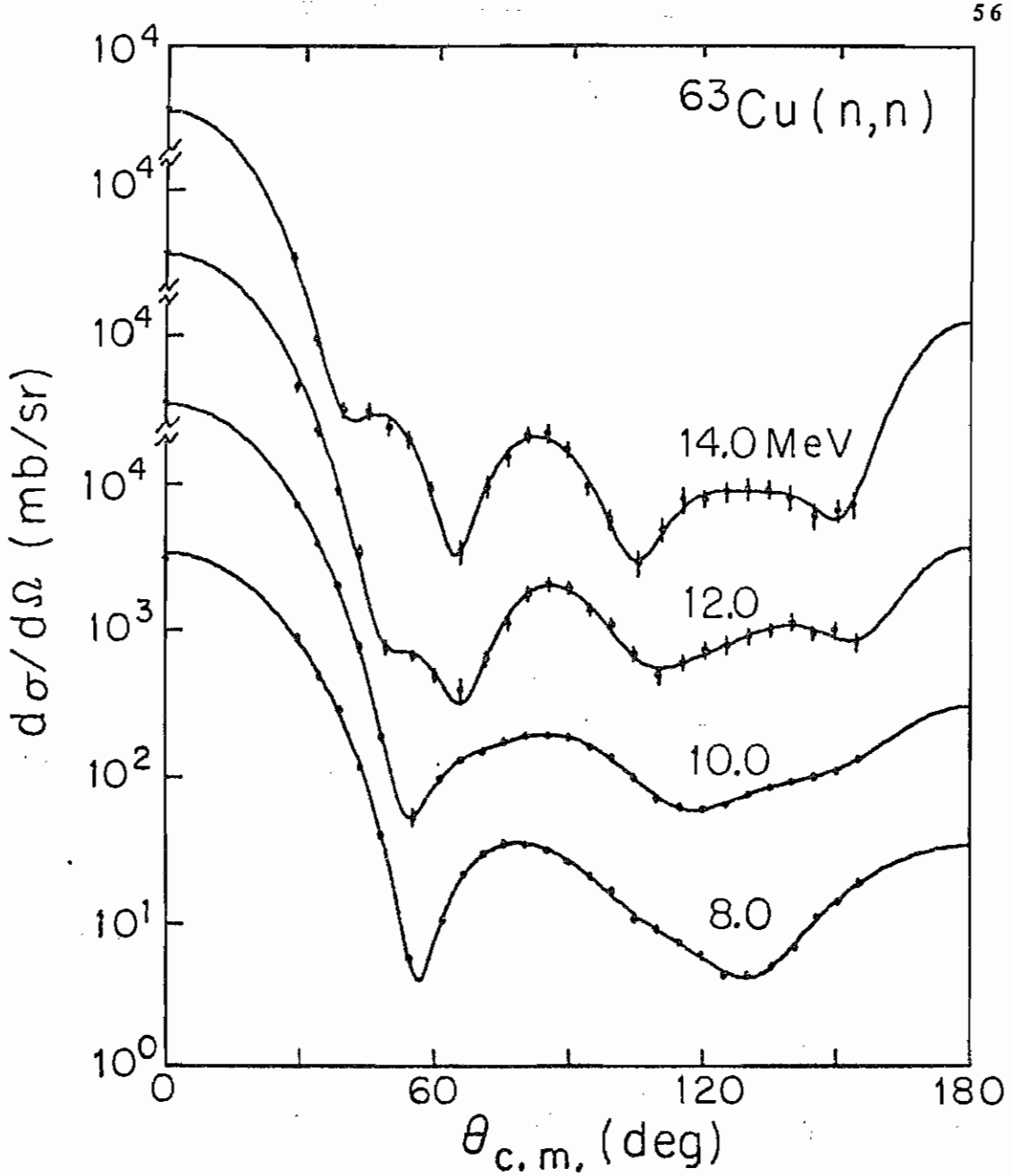

Figure 24 Legendre polynomial fit to the center-of-mass differential elastic scattering cross sections of ^{63}Cu.

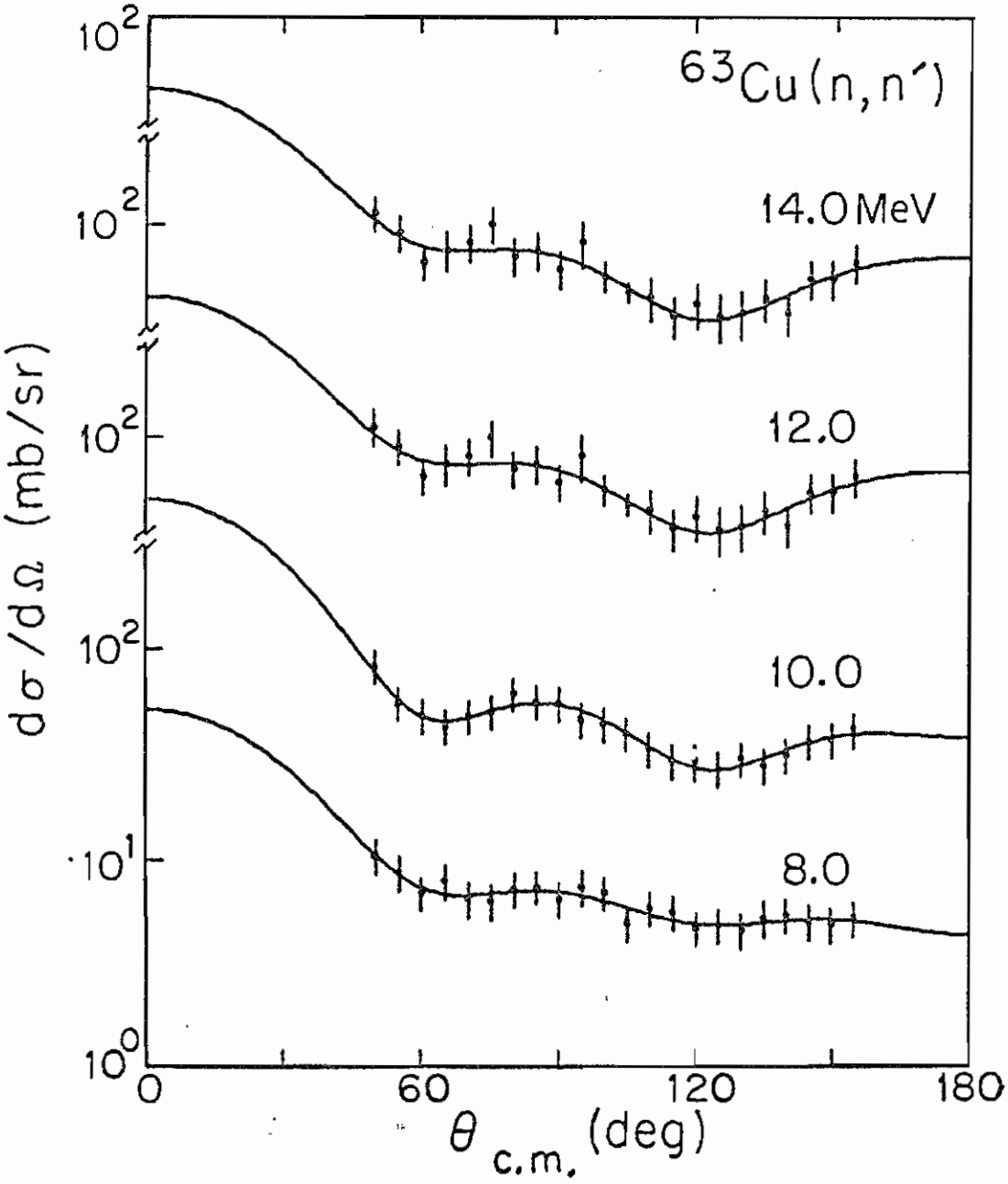

Figure 25 Legendre polynomial fit to the center-of-mass differential inelastic scattering cross sections of ^{63}Cu.

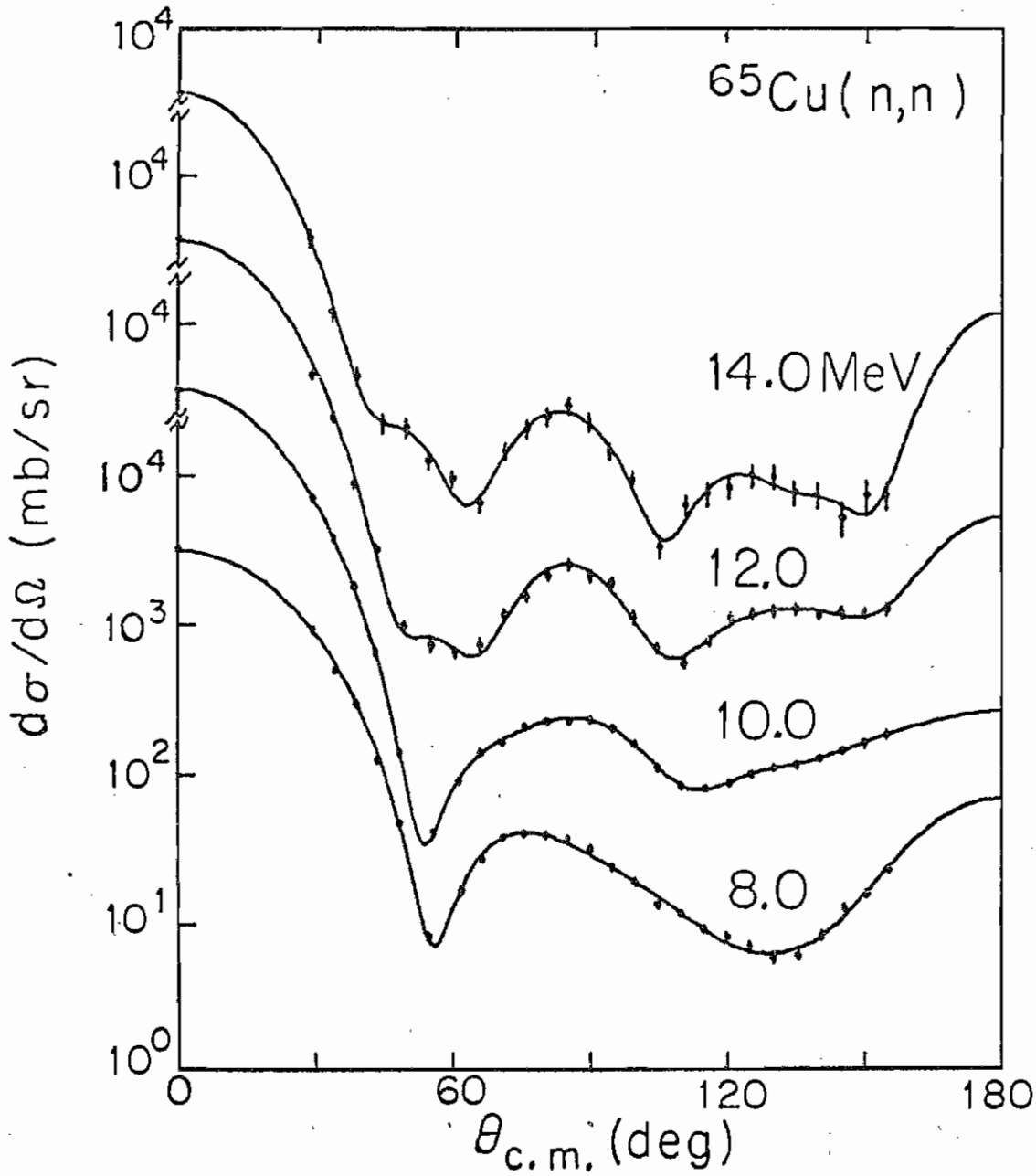

Figure 26 Legendre polynomial fit to the center-of-mass differential elastic scattering cross sections of ^{65}Cu.

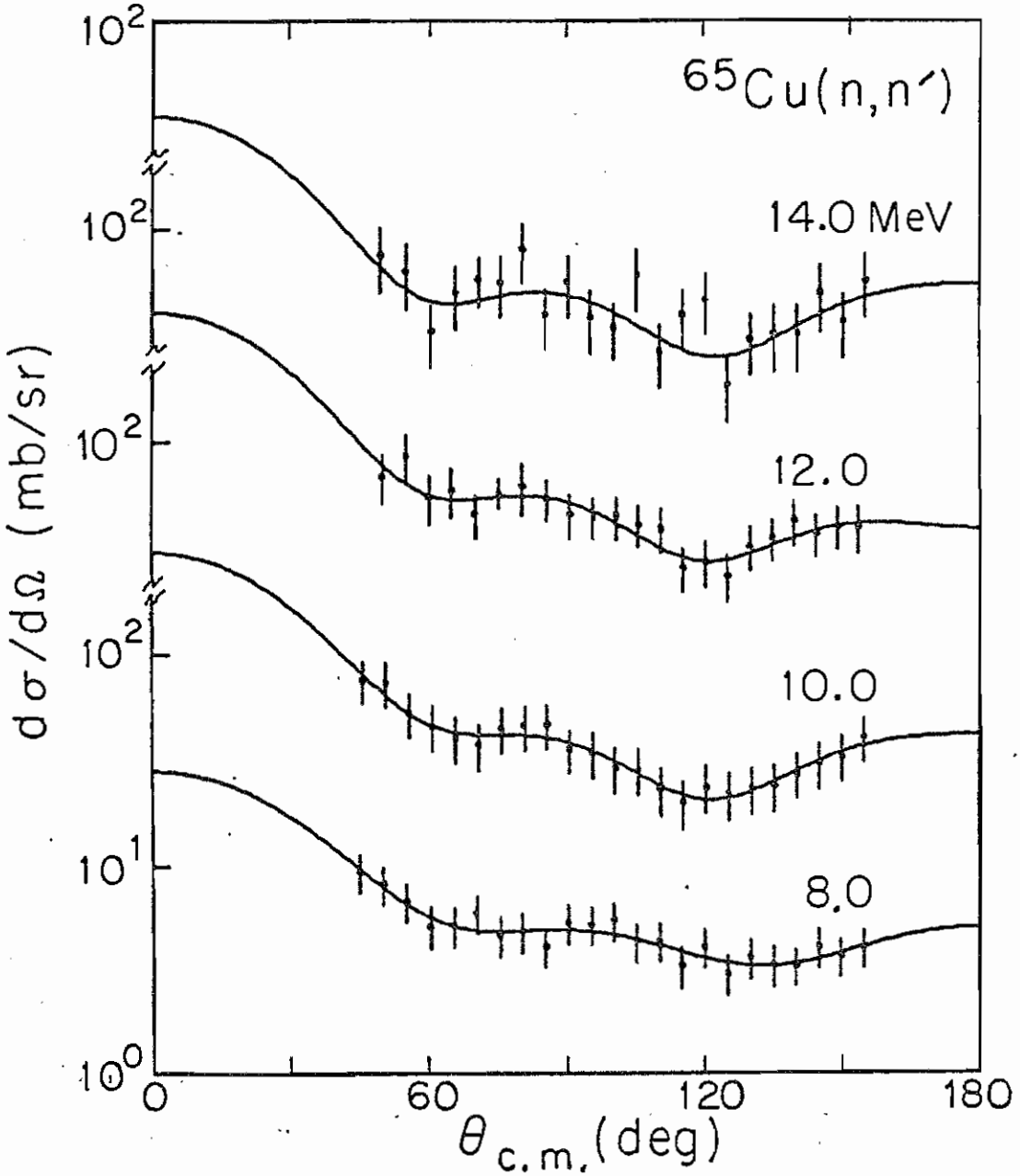

Figure 27 Legendre polynomial fit to the center-of-mass differential inelastic scattering cross sections of ^{65}Cu.

1. Chi-square (X^2) was minimized where

$$X^2 = \sum_{I=1}^{N} (Y_f(\theta_i) - Y_E(\theta_i)/\Delta(\theta_i))^2$$

where N is the number of data points.

Here $Y_E(\theta_i)$, and $\Delta(\theta_i)$ are the experimental cross section and experimental error respectively, and Y_F is the cross section resulting from the fit.

2. Wick's inequality. The lower limit of the elastic scattering cross section at zero degree must be consistent with Wick's inequality, which is a generalization of optical theorem that relates imaginary part of the elastic amplitude to the total cross section σ_T (Wick 1943, Hodgson 1971). This lower limit was obtained from the following ineequality:

$$\frac{dY_F(0)}{d\Omega} \rangle / \sigma_\omega$$

where $\sigma\omega$ is the Wick limit (Wick 1943) and is deter-

mined by

$$\sigma_\omega = (k\sigma_T/4\pi)^2$$

Here k is the centre-of-mass wave number and σ_T is the total cross section. The total cross section σ_T for each isotope at each energy of the present work was extracted from the evaluated total cross-section file ENDFB/V for natural iron and copper by the following process:

$$\sigma_T \propto A^{2/3}$$

$$\frac{\sigma_T(^{65}Cu)}{\sigma_T(^{63}Cu)} = \frac{A^{2/3}(^{65}Cu)}{A^{2/3}(^{63}Cu)} = R(Cu)$$

$$\sigma^T(^{65}Cu) = R(Cu)\ \sigma(^{63}Cu)$$

$$\sigma^T(Nat) = 0.7\sigma_T(^{63}Cu) + 0.3\sigma_T(^{65}Cu)$$

or

$$\sigma_T(^{63}Cu) = \frac{\sigma_T(Nat)}{(0.7 + 0.3\ R(Cu))}$$

In figures 28-31, the integrated elastic cross sections resulting from the best fits are plotted vs. energy together with the corresponding values for natural Fe and Cu obtained from ENDFB/V. As can be seen, the agreement between the

ENDFB/V values and the values obtained in the present work are reasonably good.

For applied purposes, the best description of the cross sections derived in the present work can be obtained from the Legendre polynomial expansion. Therefore, the coefficients are listed in appendix B. To the extent that Wick's limit is valid for these nuclei, the expansions can be trusted for angles down to 0^0. However, because there are no such anchor points near 180^0, the polynomial expansions can be in serious error in the angular region beyond our data at 155^0. Care should be exercised here. Probably the model calculations below are more trustworthy for angles around 170^0-180^0.

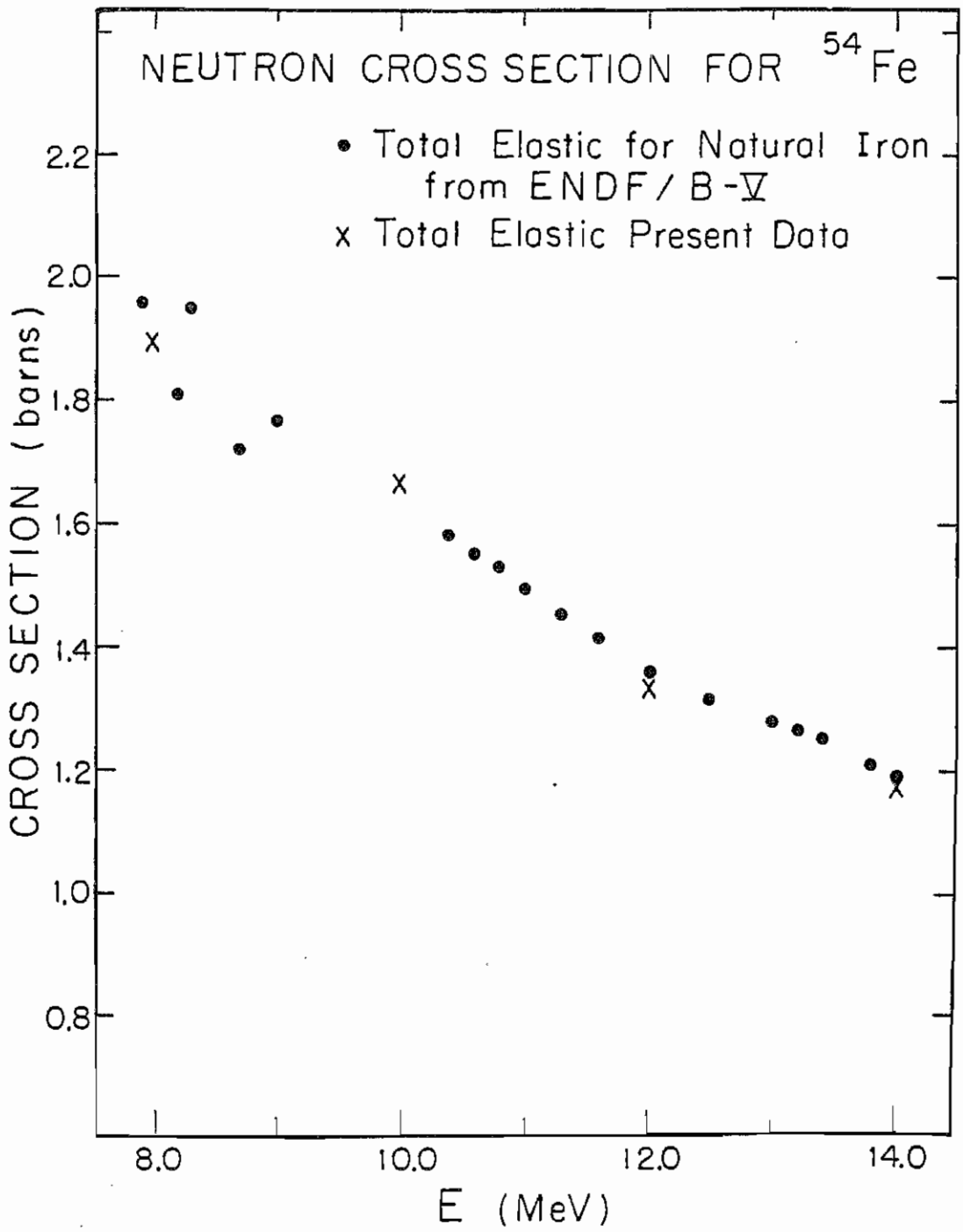

Figure 28 Comparison of the total elastic cross section for ^{54}Fe and the corresponding values of natural iron from ENDFB/V.

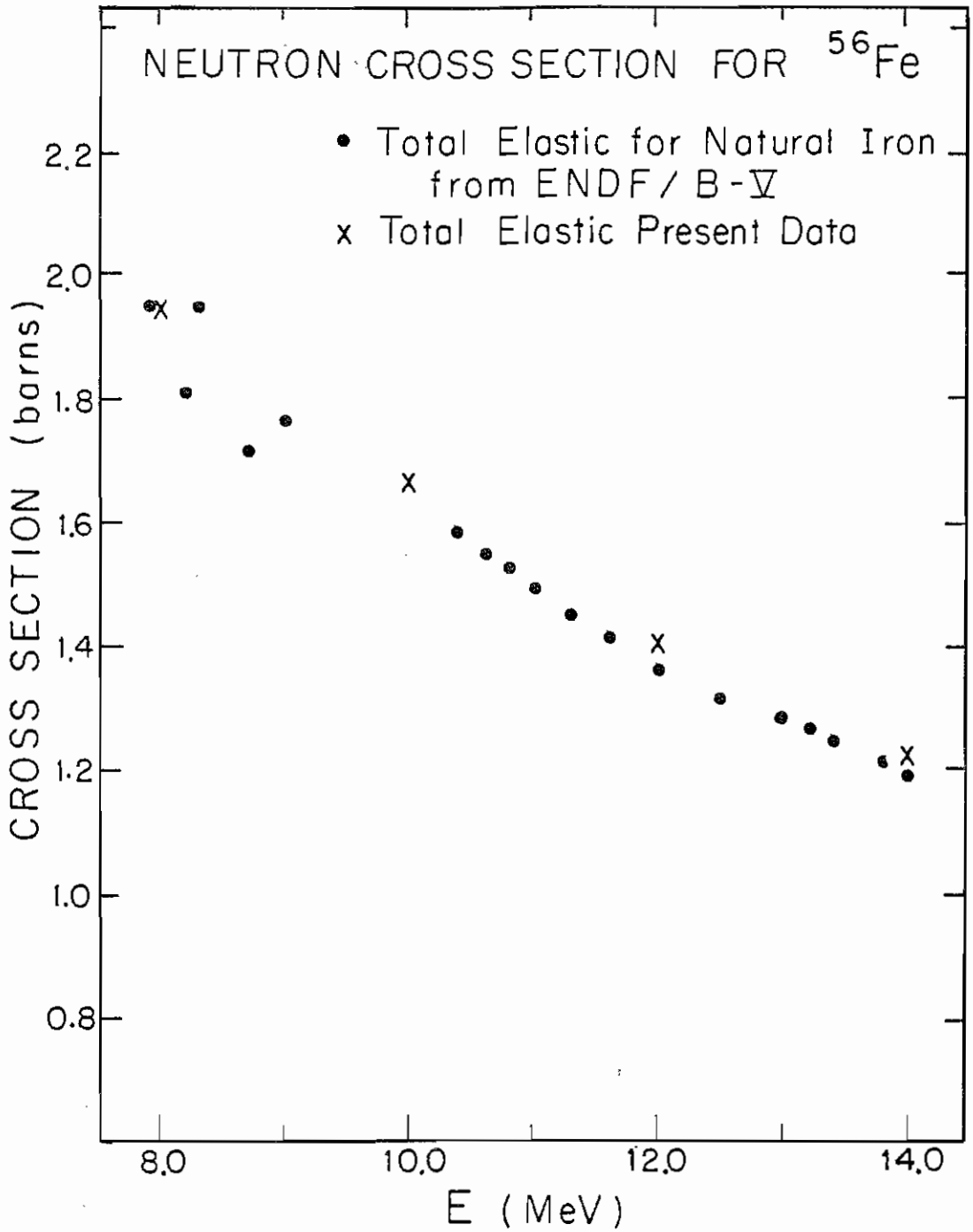

Figure 29 Comparison of the total elastic cross section for ^{56}Fe and the corresponding values of natural iron from ENDFB/V.

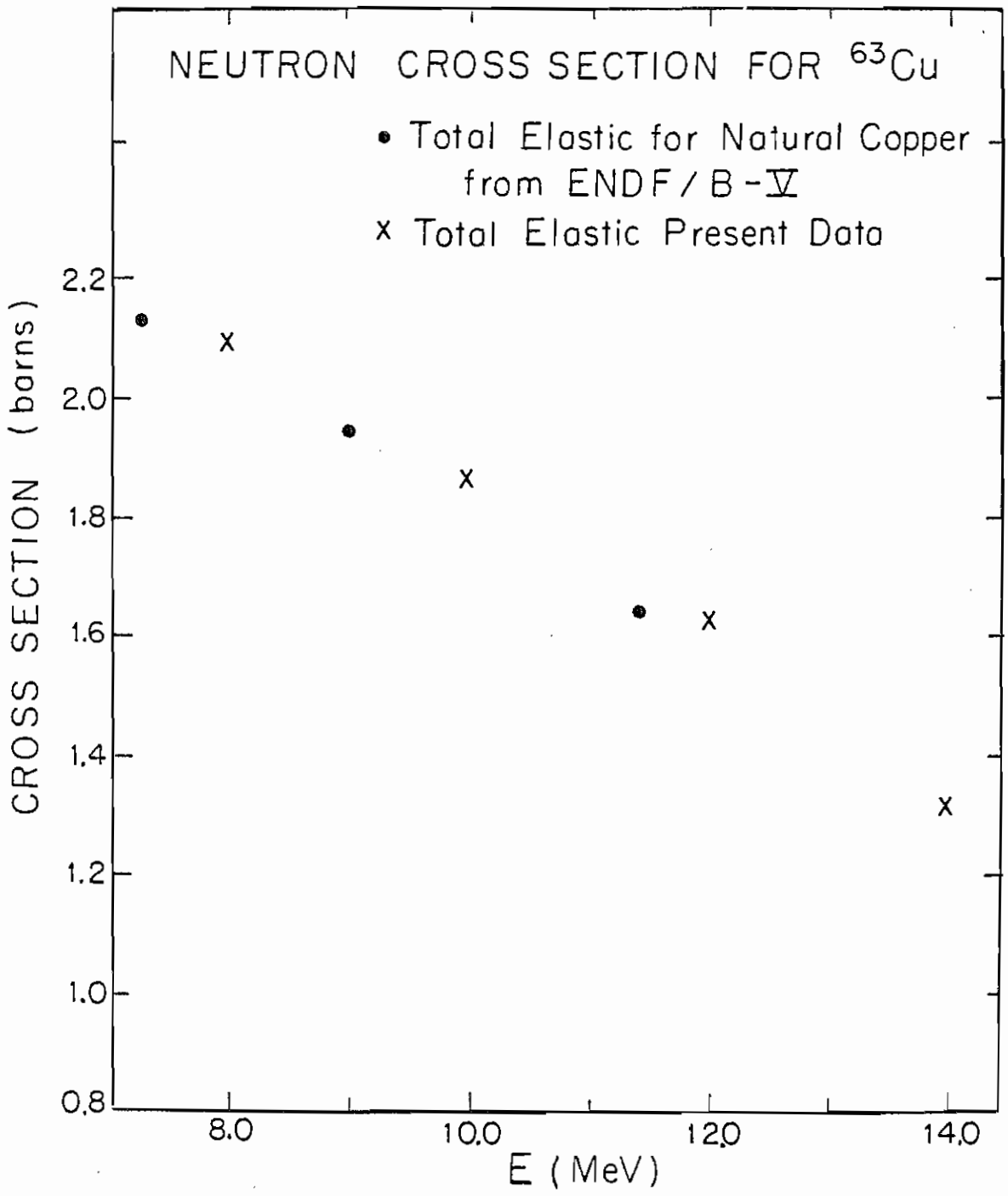

Figure 30 Comparison of the total elastic cross section for ^{63}Cu and the corresponding values of natural copper from ENDFB/V.

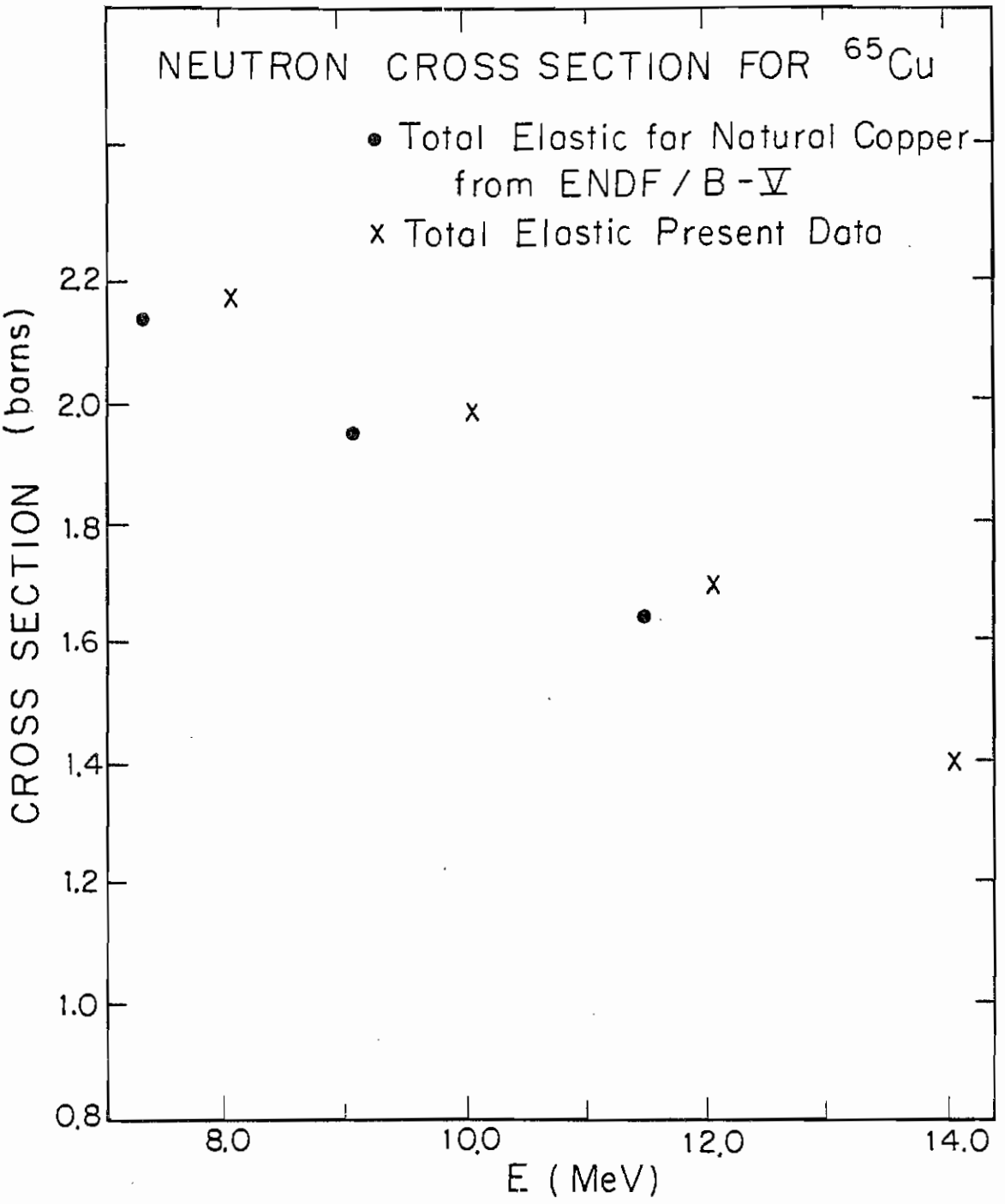

Figure 31 Comparison of the total elastic cross section for ^{65}Cu and the corresponding values of natural copper from ENDFB/V.

Chapter IV

OPTICAL MODEL

Since the proposal of the physical optical model more than twenty years ago, much work has been done dealing with the empirical determination of the appropriate optical model potential (OMP) from fitting experimental data for elastic scattering of nucleons from nuclei. For nearly two decades the spherical optical model has been used to represent elastic scattering from medium and heavy mass nuclei. Use of the spherical optical model for nucleon-nucleus scattering was extended to light nuclei by Watson et al. in 1969 and recently at TUNL (Watson 1969, Hogue 1977 and Glendinning 1980).

Several global parameter sets resulting from fitting data over a wide range in energy and mass number have been published. The most common parameter sets are listed in the compilation by Perey and Perey(Perey 1974). Recently, another global parameter set for neutron elastic scattering has been described (Rapaport et al. 1979). Later in this chapter some of these global parameter sets will be tested against the data of the present experiment.

In the present analysis, the spherical optical model was used to obtain fits to neutron elastic scattering cross sections for separated isotopes of iron and copper. The analysis was done in the following sequence:

1. Individual searches for each target nucleus at each energy that measurements were made, i.e. 8, 10, 12 and 14 MeV.

2. An average for each geometry parameter was calculated for each nucleus. The data were searched again keeping the geometry fixed at these values.

3. For each nucleus the well depths were constrained to have a linear energy dependence, and the data were searched again, this time with the average geometry parameters also.

4. The geometry parameters and energy dependences for all four nuclei were averaged and kept fixed. The data for each nucleus was searched to obtain optimum well depths from which then a magnitude for the symmetry terms (N-Z)/A were obtained.

5. A symmetry term (N-Z)/A was inserted in the OMP and a global search was carried out, allowing the coefficient in both the symmetry terms and the energy dependence to vary. This simultaneous search was concentrated on the iron and copper data although

data for other nuclei were eventually included to apply some loose constraints on the global behavior of the parameters.

4.1 SPHERICAL OPTICAL MODEL POTENTIALS

For our purposes here, the optical model potential (OMP) for neutron scattering is defined as follows:

$$U(r) = -Vf(x) + (h^2/(m_\pi.c))^2 V_{so}(\sigma.l)\ 1/r\ df(x_{so})/dr$$

$$-i[W_v\ f(x_v) - 4W_D\ df(x_D)/dx_D)]$$

where $f(x)$, $f(x_v)$, $f(x_D)$ and $f(x_{so})$ are Woods-Saxon form factors defined as follows:

$$f(x_i) = 1/(1 + e^{x_i})$$

$$x_i = (r - r_i A^{1/3})/a_i.$$

Here r_i and a_i are the appropriate radius and diffuseness parameters.

4.2 OPTICAL MODEL ANALYSES

The data were fitted using an optical potential search code GENOA obtained from F. Perey. The global feature of the code allows fitting of individual as well as several data sets with or without constraints on the parameters. These data sets may vary over energy and target mass. The goodness of the fit is provided by X^2 defined as:

$$X^2 = (1/N) \sum_{i=1}^{N} [(\sigma_{th}(\theta_i) - \sigma_{exp}(\theta_i))/\Delta\sigma_{exp}(\theta_i)]^2$$

Here N is the number of data points in the distribution being fitted, $\sigma_{th}(\theta_i)$ is the theoretical differential elastic cross section, $\sigma_{exp}(\theta_i)$ and $\Delta\sigma_{exp}(\theta_i)$ are the experimental differential elastic scattering cross section and the corresponding experimental uncertainties.

As mentioned above, several sets of global OMP parameters are available. In this section, the data of the present work are used to test the predictions of some of the widely used parameter sets. A wide range of neutron differential elastic scattering cross-section data for nuclei with A $>$ 40 and for energies less than 50 MeV has been analyzed by (Bechetti and Greenlees 1969). One should note here that most of their data was proton data and most of their neutron data was low energy or concentrated at 14 MeV. The optimum neutron parameters obtained from their analysis are:

$V = 56.3 - 0.32E - 24(N-Z)/A$

$W_D = 13 - 0.25E - 12(N-Z)/A$, or Zero whichever is greater

$W_v = 0.22E - 1.56$, or Zero, whichever is greater

$r = 1.17$, $a = 0.75$

$r_D = r_v = 1.26$, $a_D = a_v = 0.58$

$V_{so} = 6.2$, $r_{so} = 1.01$, $a_{so} = 0.75$

One should note also that here and in the following parameter sets, all well depth are in MeV and all the lengths are in fm. Also, the energy E is the laboratory energy of the incident nucleon. It is assumed also that the volume imaginary potential has the same geometry as the surface imaginary one.

The data in the present work for ^{54}Fe and ^{65}Cu are compared with the predicted angular distributions resulting from these parameters in figures 32-33. The discrepancies for ^{56}Fe and ^{65}Cu are nearly the same as those shown in these figures. As can be seen from the figures these parameters fail to predict our data, especially at the lower energies.

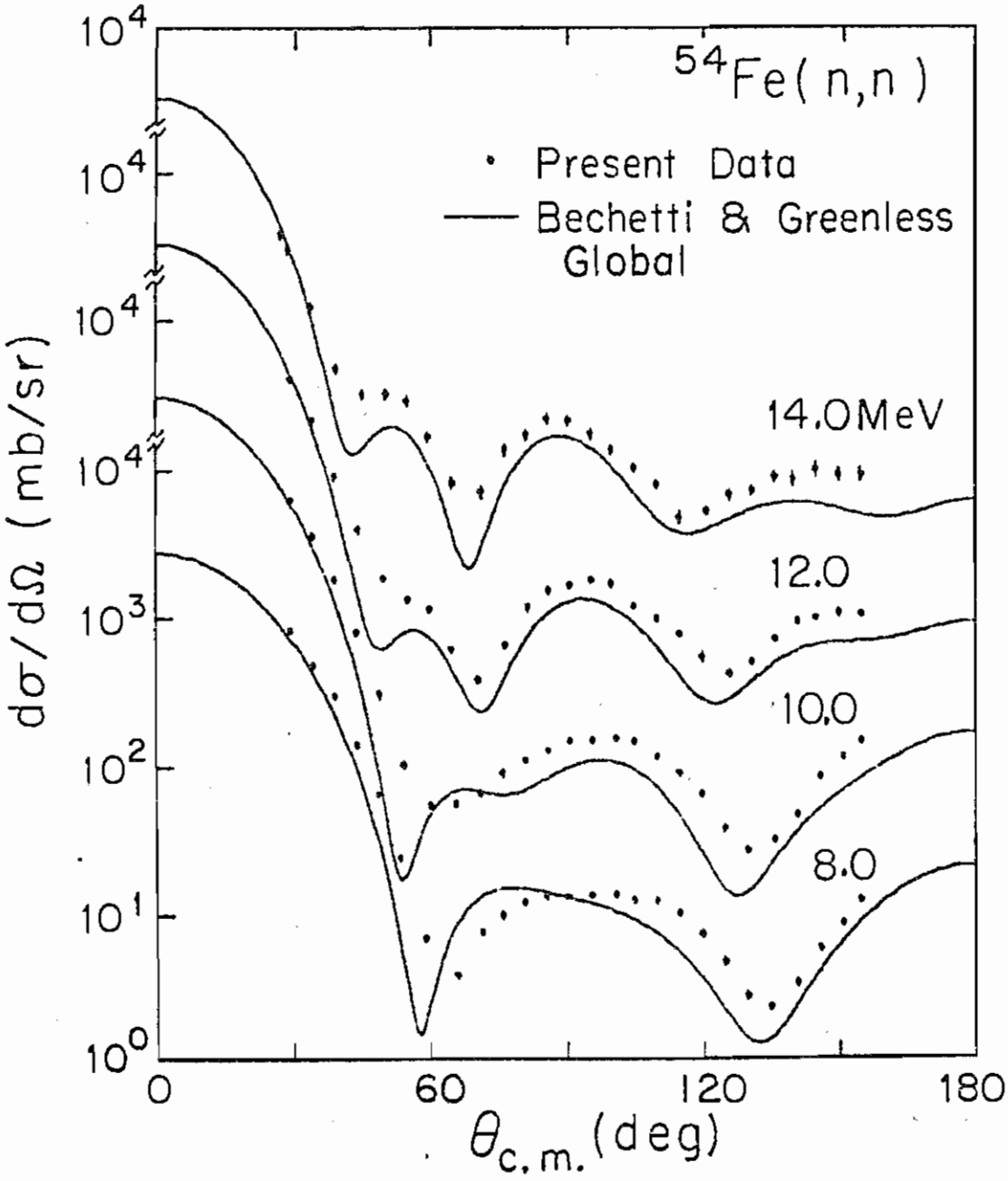

Figure 32 Comparison between the data of the present work for ^{54}Fe and the prediction of Bechetti and Greenlees global parameters.

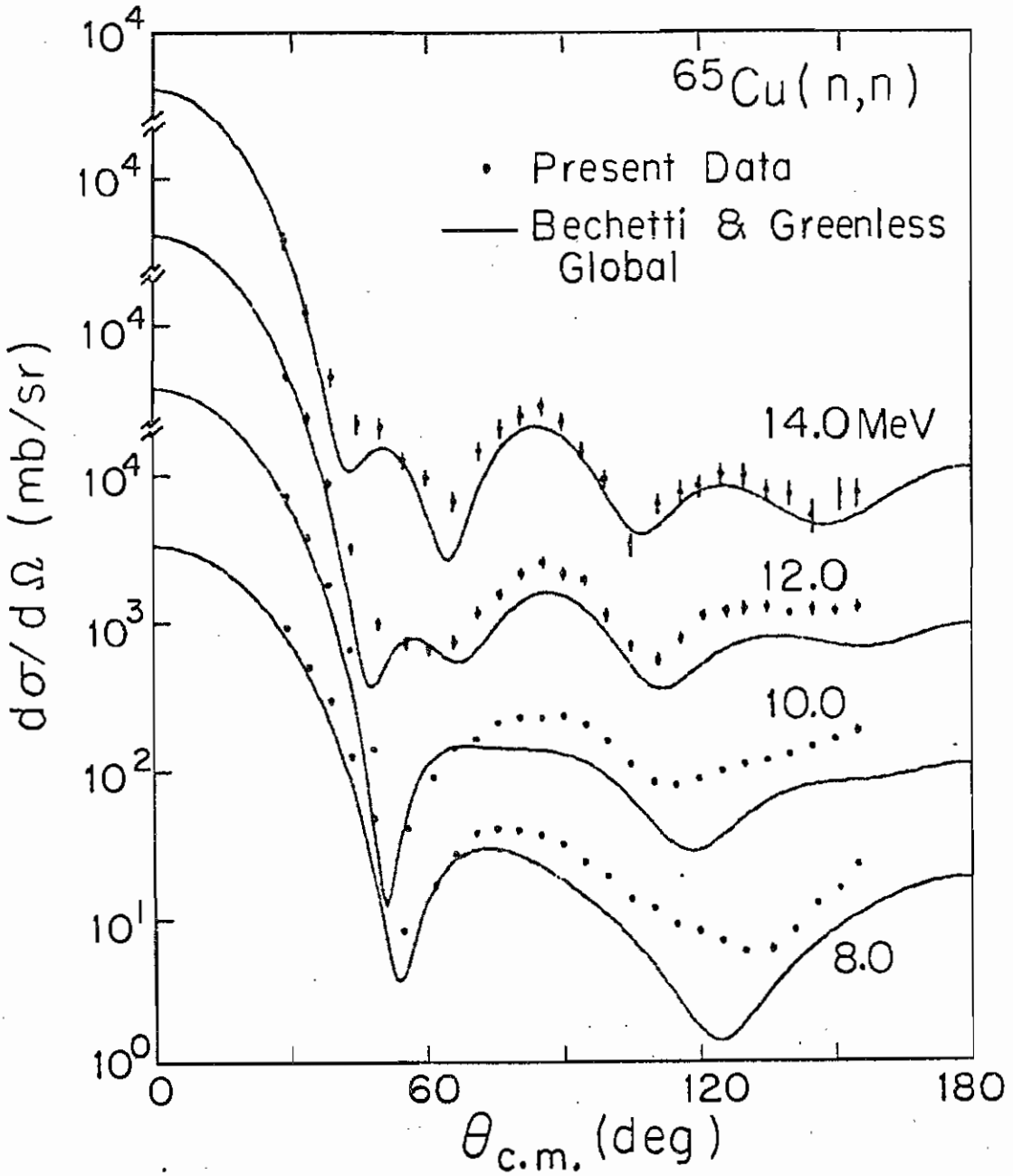

Figure 33 Comparison between the data of the present work for ^{65}Cu and the prediction of Bechetti and Greenlees global parameters.

An overall local potential which is equivalent to the non-local potential of Perey and Buck (Perey and Buck 1962) has been obtained by Wilmore and Hodgson (Wilmore and Hodgson 1964) and results in the following parameters:

$$V = 47.01 - 0.267E - 0.0018E^2$$

$$r = 1.322 - 7.6Ax10^{-4} + 4A^2x10^{-6} - 8A^3x10^{-9}$$

$$a = 0.66$$

$$W_D = 9.52 - 0.053E$$

$$r_D = 1.266 - 3.7Ax10^{-4} + 2A^2x10^{-6} - 4A^3x10^{-9}$$

$$a_D = 0.48$$

In order to compare the present data with this parameter set, addition of a spin-orbit term is required, since the data of the present work was found to be sensitive to this term. Thus, a standard spin-orbit term determined by Bechetti and Greenlees to be V_{so} =6.2, r_{so} =1.01 and a_{so} = 0.75 has been added. The prediction of this modified global set as well as the experimental data in the present work are shown in figures 34 - 35. Here the agreement between the

data and the calculation is seen to be better than for the predictions with the Bechetti-Greenlees set.

In 1979 Rapaport et al. reported three sets of neutron global optical model parameters (Rapaport 1979). These sets were derived from fitting a range of spherical nuclei, ^{40}Ca, ^{90}Zr, ^{92}Mo, $^{116,124}Sn$ and ^{208}Pb. The following parameters are Rapaport's set B:

$$V = 54.62 - 0.30E - [(N-Z)/A]\ (25.3 - 0.02E)$$

$$r = 1.225 - 2.985/A \quad , \quad a = 0.668$$

$$W_D = 4.27 + 0.4E - 12.7\ (N-Z)/A$$

$$r_D = 1.297 \quad , \quad a_D = 0.59$$

$$W_v = 0.0 \quad \text{for } E < 15 \text{ MeV}$$

$$V_{so} = 6.2 \quad , \ r_{so} = 1.01 \quad , \ a_{so} = 0.75$$

The data as well as the fits resulting from this set are given in figures 36-37. The predictions of this global set are in better agreement with our data than the predictions of the two older global sets mentioned above.

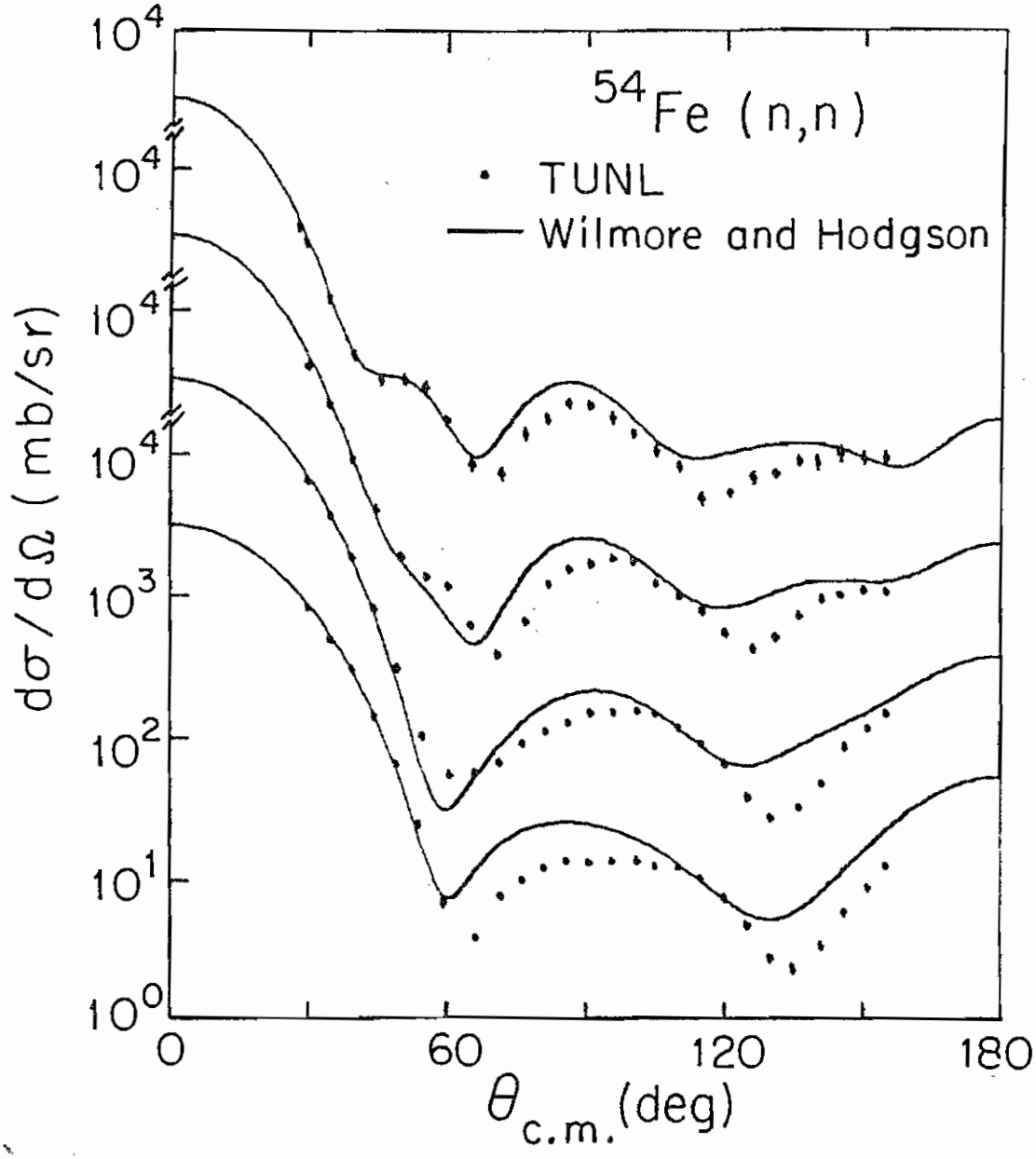

re 34 Comparison between the data of the present work for ^{54}Fe and the prediction of Wilmore and Hodgson global parameters.

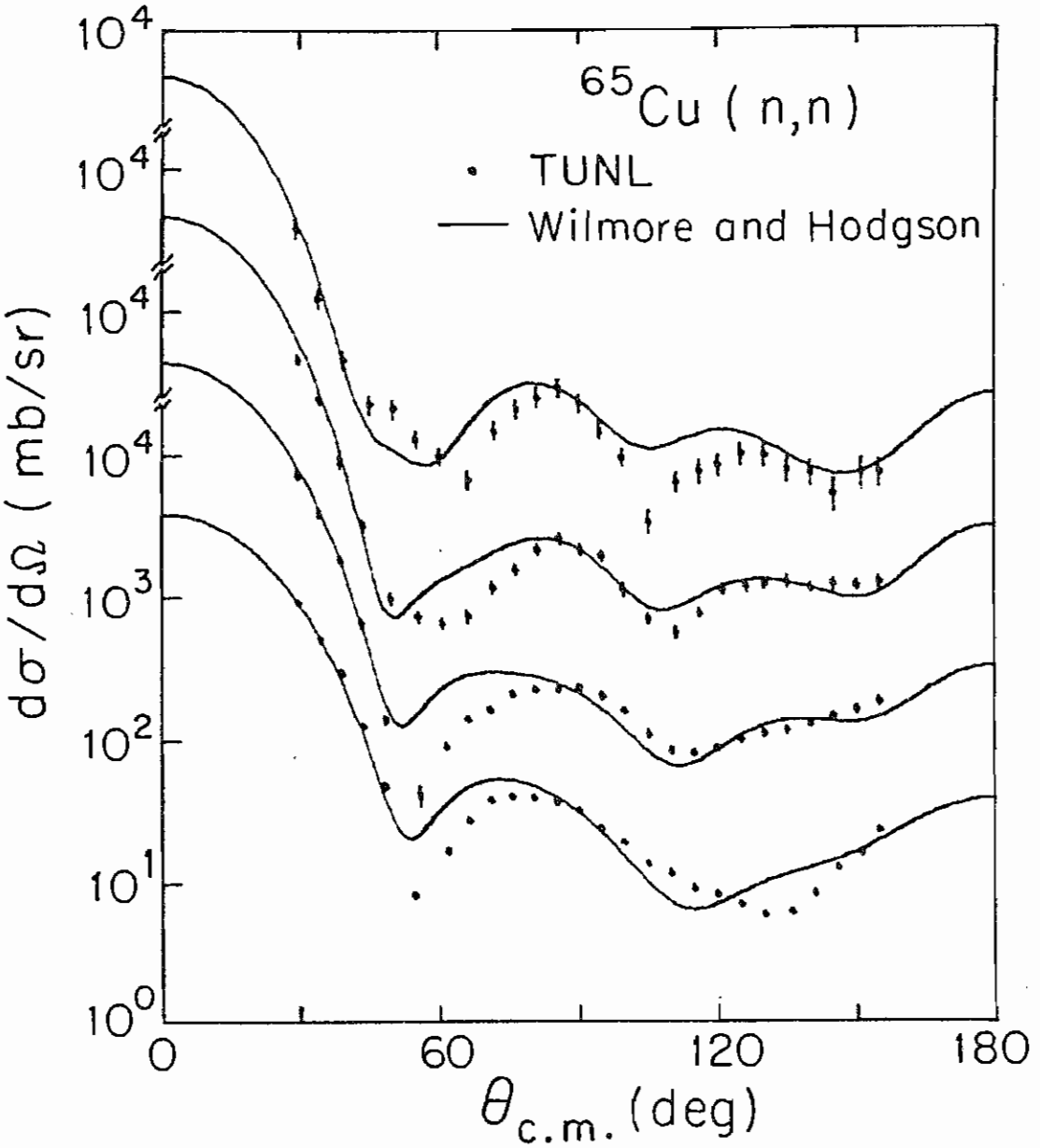

Figure 35 Comparison between the data of the present work for ^{65}Cu and the prediction of Wilmore and Hodgson global parameters.

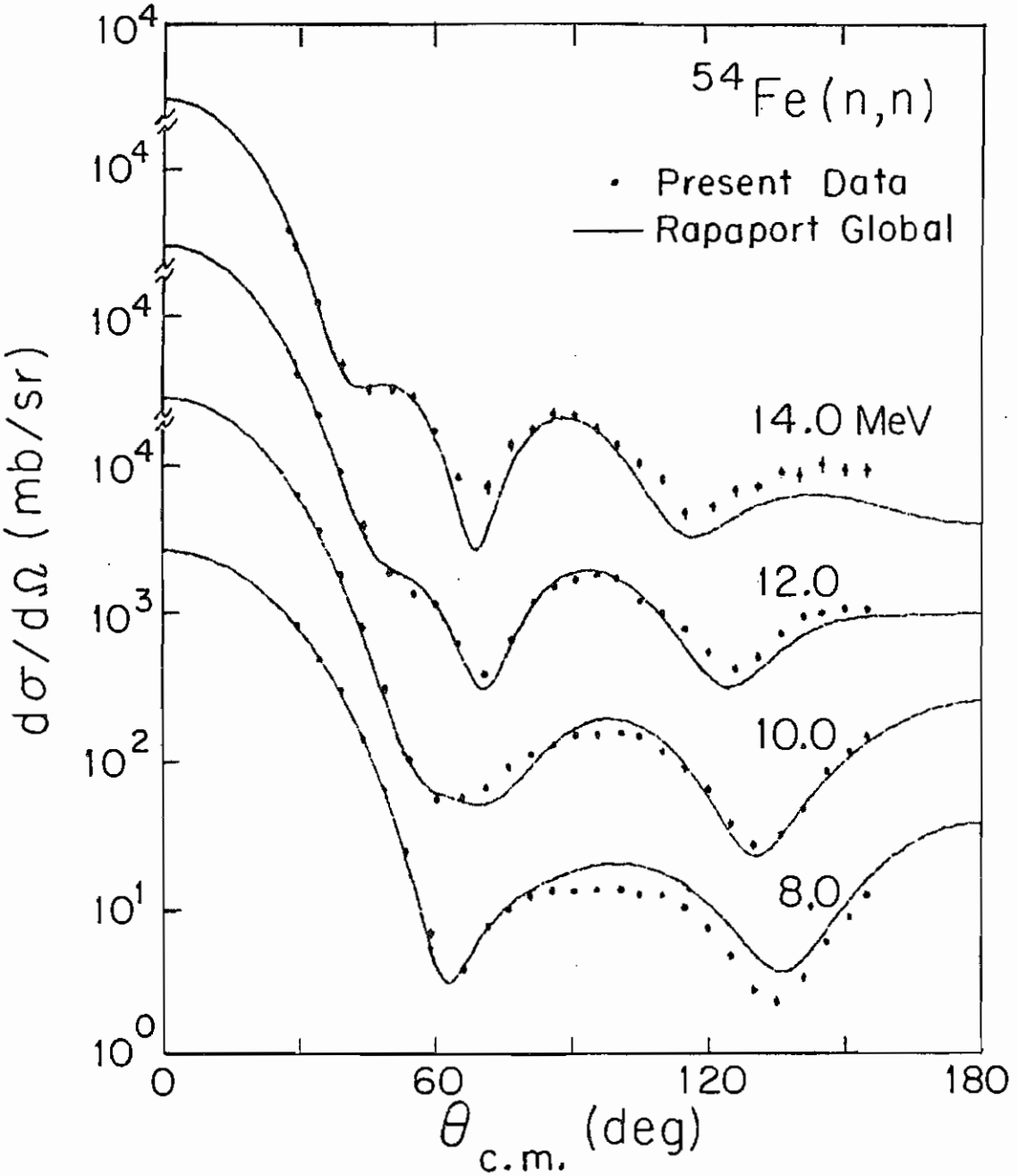

Figure 36 Comparison between the data of the present work for ^{54}Fe and the prediction of Rapaport et al. global parameter set B.

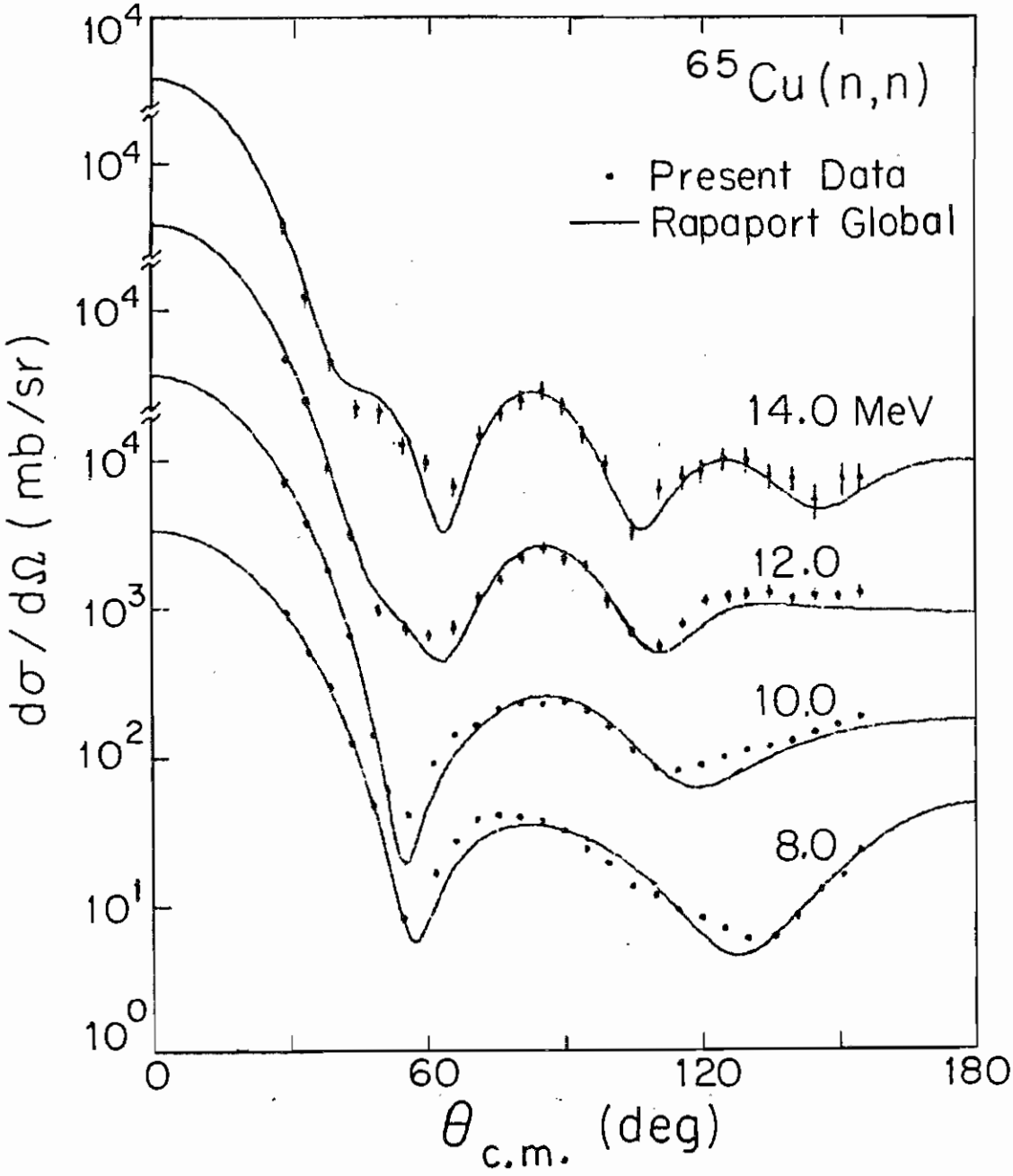

Figure 37 Comparison between the data of the present work for ^{65}Cu and the prediction of Rapaport et al. global parameter set B.

In the remainder of the present chapter we report an attempt to find OMP parameters that predict the data in the present work better than those of the global parameters given above. As mentioned previously, the OMP analyses were carried out in three steps.

4.2.1 Individual searches

Individual searches were carried out for each isotope at each incident energy to obtain OMP parameter sets which give the best fit to each individual angular distribution. The initial parameter set used in the present search was that of Bechetti and Greenlees (1969). The search for optimum parameters was done in such a manner as to avoid the well known ambiguities: $V.r^n$ = constant and $W_D.a_D$ = constant. The spin-orbit parameters V_{so}, r_{so}, and a_{so} were allowed to vary. This variation of the spin-orbit parameters led to improvement of the fits, especially at the back angles. Chi-square per point typically ranged from about 4 at 8 MeV to 1 at 14 MeV. The OMP parameters which gave the best individual fits are given in tables 3-6. The predicted angular distributions resulting from using these parameters are compared with experimental values in figures 38 - 41. As seen in the figures, the fits to the data are very good with no apparent systematic renormalization of these data required.

TABLE 3

Optical potential parameters representing best individual fit to the $^{54}Fe(n,n)$ data

Energy (MeV)	8	10	12	14
V	51.68	51.41	50.45	49.19
r	1.176	1.178	1.178	1.181
a	0.677	0.626	0.627	0.620
W_D	8.47	6.88	5.71	5.17
r_D	1.22	1.25	1.33	1.33
a_D	0.58	0.60	0.57	0.58
W_v	0.60	0.76	2.03	2.51
V_{so}	7.03	6.68	6.52	6.10
r_{so}	1.16	0.94	0.99	0.92
a_{so}	0.63	0.69	0.77	0.64

TABLE 4

Optical potential parameters representing best individual fit to the $^{56}Fe(n,n)$ data

Energy (MeV)	8	10	12	14
V	53.22	51.16	49.74	49.93
r	1.159	1.172	1.176	1.167
a	0.677	0.613	0.617	0.609
W_D	8.36	7.54	6.08	6.02
r_D	1.21	1.20	1.27	1.31
a_D	0.56	0.58	0.62	0.60
W_v	0.58	0.82	1.08	1.51
V_{so}	8.03	6.62	6.30	5.75
r_{so}	1.19	0.92	1.00	0.89
a_{so}	0.56	0.34	0.73	0.41

TABLE 5

Optical potential parameters representing best individual fit to the $^{63}Cu(n,n)$ data

Energy (MeV)	8	10	12	14
V	51.97	52.19	50.59	47.66
r	1.168	1.167	1.158	1.180
a	0.688	0.705	0.635	0.683
W_D	6.38	7.12	3.53	4.79
r_D	1.31	1.18	1.35	1.36
a_D	0.58	0.60	0.60	0.63
W_v	0.46	0.47	3.59	3.46
V_{so}	6.48	5.03	5.58	5.20
r_{so}	1.15	1.05	1.13	0.93
a_{so}	0.47	0.62	0.72	0.56

TABLE 6

Optical potential parameters representing best individual fit to the $^{65}Cu(n,n)$ data

Energy (MeV)	8	10	12	14
V	51.23	50.72	48.44	49.14
r	1.172	1.172	1.188	1.175
a	0.691	0.732	0.639	0.637
W_D	6.15	5.12	3.47	5.10
r_D	1.29	1.26	1.33	1.34
a_D	0.57	0.59	0.60	0.59
W_v	0.19	1.33	3.02	2.30
V_{so}	6.50	5.47	6.48	6.87
r_{so}	1.17	1.12	0.92	0.96
a_{so}	0.46	0.69	0.68	0.70

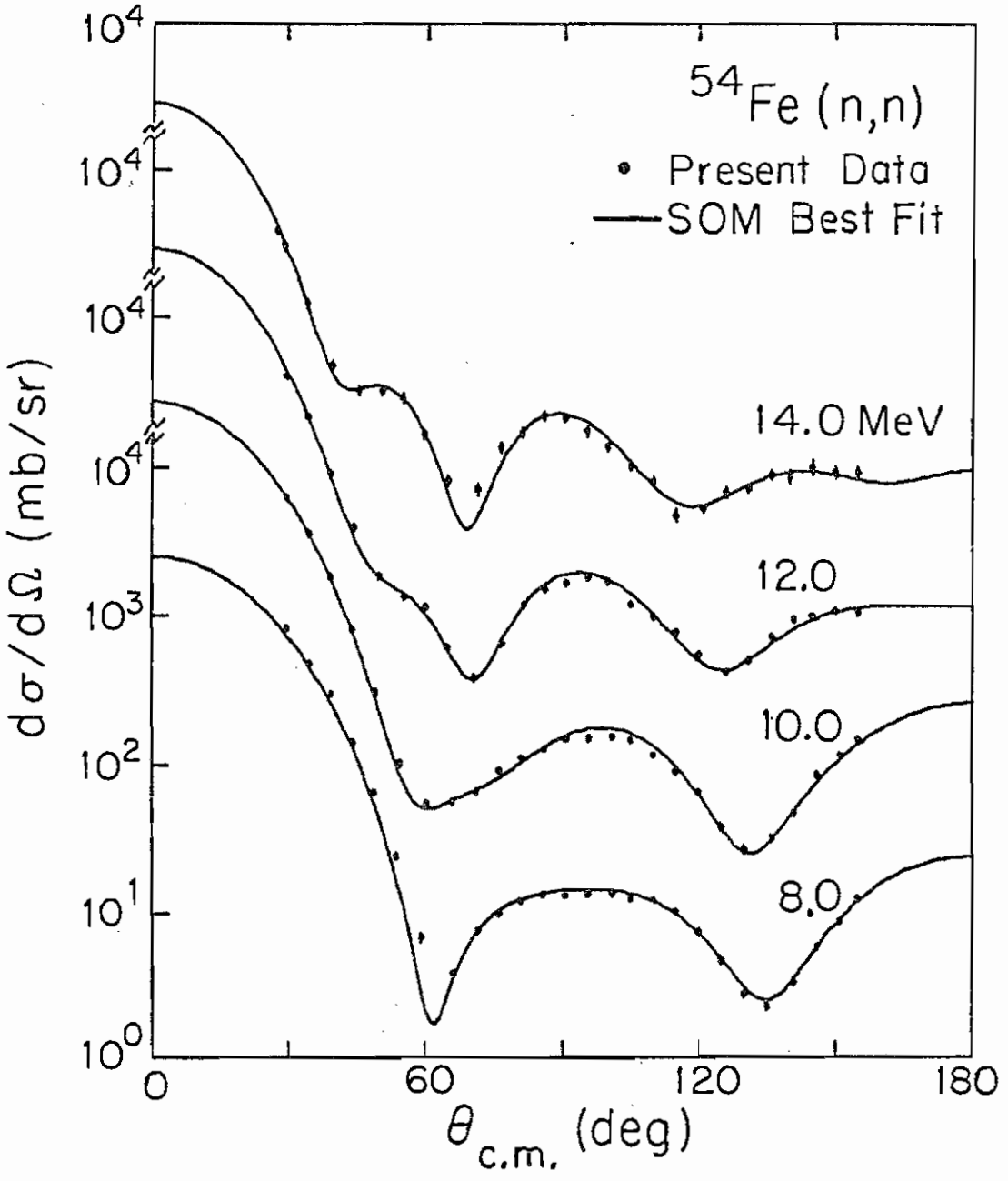

Figure 38 Optical model single-energy best fit to ^{54}Fe differential elastic cross section.

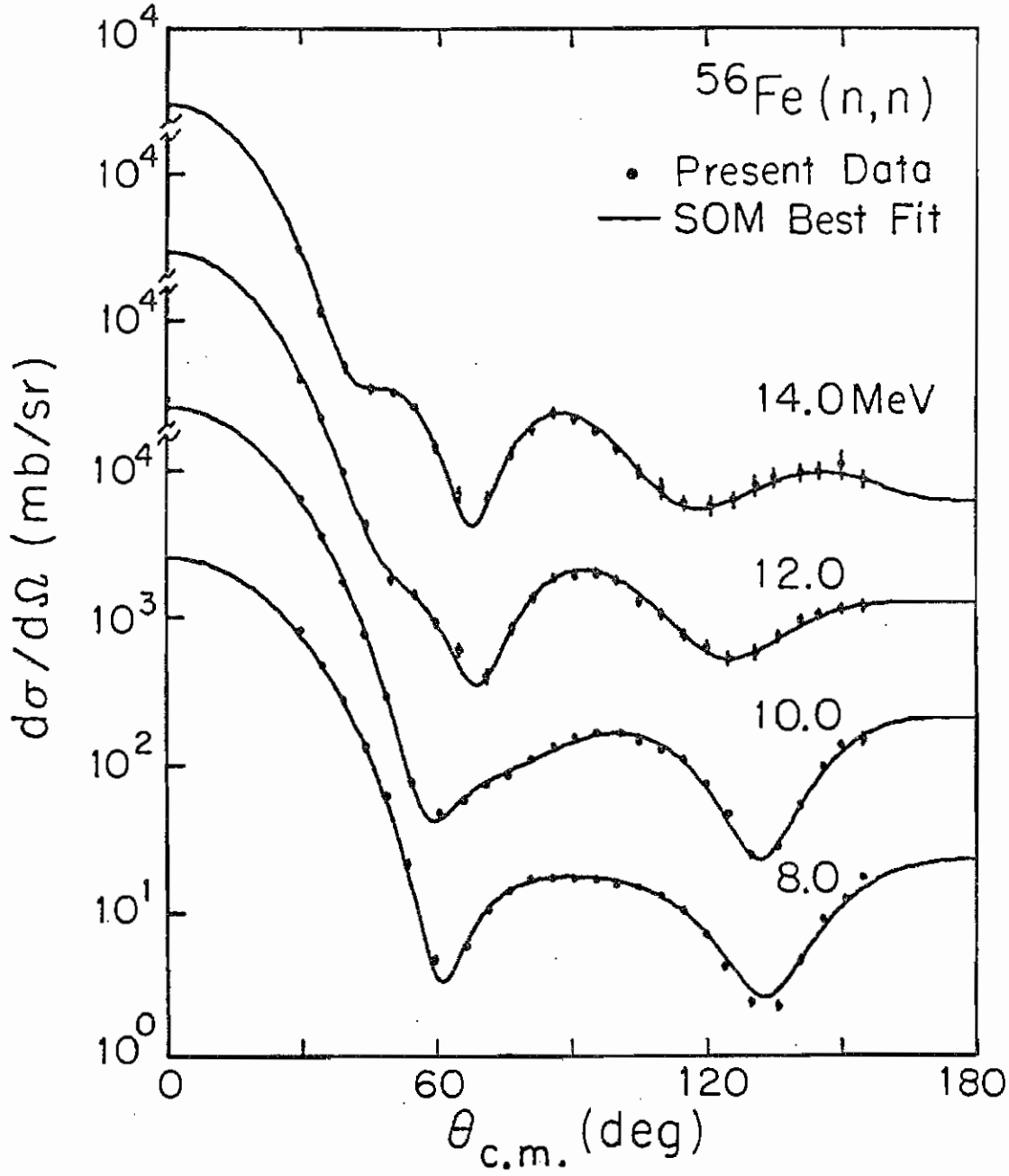

Figure 39 Optical model single-energy best fit to ^{56}Fe differential elastic cross section.

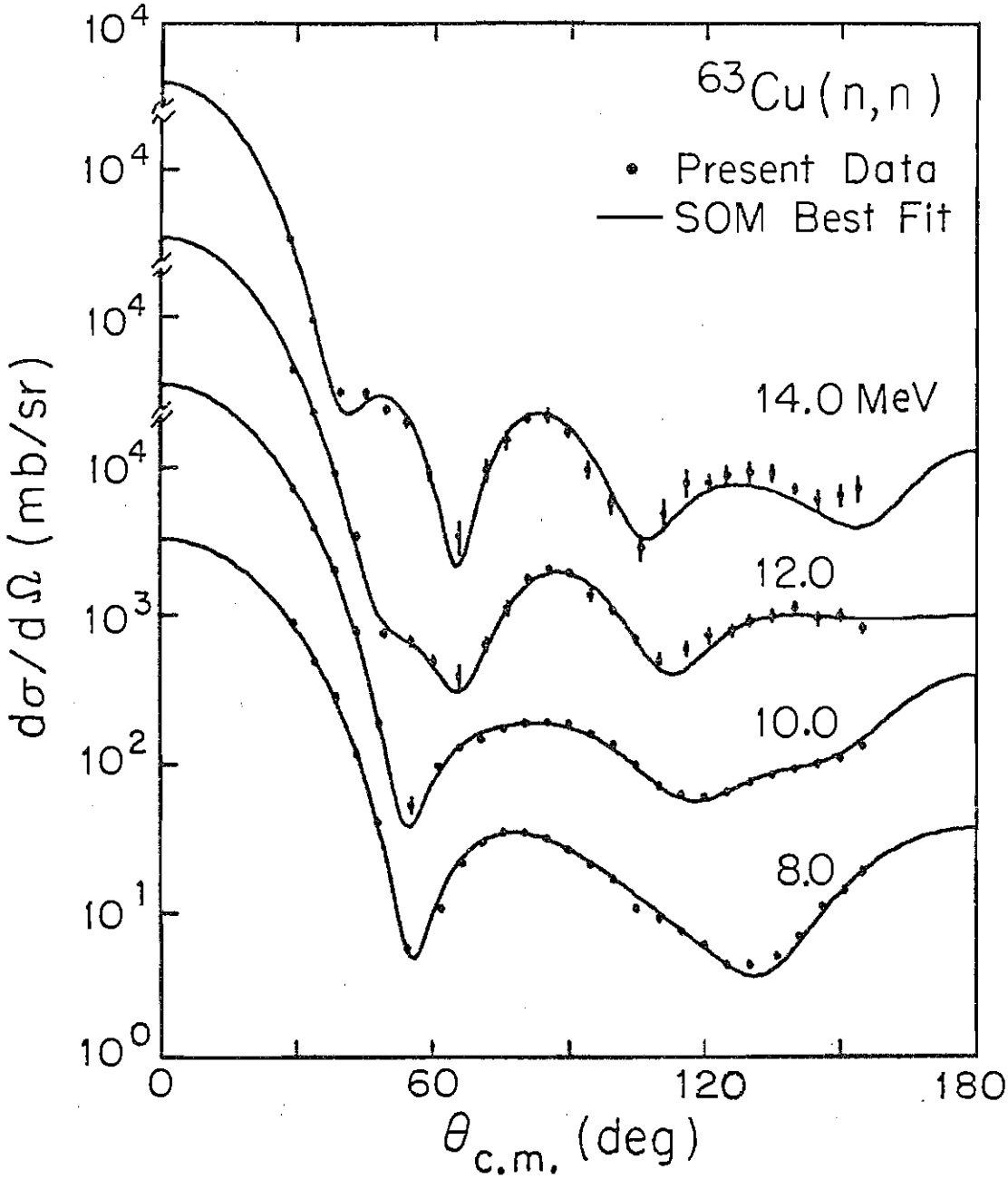

Figure 40 Optical model single-energy best fit to ^{63}Cu differential elastic cross section.

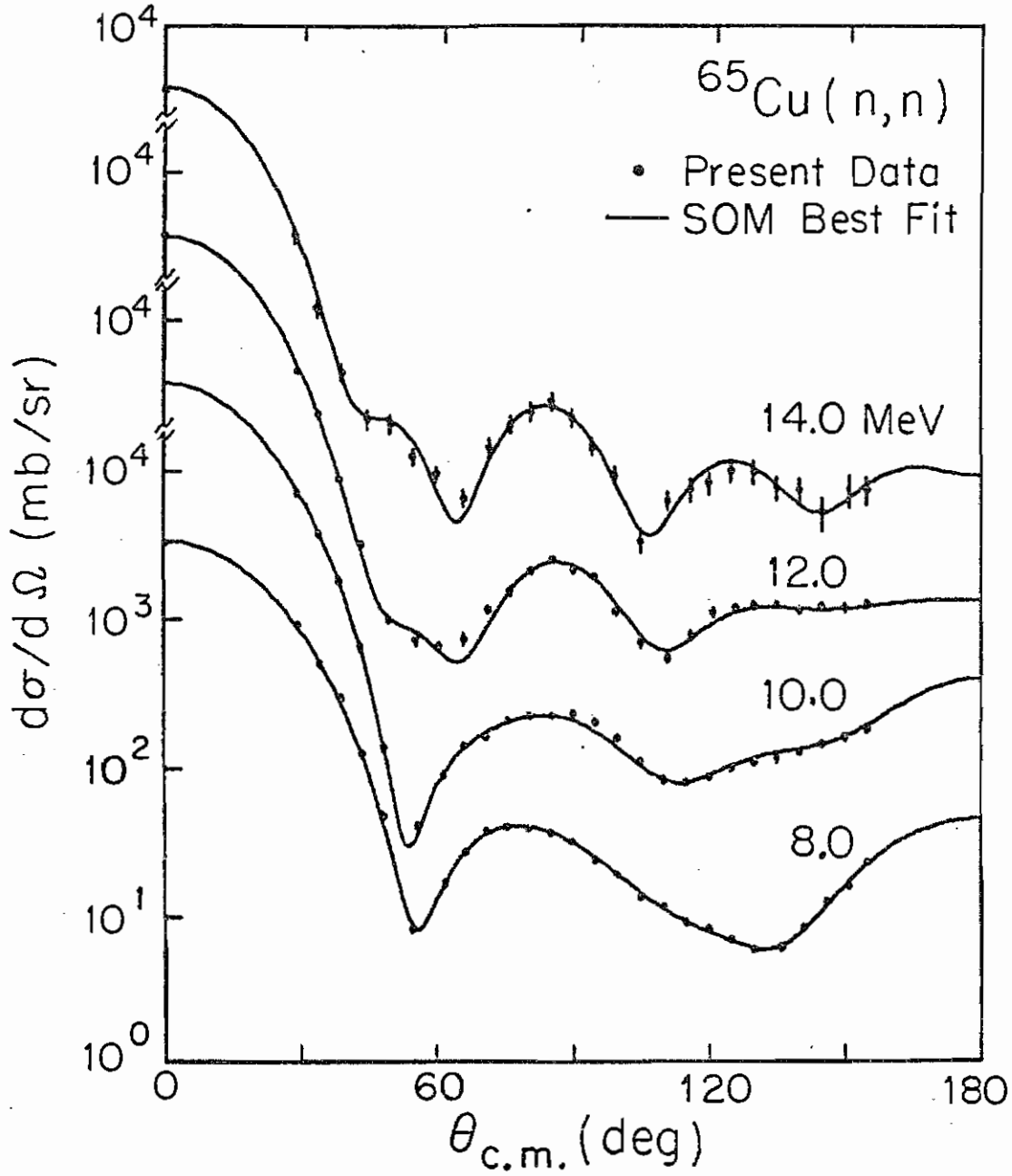

Figure 41 Optical model single-energy best fit to ^{65}Cu differential elastic cross section.

4.2.2 Individual searches with averaged geometries

The geometry parameters resulting from the individual searches were then averaged for each isotope. Each angular distribution was then fitted using the average geometry for each isotope. The resulting fits differ little in quality from those in which the geometry was allowed to vary. Geometry parameters obtained here are listed in table 7. The OMP depths obtained with this fixed geometry are plotted vs. energy in figures 42 - 44.

TABLE 7

Averaged geometry for each Fe and Cu isotope of the present work

	^{54}Fe	^{56}Fe	^{63}Cu	^{65}Cu
r	1.178	1.169	1.168	1.177
a	0.636	0.629	0.678	0.675
r_D	1.28	1.25	1.30	1.30
a_D	0.58	0.59	0.60	0.59
r_{so}	1.02	1.02	1.02	1.02
a_{so}	0.60	0.60	0.60	0.60

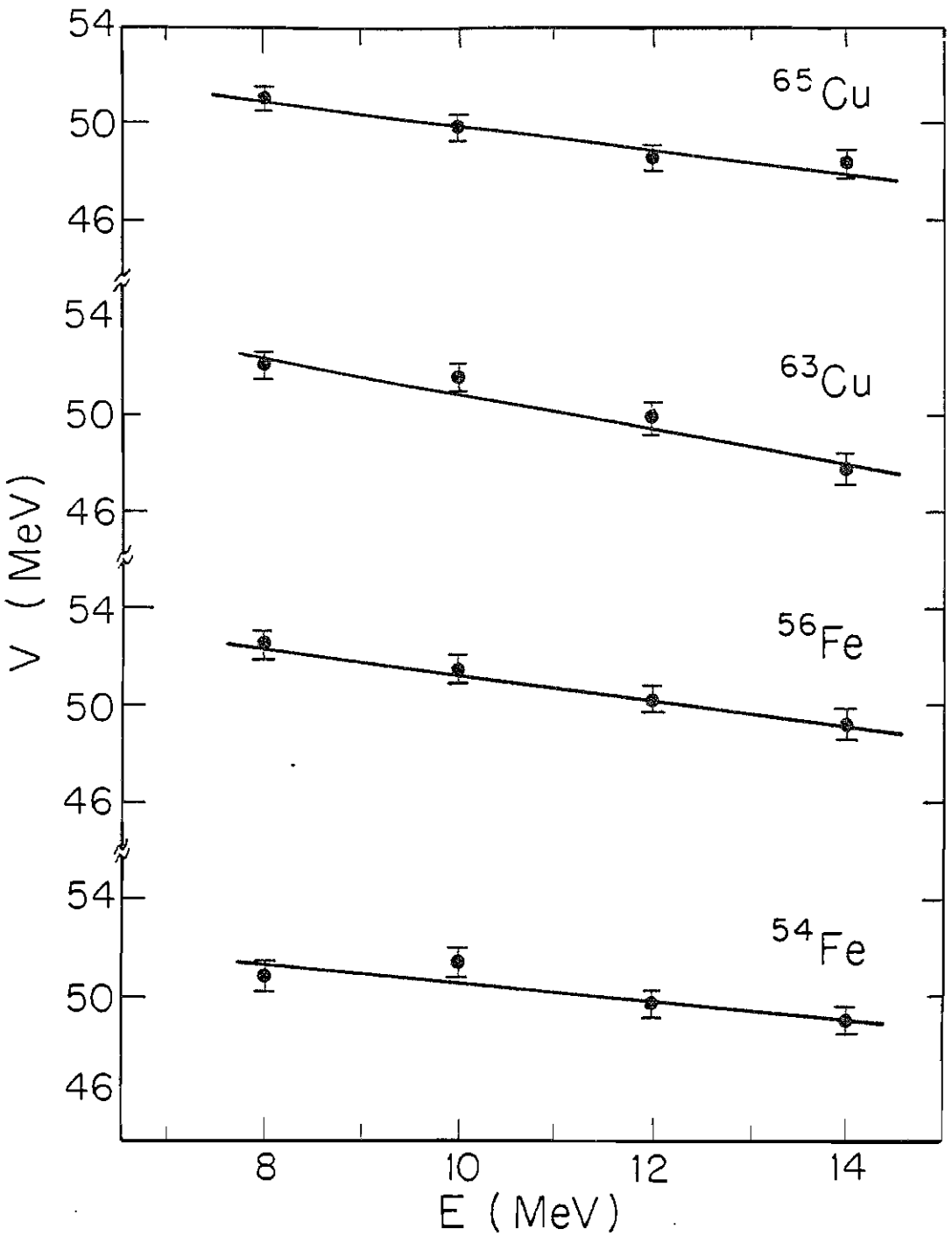

Figure 42 Energy dependence of the real potential V for iron and copper isotopes of the present work.

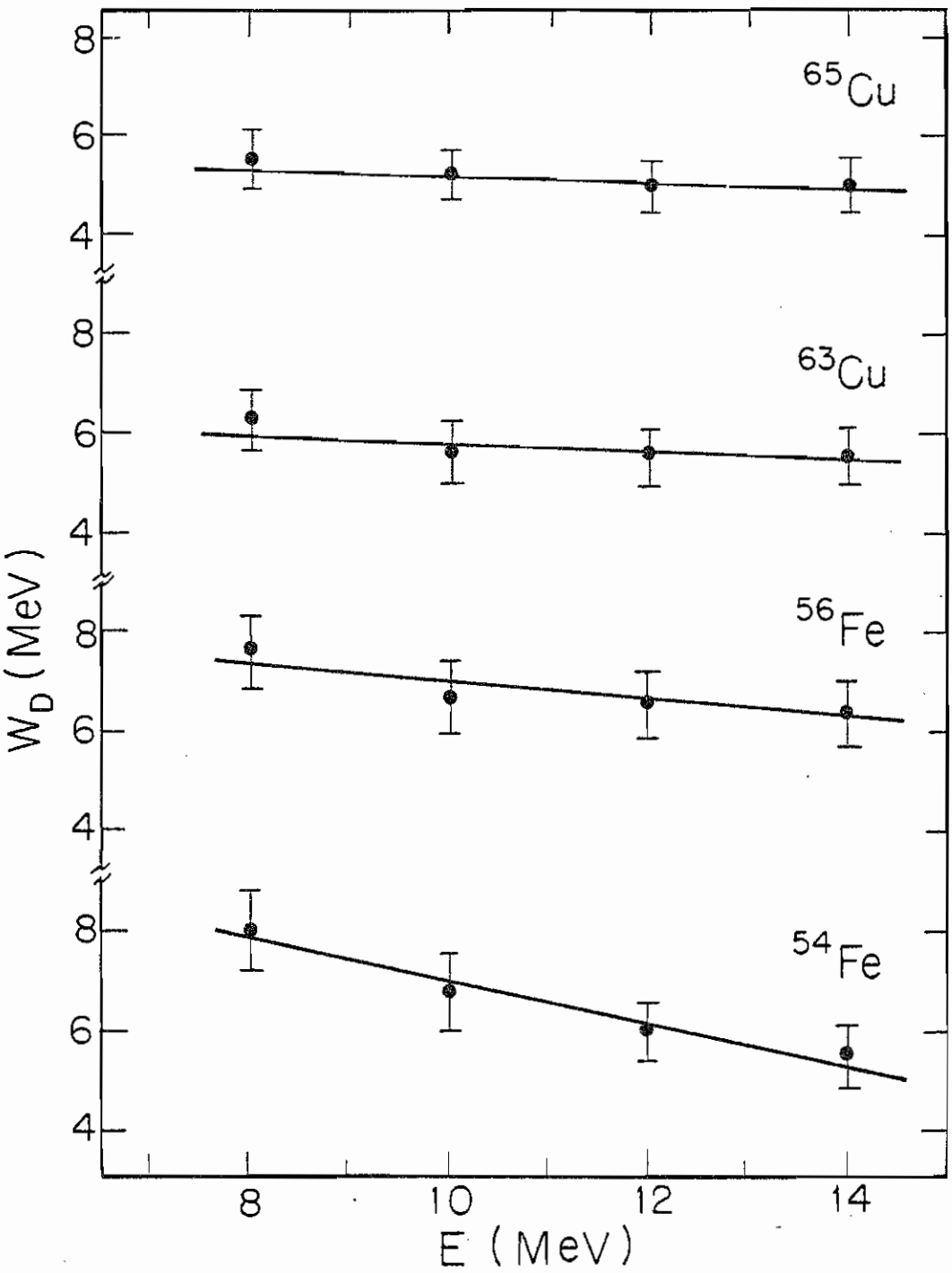

Figure 43 Energy dependence of the imaginary surface potential W_D for iron and copper isotopes of the present work.

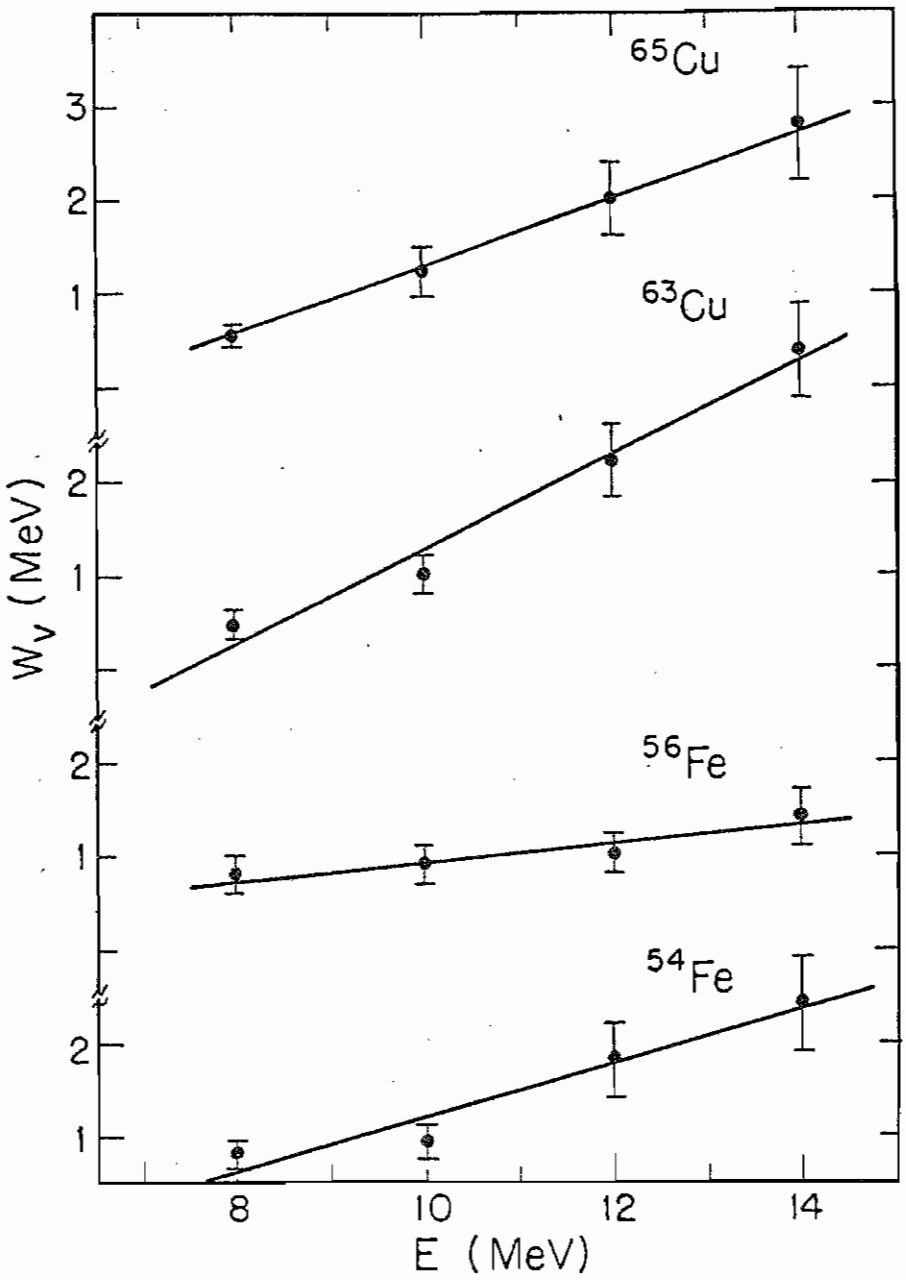

Figure 44 Energy dependence of the imaginary volume potential W_v for iron and copper isotopes of the present work.

4.2.3 Energy dependent OMP parameters

The OMP parameters obtained from the fixed geometry were used to study further the energy dependence of the potentials. As seen in figures 42 - 44, the energy variation for V, W_D and W_v can be expressed as:

$$V = V_0 - \alpha E$$

$$W_D = W_{0D} - \alpha_D E$$

$$W_v = \alpha_v E - W_{0v}$$

The initial values for V_0, W_{0D}, W_{0v} and the energy coefficients of each potential were obtained from figures 42-44. Although the geometry parameters do not differ much from one isotope to another in the present analysis, an overall average geometry set for all isotopes was not obtained at this stage of the search. However, an average spin-orbit parameter set for all isotopes was determined from the earlier individual searches to be V_{so} = 6.08, r_{so} = 1.017 and a_{so} = 0.600, this set was used without variation in these calculations. The search to optimize the well depths including the energy dependent parameters as well as the geometry was carried out for each isotope in the same manner as in the individual searches. The optimized OMP parameters are given in table 8 - 9. The fits resulting from using these parameters are compared with the present data in figures 45-48.

TABLE 8

Energy dependent OMP parameters representing best fit to the Fe isotopes

Isotope	^{54}Fe	^{56}Fe
V	54.05 - 0.340E	55.03 - 0.448E
r	1.173	1.173
a	0.680	0.658
W_D	11.32 -0.326E	9.19 - 0.221E
r_D	1.273	1.282
a_D	0.590	0.591
W_v	0.314E - 3.106	0.249E - 1.744

$V_{so} = 6.108$, $r_{so} = 1.017$, $a_{so} = 0.600$

TABLE 9

Energy dependent OMP parameters representing best fit to the Cu isotopes

Isotope	^{63}Cu	^{65}Cu
V	55.05 - 0.47E	55.99 - 0.564E
r	1.174	1.175
a	0.703	0.702
W_D	8.29 -0.195E	7.20 - 0.049E
r_D	1.315	1.296
a_D	0.591	0.586
W_v	0.361E - 2.482	0.250E - 2.306

$V_{so} = 6.108$, $r_{so} = 1.017$, $a_{so} = 0.600$

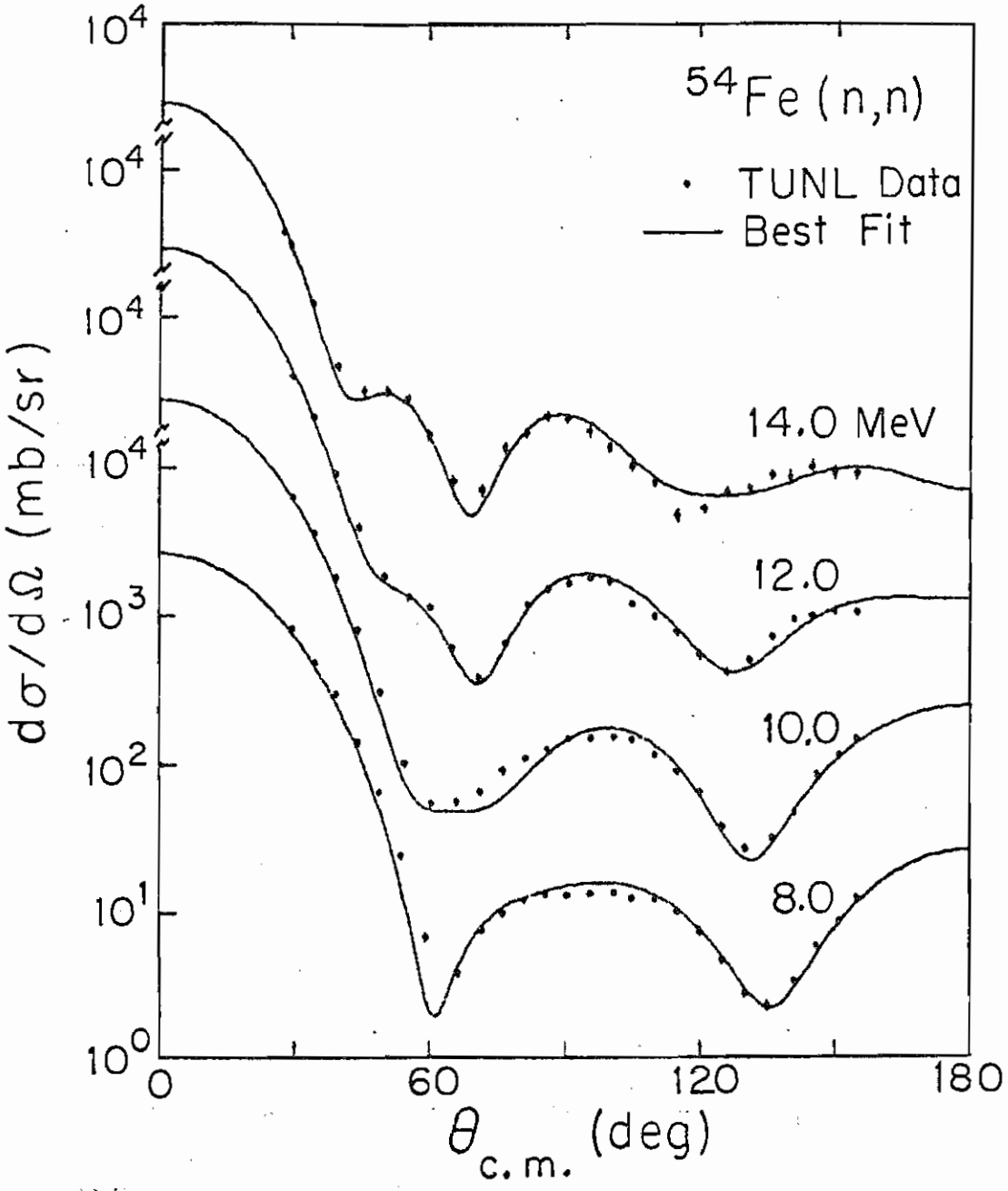

Figure 45 Energy dependent OMP best fit for ^{54}Fe of the present work.

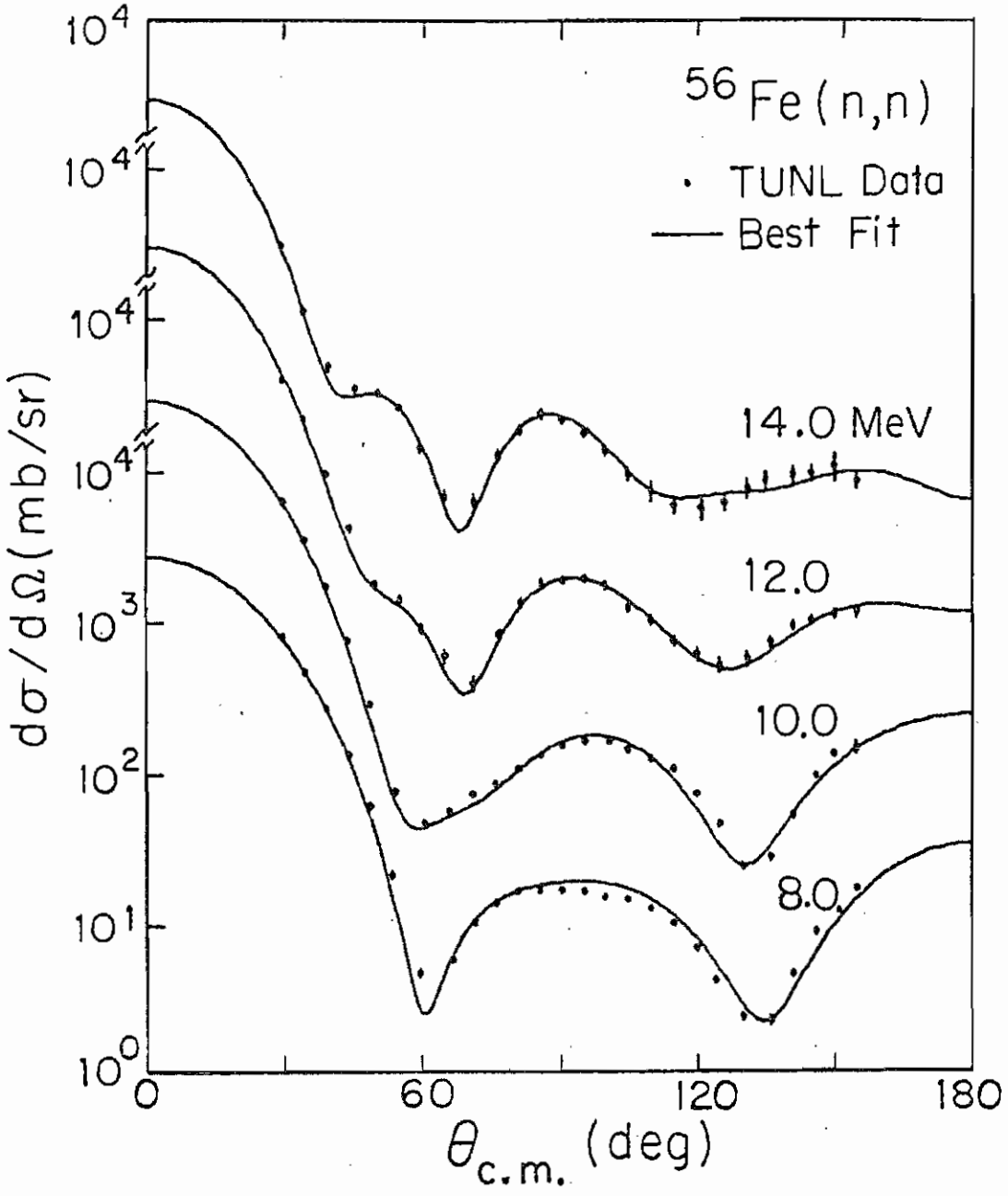

Figure 46 Energy dependent OMP best fit for ^{56}Fe of the present work.

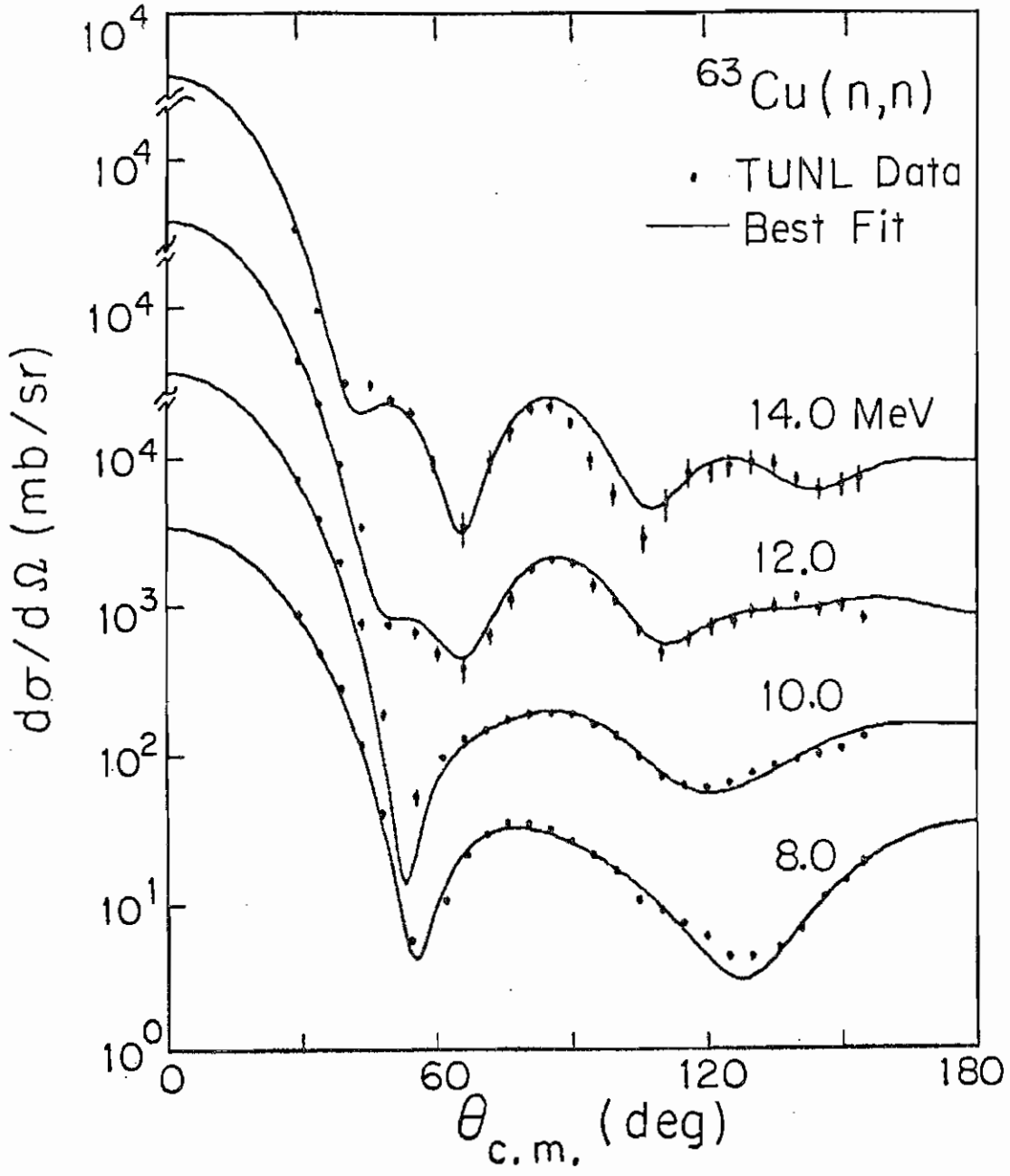

Figure 47 Energy dependent OMP best fit for ^{63}Cu of the present work.

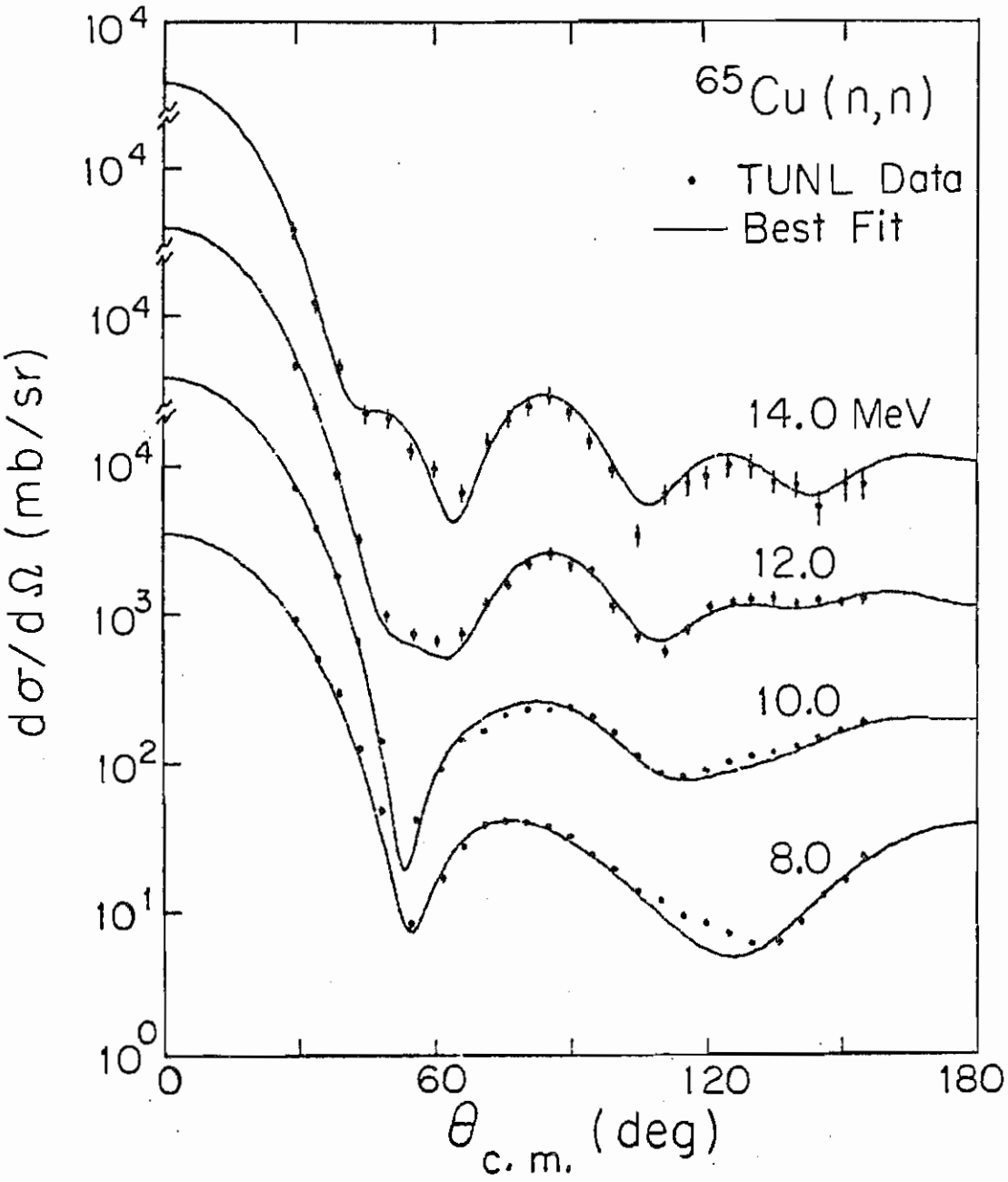

Figure 48 Energy dependent OMP best fit for ^{65}Cu of the present work.

Before searching on all the sixteen sets of iron and copper simultanously, one last preparatory step was taken. For the four nuclei combined, overall average geometry parameters as well as energy dependent coefficients for V, W_D and W_v were obtained by averaging the optimized geometry and energy variation parameters obtained in the previous step. These average parameters were then kept fixed and searches were conducted on the data of each isotope to optimize V_0, W_{0D} and W_{0v}. The results for the optimized values are plotted vs. (N-Z)/A in figure 49. The optimized value of W_v did not change systematically from one isotope to another and so it will be assumed to be independent of (N-Z)/A in the global search below. The parameters V and W_D were assumed to be linearly dependent on the symmetry terms and the fits are shown as the straight line in figure 49.

4.2.4 Global OMP parameters

The average geometry and energy variation parameters for V, W_D, and W_v obtained above were used as starting parameters for the global search on all iron and copper data simultanously. The starting symmetry parameters were obtained from figure 49. The search was carried out to optimize V, W_D and W_v as well as the geometric parameters. In this search the potential strengths V, W_D, and W_v are assumed to

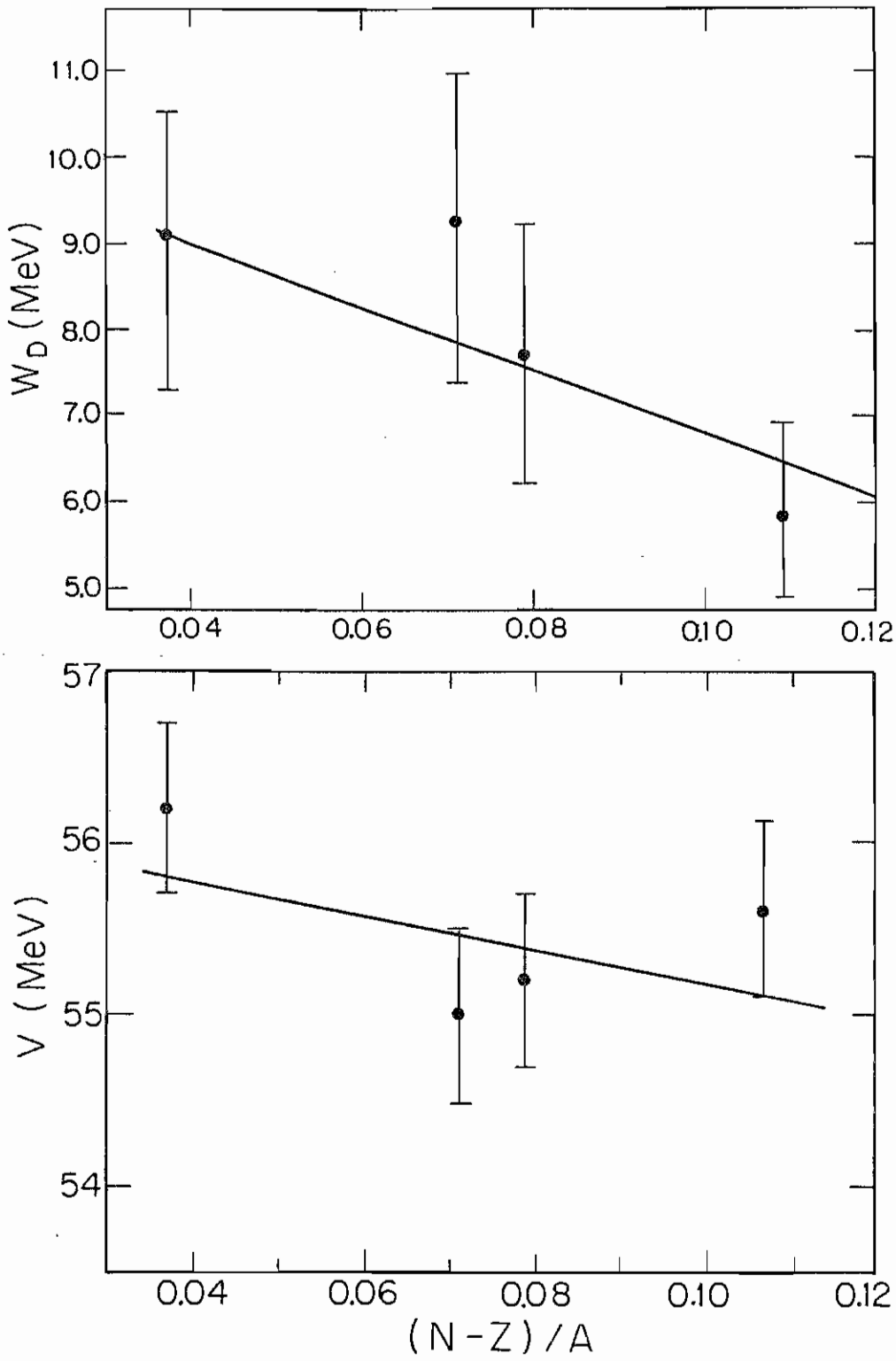

Figure 49 Well depths V and W_D as function of (N-Z)/A.

be expressed as:

$$V = V_0 - \alpha E - V_1(N-Z)/A$$

$$W_D = W_{0D} - \alpha_D E - W_{1D}\,(N-Z)/A$$

$$W_v = \alpha_v E - W_{0v}$$

The global searches were also conducted in such a manner as to avoid the OMP ambiguities mentioned previously. The spin-orbit parameters were kept fixed throughout the global search at the average values obtained above. In the first stage of the global search, only the sixteen data sets of the present work were included. The results of this search are given in table 11. As can be seen, this search resulted in a small positive energy dependence of the surface imaginary potential, i.e. W_D increased with energy. We attribute our finding to the quite small energy and mass ranges covered by the data, making the search quite insensitive to the energy dependence of this term.

A second stage global search was then undertaken to attempt to find parameters which would be consistent with a wider energy and mass range. For this search seven more data sets were included. These data sets were from ^{58}Ni at 8 and 10 MeV, ^{116}Sn and ^{120}Sn at 10 MeV (Guss 1980), ^{208}Pb at 9 and 11 MeV (Rapaport 1979) and ^{58}Ni at 20 MeV (Finlay et al.

1980). Two optimized global parameter sets resulted from searching this broadened data set. These two global sets are given in table 12. As can be seen, these two sets differ in the isobaric spin dependence term of the real and surface imaginary potentials. They also differ considerably from the set obtained in the first stage of the search, principally in the energy dependence of W_D. Figures 50 - 54 show fits to the data of the present work as well as the ^{208}Pb data at 9 and 11 MeV. The fits to the data are the prediction of the global set B. To compare the quality of the fit predicted by each global set, the data of ^{54}Fe and ^{65}Cu at 10 Mev are plotted against the fits of the three global sets in figure 55. The solid lines in the figure are the prediction of the global set of table 11. As can be seen from the figure, a slightly better fit to the data can be obtained from the global set of table 11. The total chi square for set A and set B are the same while it is about 20% better for the global set obtained from the iron and copper isotopes only.

The two global sets (A and B) which resulted from the second stage of the global search were used to calculate the total cross sections for ^{54}Fe, ^{56}Fe, ^{63}Cu and ^{65}Cu in the energy range between 100 keV and 20 MeV. The predicted neutron total cross sections from sets A and B were indistinguishable. Thus, only the results obtained by set A for ^{56}Fe and ^{63}Cu are compared with total cross sections obtained from (BNL325 1976) in figure 56 -57. As can be seen, the

TABLE 11

OMP global parameters for Fe and Cu isotopes

$V = 57.01 - 0.546E - 15.3(N-Z)/A$

$r = 1.175 \quad , \quad a = 0.711$

$W_D = 8.83 + 0.068E - 24.0(N-Z)/A$

$r_D = 1.282 \quad , \quad a_D = 0.580$

$W_v = 0.212E - 2.19$ or Zero whichever is greater

$V_{so} = 6.108 \quad , \quad r_{so} = 1.017 \quad , \quad a_{so} = 0.600$

TABLE 12

OMP global parameters

Set A

$V = 57.5 - 0.476E - 23(N-Z)/A$

$r = 1.165$, $a = 0.720$

$W_D = 10.37 - 0.192E - 16(N-Z)/A$

$r_D = 1.272$, $a_D = 0.593$

$W_v = 0.231E - 2.164$, or Zero whichever is greater

$V_{so} = 6.108$, $r_{so} = 1.017$, $a_{so} = 0.600$

Set B

$V = 56.23 - 0.474E - 16.4(N-Z)/A$

$r = 1.173$, $a = 0.711$

$W_D = 10.89 - 0.204E - 19.6(N-Z)/A$

$r_D = 1.282$, $a_D = 0.594$

$W_v = 0.231E - 2.164$, or Zero whichever is greater

$V_{so} = 6.108$, $r_{so} = 1.017$, $a_{so} = 0.600$

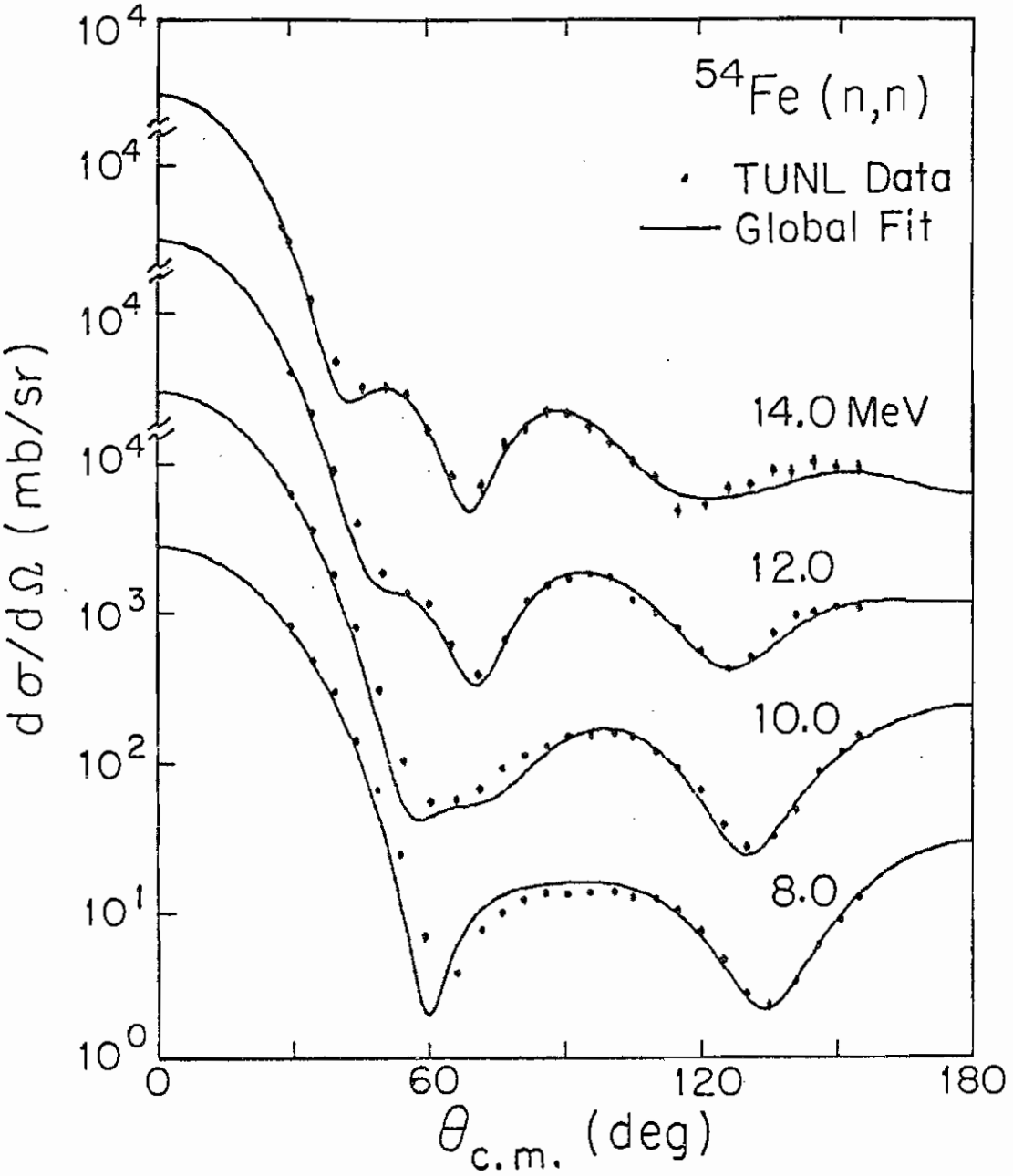

Figure 50 Optical model global fit to ^{54}Fe differential elastic cross section.

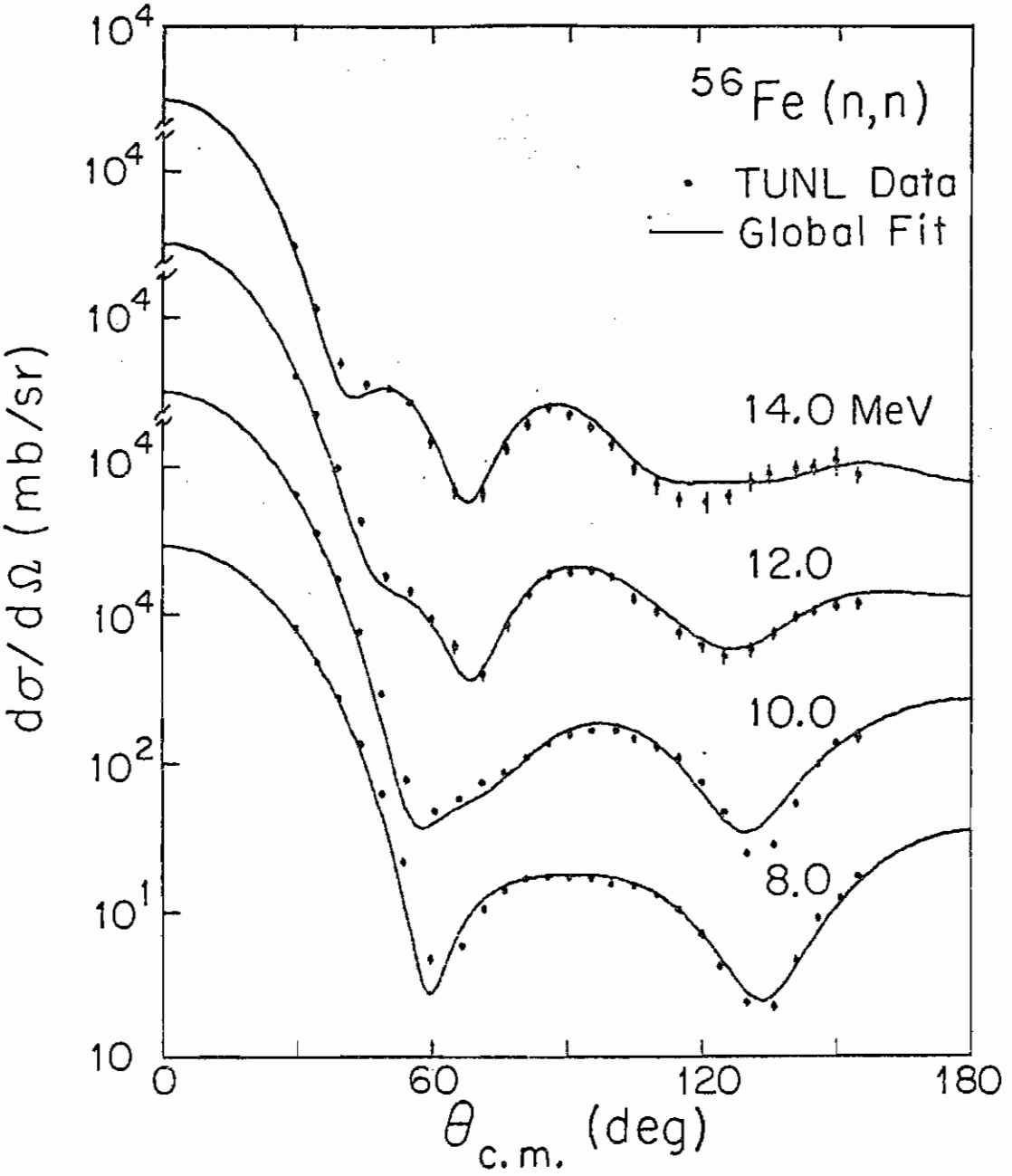

Figure 51 Optical model global fit to ^{56}Fe differential elastic cross section.

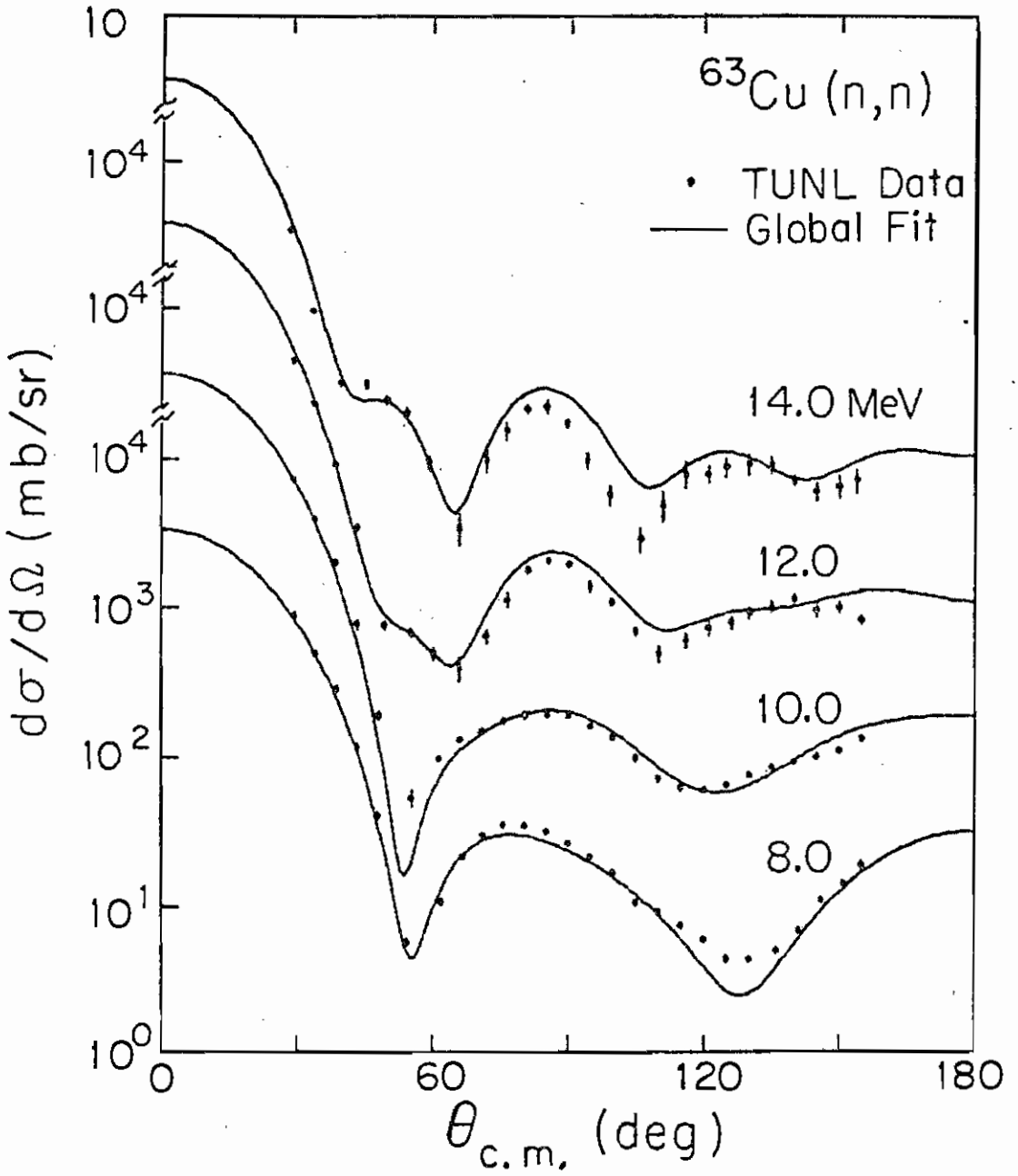

Figure 52 Optical model global fit to ^{63}Cu differential elastic cross section.

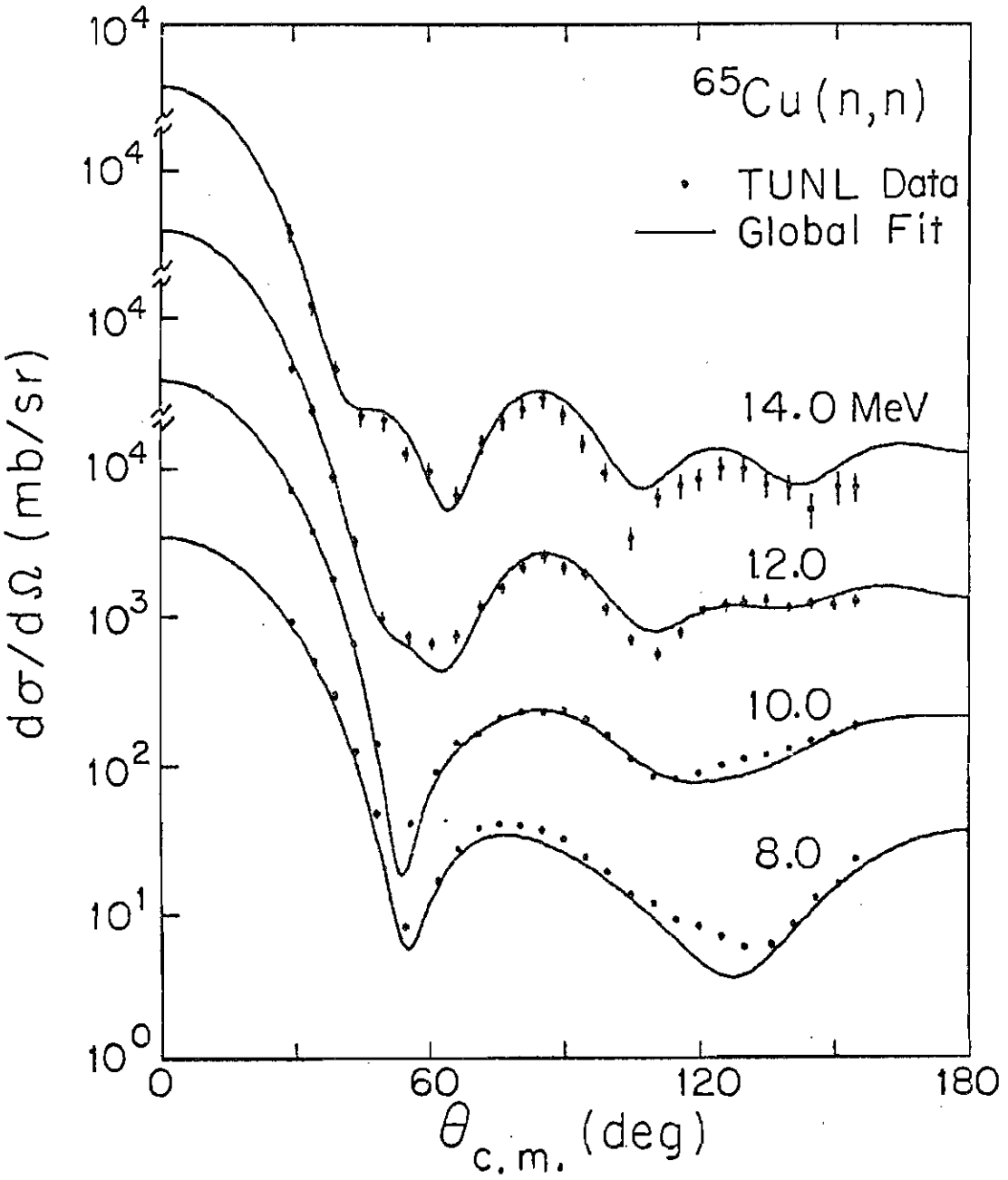

Figure 53 Optical model global fit to ^{65}Cu differential elastic cross section.

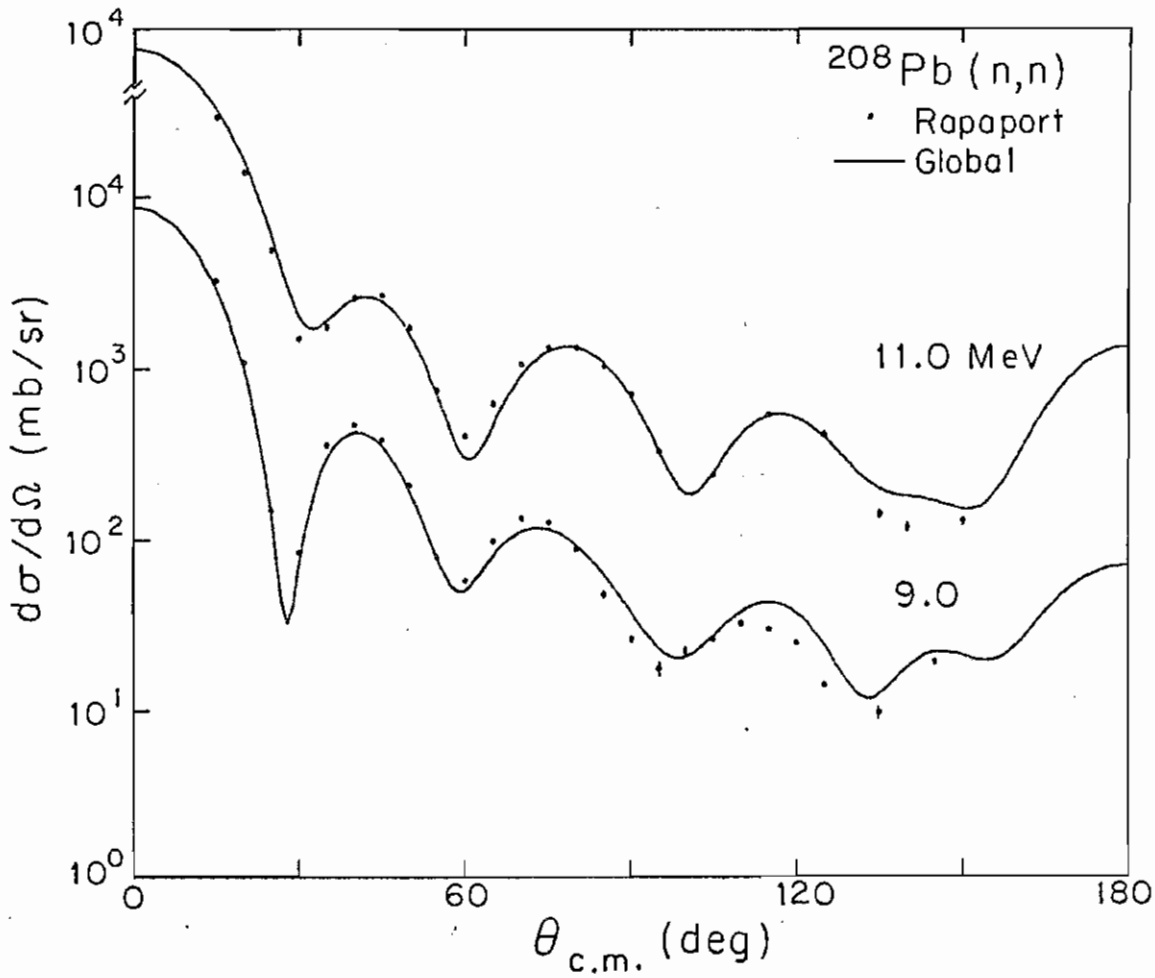

Figure 54 Optical model global fit to ^{208}Pb differential elastic cross section.

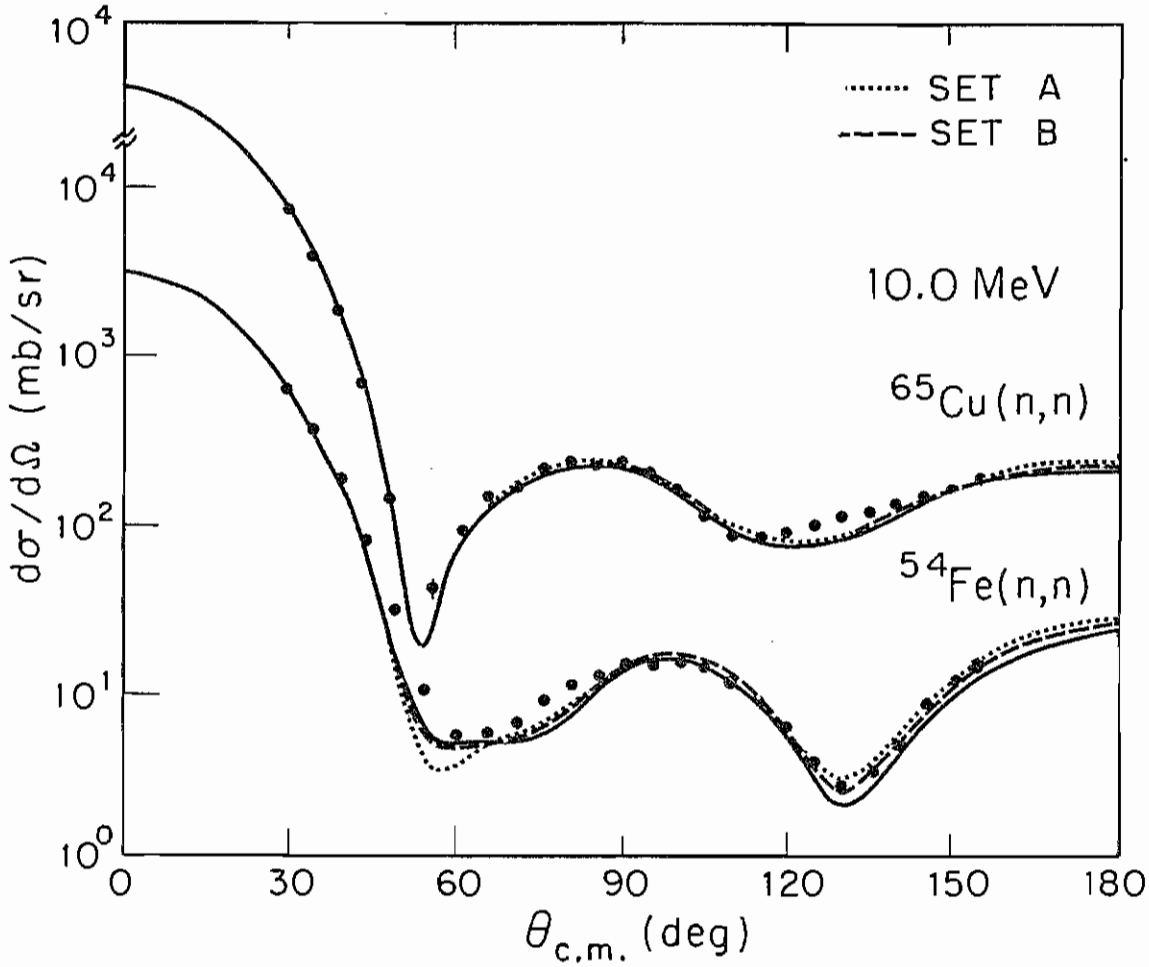

Figure 55 Comparison between the different OMP global fits to ^{54}Fe and ^{65}Cu data at 10 MeV (see text).

global sets predicted the total cross sections reasonably well except for Cu at energies below 2 MeV in which case the predictions are slightly high. In addition, the potential scattering radii (R') calculated at 10 keV have been compared with available data (BNL325 1973) and the results of this comparison are given in table 13. It must be noticed that in the case of Cu isotopes the present values of (R') are compared with (R') from BNL325 for natural Cu.

TABLE 13

Potential scattering radii

	^{54}Fe	^{56}Fe	^{63}Cu	^{65}Cu
$R'_{present}$	5.81	5.91	6.82	6.90
R'_{BNL}	5.6±0.6	6.1±0.7	7.1±0.2	7.1±0.2

The geometries of the global sets obtained here do not differ much from those obtained by Rapaport et al. and Bechetti and Greenlees. The isobaric spin dependence term of

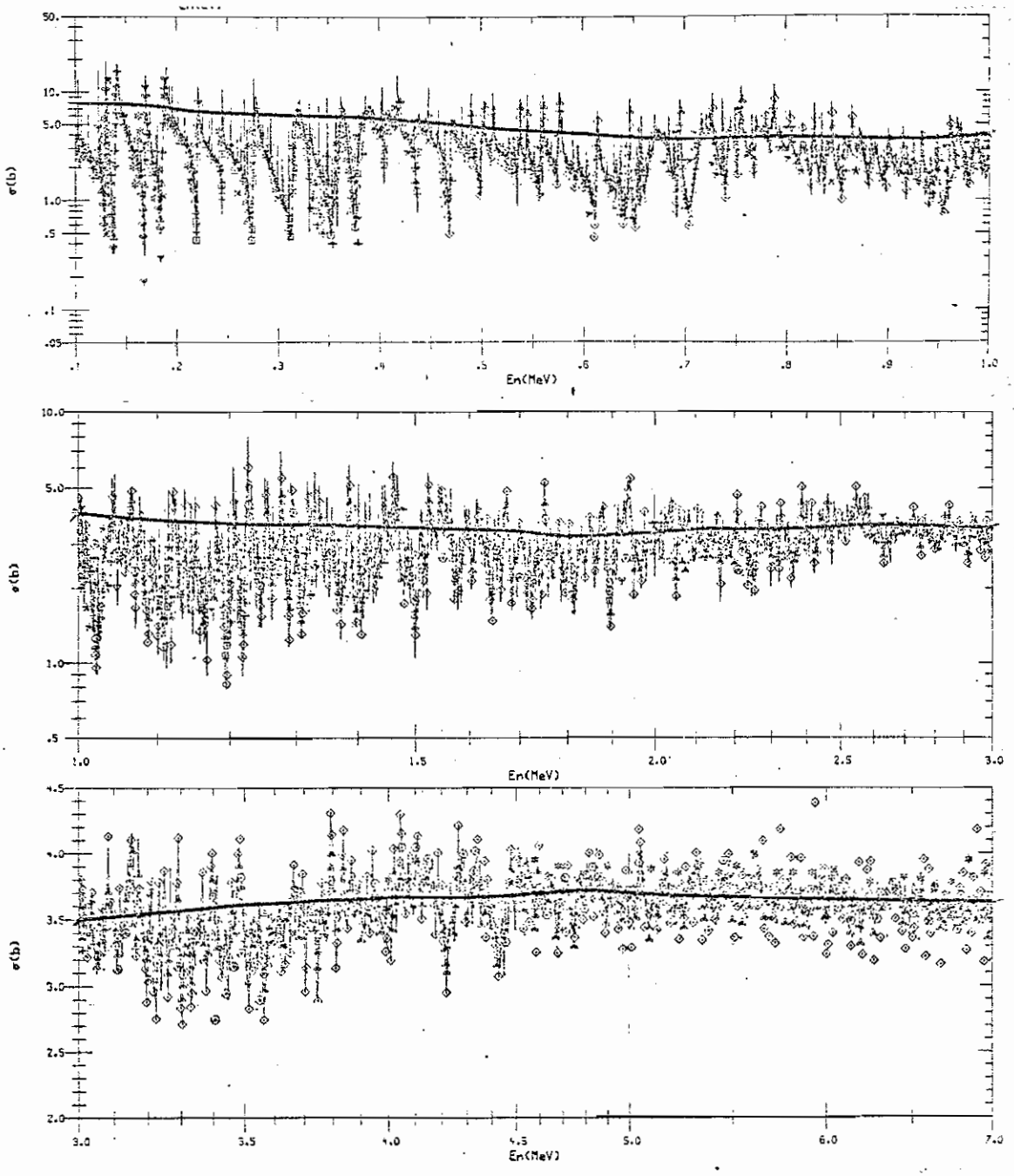

Figure 56 Comparison between total cross section predicted for ^{56}Fe by set A and the experimental total cross section for natural iron (see text).

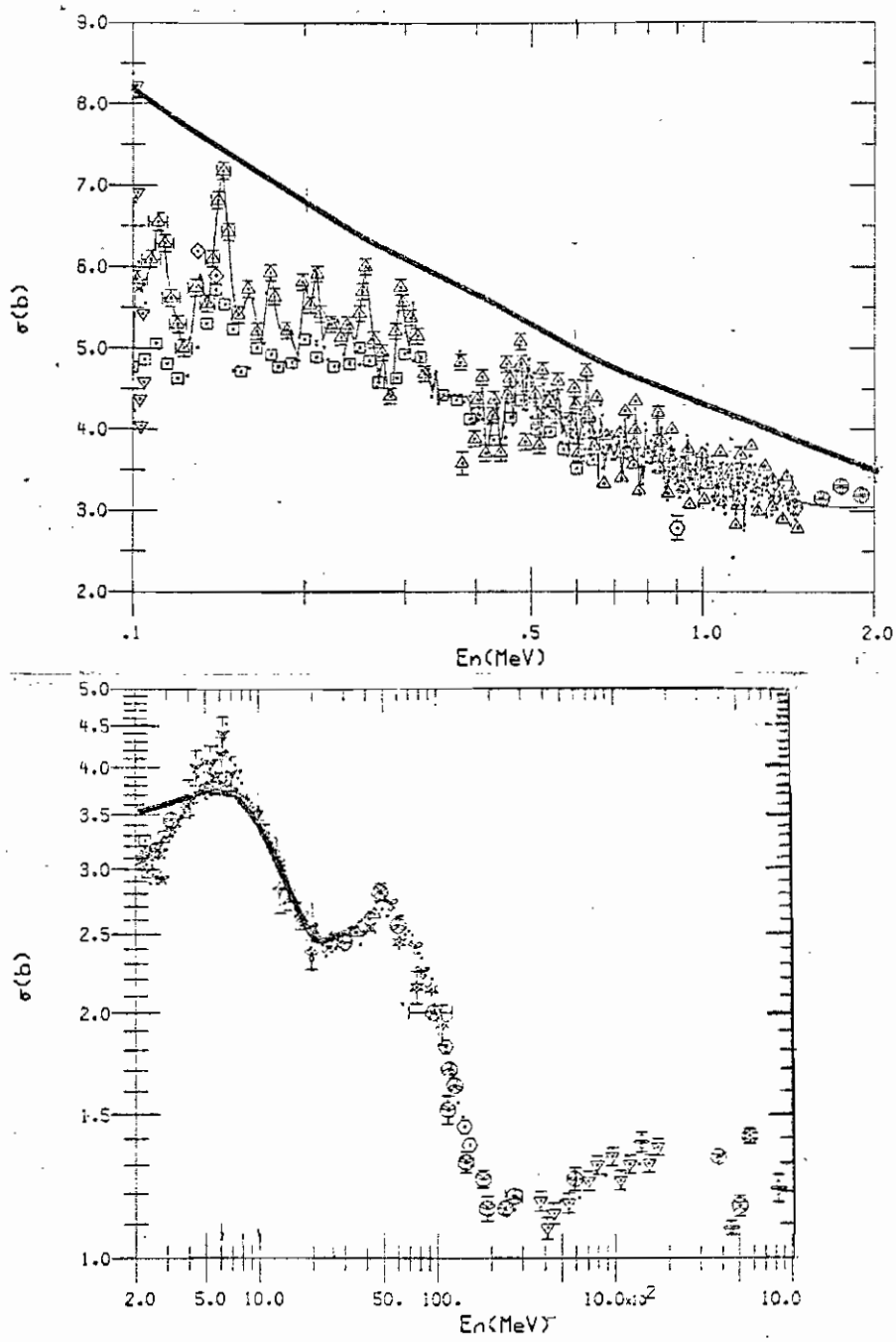

Figure 57 Comparison between total cross section predicted for ^{63}Cu by set A and the experimental total cross section for natural copper (see text).

the real and imaginary surface potential of the set A (V_1 = 23, W_{1D} = 16) are comparable with values of V_1 = 24 and W_{1D} = 12 obtained by Bechetti and Greenlees and V_1 = 22.7 - 25.5 and W_{1D} = 9 - 13 obtained by Rapaport et al. The real isobaric spin potential as well as the corresponding imaginary potential of set B (V_1 = 16.4 and W_{1D} = 19.5) compared favorably with those from still other analyses. Holmqvist (Holmqvist 1968) obtained V_1 = 14 $\pm$ 4 MeV and W_{1D} = 25 $\pm$ 7.5 MeV from the analyses of the neutron elastic scattering cross sections of several elements at several incident energies. Further, Dukarevich (Dukarevich et al. 1967) found V_1= 17$\pm$2 and W_{1D} = 26$\pm$9 from the analyses of total cross-section measurements on a number of isotopes at 14.2 MeV.

It is also interesting to compare the value of V_1 and W_1 obtained in the present work with those from proton scattering analysis. Bechetti and Greenlees found V_1 = 24 MeV and W_{1D} = 12 MeV from the systematic analyses of elastic differential cross sections for a wide range nuclei with A>40 and at energies below 50 MeV. Menet (Menet et al. 1971) deduced V_1 = 26.4 MeV and W_D = 15.5 MeV from analyses similar to that of Bechetti and Greenlees extending from 30 to 60 MeV. Perey (Perey 1963) found V_1 = 27 MeV and Ws'1D. = 48 MeV in the 9 to 22 MeV energy interval. As can be seen from this comparison, the average values of $V_1$and Ws'1D. obtained from the protons analyses are only slightly higher than the corresponding values obtained in our set B.

4.3 PROPERTIES OF THE GLOBAL OPTICAL POTENTIAL

The isobaric spin as well as the energy dependence of the optical potential were investigated above using the optimum values of V and W. However, because of the ambiguities of V due to its dependence on r, and W_D due to its dependence on a_D, Feschbach suggested the use of the volume integral as a measure of the real part of the potential V as well as the imaginary surface part W_D (Feschbach 1958). Later Greenlees and collaborators (Greenlees et al. 1968) calculated the optical potential from the nucleon-nucleon interaction. They found that the volume integral per nucleon of the real central potential (J_v/A) and its rms radius $\langle r_R^2 \rangle^{1/2}$ are the significant quantities in this formalism. These quantities were calculated in the present work and compared with available values.

4.3.1 Volume integral

The volume integral per nucleon of the real central potential (J_v/A) has been calculated for several neutron incident energies for each isotope. The calculations were carried out using both global set A and B obtained in the present work. The results of this calculations at 10 MeV are plotted as function of (N-Z)/A in figure 58. Next, the volume integral was assumed to be linearly dependent on (N-Z)/A, the straight line resulting from a least-square fit

of the points can be expressed as

$$J_v/A = (454\pm30).(1 - 1.05\ (N-Z)/A) \quad MeV\ fm^3$$

which gives the isobaric strength of 477 ± 32 . This value is in excellent agreement with the value of (470 ± 40) obtained by Holmqvist (Holmqvist et al 1972).
The result also agreed with the expression:

$$J_v/A = (495 \pm 30).(1 - (0.95 \pm 10\%).(N-Z)/A) \quad MeV.fm^3$$

obtained by Ferrer (Ferrer et al. 1977).

In figure 59 the volume integral per nucleon (J_v/A) in $MeV.fm^3$ is plotted as a function of the incident energy. As seen, the linear variation can be expressed as

$$J_v/A = J_0/A - 4.0E$$

The energy coefficient is slightly higher than the value of 2.8 obtained by Rapaport (Rapaport et al 1979). The results for our set B were within one percent of those given here for set A.

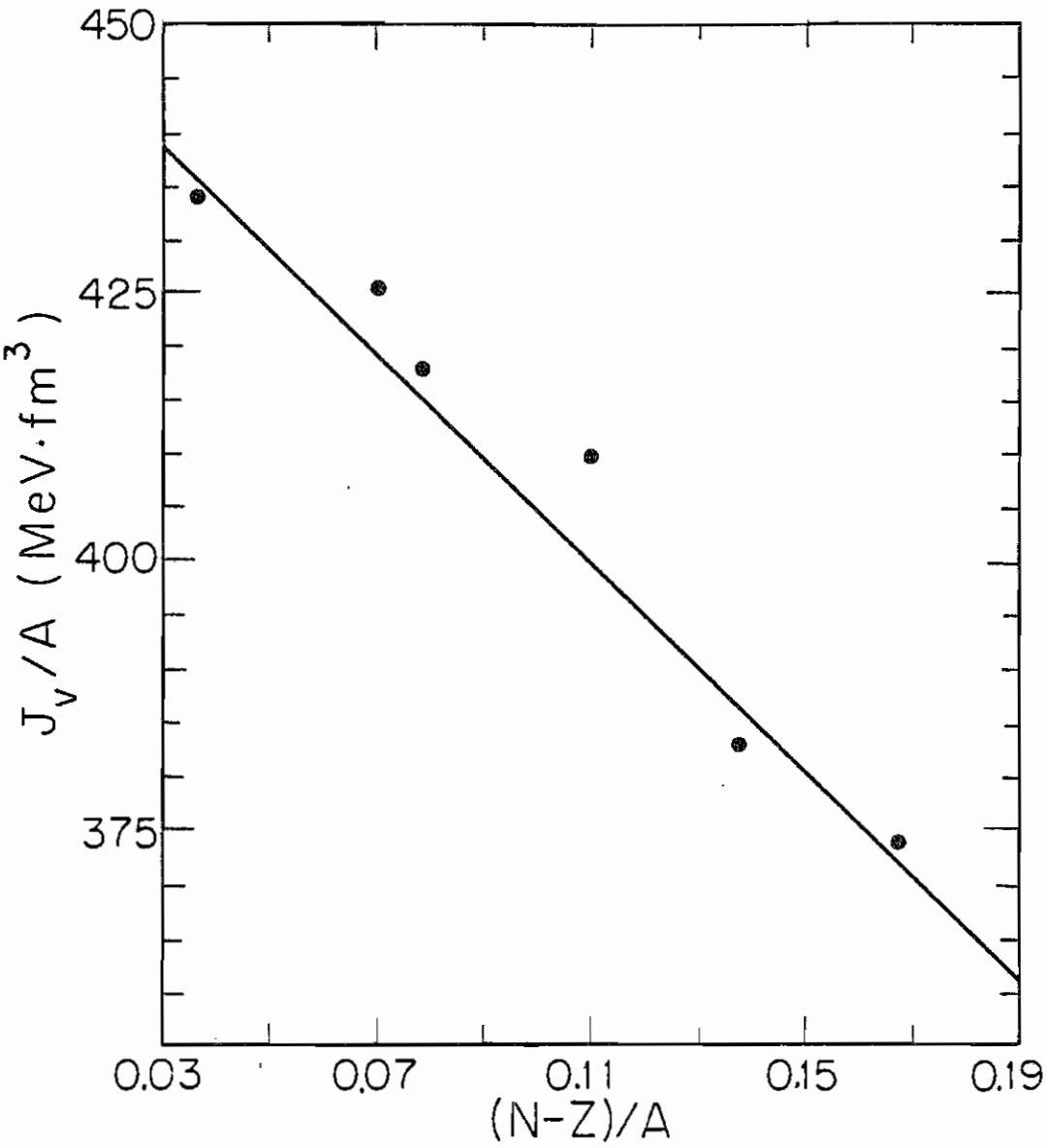

Figure 58 Volume integral per nucleon J_v/A of the real central potential vs. (N-Z)/A.

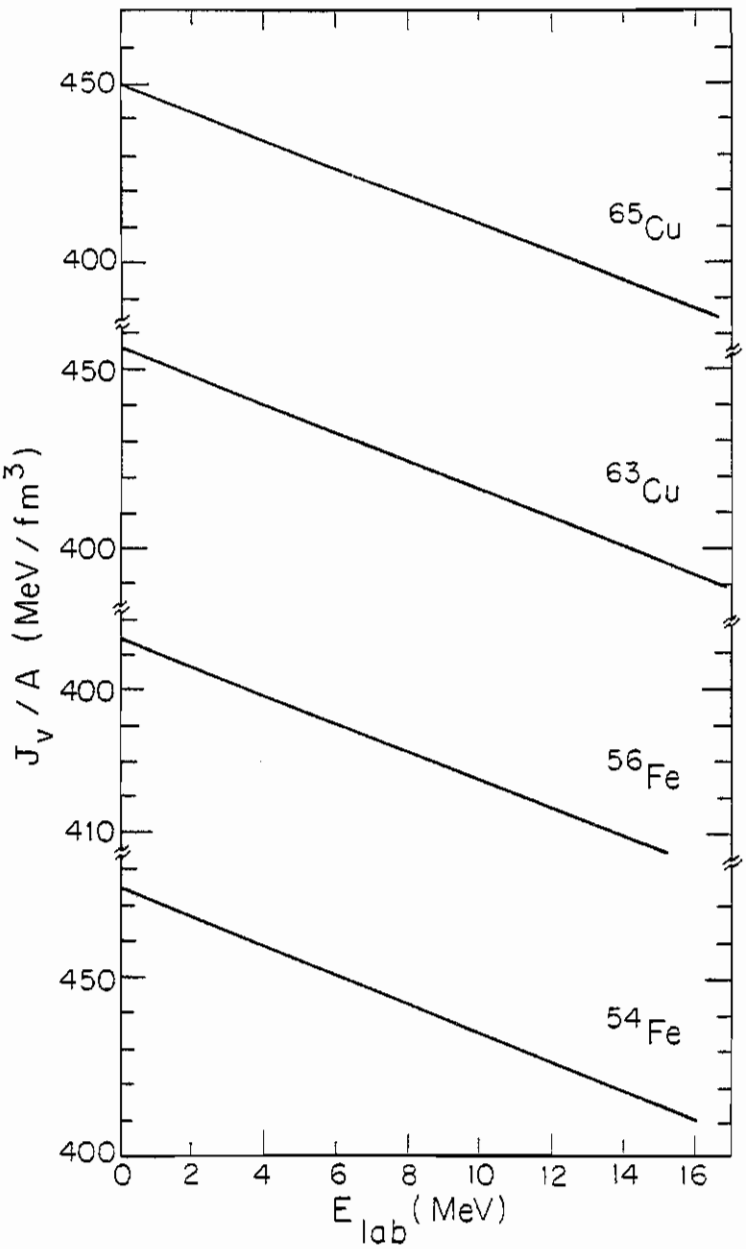

Figure 59 Real volume integral per nucleon J_v/A Mev.fm^3 vs. incident energy E.

4.3.2 Nuclear radii

The rms radius $\langle r^2_R \rangle^{1/2}$ of the real central potential was calculated using global set A of the present work and plotted as a function of $A^{1/3}$ in figure 60. The results were compared with the values obtained by using global set B of Rapaport (open circle). Holmqvist (1968) obtained the following expression for rms radius of the real central potential

$$\langle r^2_R \rangle^{1/2} = 0.96 + 0.89A^{1/3}$$

The values of $\langle r^2_R \rangle^{1/2}$ obtained from the above expression are also shown in figure 60. The rms radius $\langle r^2_R \rangle$ obtained in the present work for tin isotopes also compares well with the value of 5.33 obtained by Boyd (Boyd et al 1971) from the analysis of 16 MeV proton differential cross sections of tin isotopes. As can be seen from the figure, these sets of values agree quite well with the present result.

The mean square (ms) radius of the point matter distribution $\langle r^2_m \rangle$ has been estimated in the fromwork of the folding model (Greenlees et al. 1968) from the mean square radius of the real potential $\langle r^2_R \rangle$. The ms radius $\langle r_{2m} \rangle$ is related to $\langle r_{2R} \rangle$ as follows (Thomas et al. 1973):

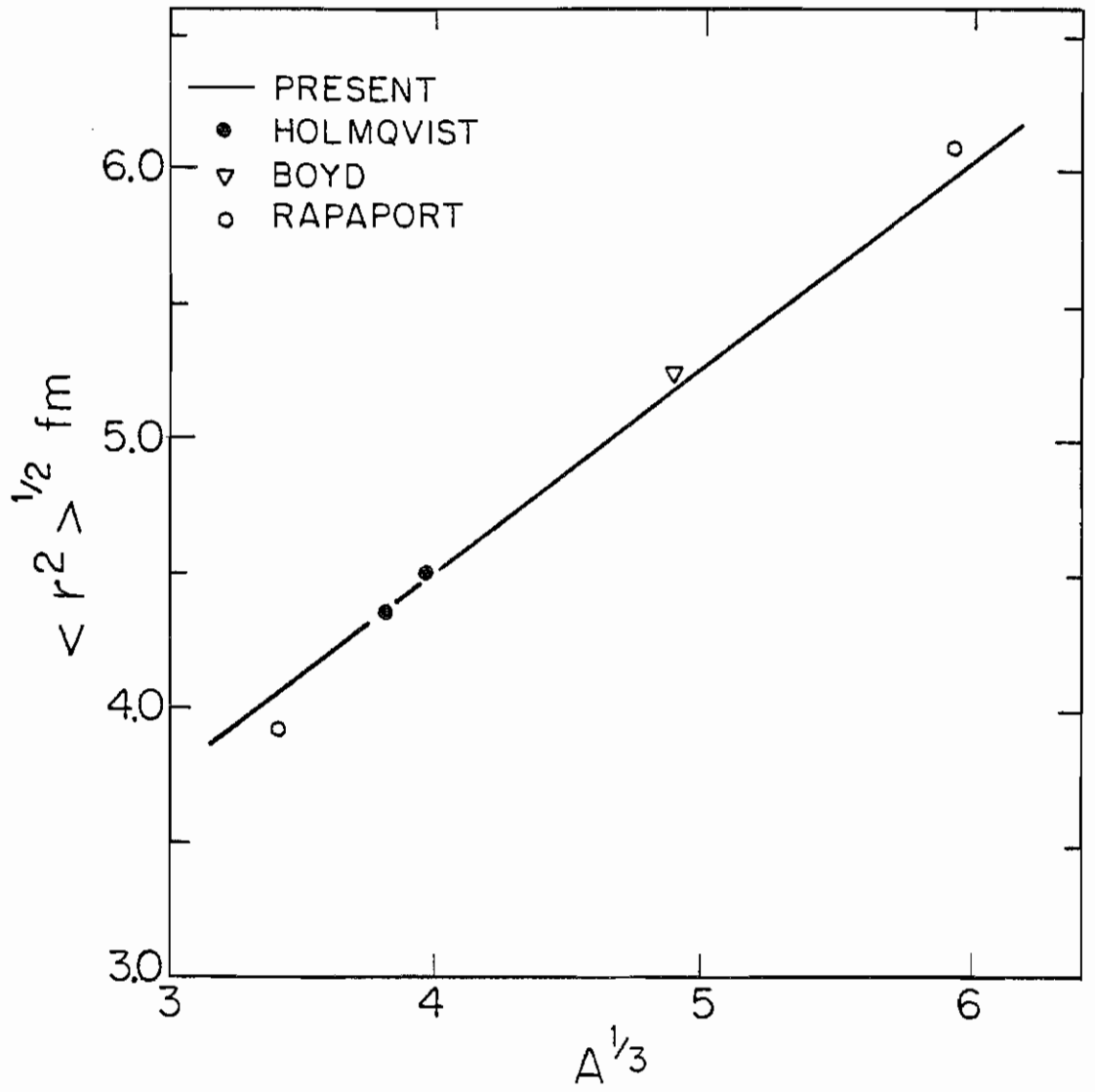

Figure 60 Comparison of rms radii of the real central potential of the present work to some of the corresponding values available.

$$\langle r^2_m \rangle = \langle r^2_R \rangle - \langle r^2 \rangle_{eff}$$

where $\langle r^2 \rangle_{eff}$ is the effective ms radius of the effective folding force. The obtained values of $\langle r^2 \rangle_{eff}$ depend on the choice made for the density dependent (DD) effective interactions and exchange terms (Negele 1970). The m.s.r $\langle r^2 \rangle_{eff}$ were estimated for Fe and Cu isotopes of the present work from the folding calculations involving the so-called (WDDE), (SDDE) and (N) for ^{16}O, ^{40}Ca, ^{58}Ni, ^{90}Zr and ^{208}Pb given by (Thomas et al. 1973). The values of the matter r.m.s radii $\langle r^2_m \rangle^{1/2}$ are compared in figure 61 with the plot of $\langle r^2_m \rangle^{1/2}$ as a function of $A^{1/3}$ given by Brissaud (Brissaud 1973) obtained from the analysis of the angular distributions for 166 MeV α-particle elastic scattering. This comparison has been suggested by (Delaroche 1980).

The neutron r.m.s. radii $\langle r^2_n \rangle^{1/2}$ are estimated from the general expression

$$A\langle r^2_m \rangle = Z\langle r^2_p \rangle + N\langle r^2_n \rangle$$

where Z is the proton number, $\langle r^2_p \rangle$ is the proton m.s.r. and N is the neutron number. The values of $\langle r^2_p \rangle$ are obtained from the m.s. charge radii $\langle r^2_c \rangle$ by removing the proton charge smearing (Borkowski et al. 1975). The neutron r.m.s.

radius for ^{56}Fe obtained in the present work is in very good agreement with 3.70 ± 0.11 obtained by Brissaud et al.

Table 14 shows the values of $\langle r^2_R \rangle^{1/2}$, $\langle r^2 \rangle_{eff}$, $\langle r^2_m \rangle^{1/2}$, $\langle r^2_c \rangle^{1/2}$, $\langle r^2_p \rangle^{1/2}$ and $\langle r^2_n \rangle^{1/2}$. The values of $\langle r^2_c \rangle^{1/2}$ have been obtained from de Jager (de Jager et al 1974).

TABLE 14

The r.m.s radii for iron and copper istopes of the present work

	$\langle r^2_R \rangle^{1/2}$	$\langle r^2 \rangle_{eff}$	$\langle r^2_m \rangle^{1/2}$	$\langle r^2_c \rangle^{1/2}$	$\langle r^2_p \rangle^{1/2}$	$\langle r^2_n \rangle^{1/2}$
^{54}Fe	4.324	5.0 ± 1.0	3.70	3.723	3.62	3.77
^{56}Fe	4.360	5.0 ± 1.0	3.74	3.787	3.69	3.78
^{63}Cu	4.470	5.2 ± 1.0	3.84	3.925	3.83	3.85
^{65}Cu	4.500	5.2 ± 1.0	3.88	3.947	3.85	3.90

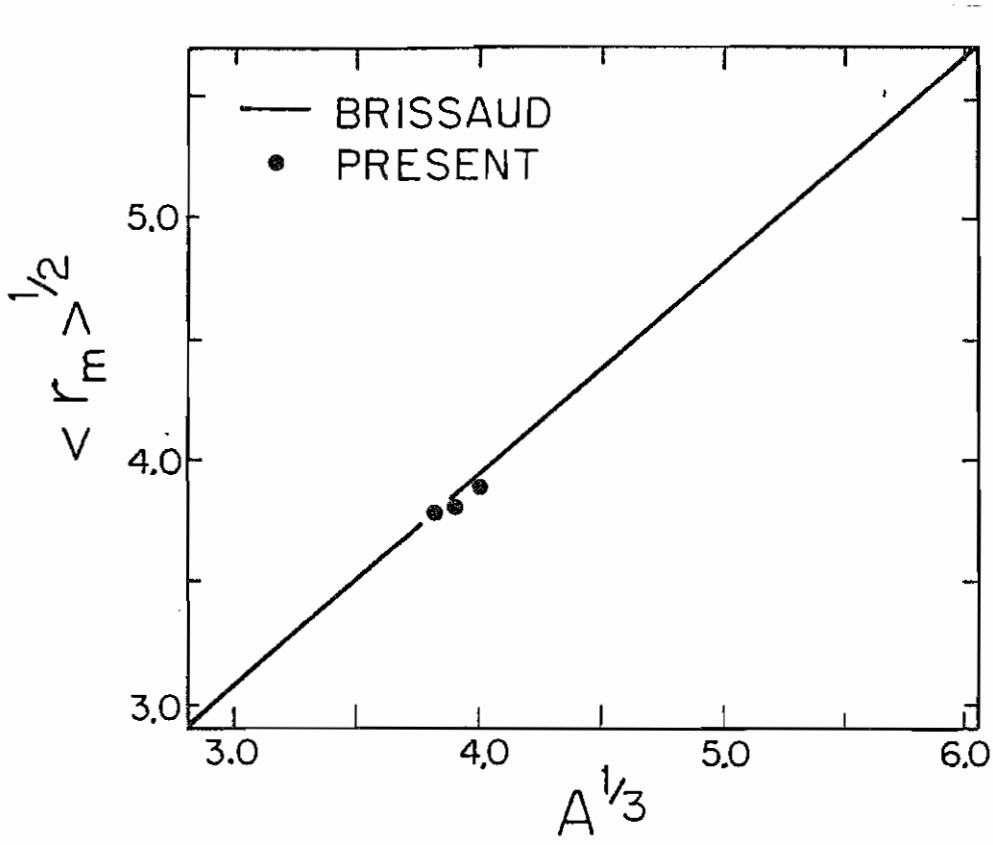

Figure 61 Comparison of r.m.s matter radii of the present work with the values obtained by Brissaud (see text).

Chapter V

COUPLED CHANNELS ANALYSES

In the coupled channels (CC) formalism, the total Hamiltonian of the interacting system can be written as

$$H = T + H_t + U$$

where T is the kinetic energy of the incident particle, H_t is the Hamiltonian for the internal collective motion of target nucleus and U is the deformed optical model potential which can be expressed for neutrons as:

$$U = -(V + iW_v)\, f(r,a_v,R_v) - 4iW_D d(f(r,a_D,R_D))/dr$$

$$+ 2\left(\frac{\hbar}{\pi}\right)^2 V_{so}\, L.S\, (1/r)\, d(f(r,a_{so},R_{so}))/dr \quad ,$$

where $f(r,a_i,R_i)$ is a Woods-Saxon form factor.

For harmonic vibrational nuclei R_i may be expressed as:

$$R_i = r_i A^{1/3}(1 + \alpha_{20} Y_2^0(\theta)) \quad \{i=V,D,so\},$$

where α_{20} is a linear operator which is related to the deformation parameter β_2 (Tamura 1965).

The optical potential given above can be expanded into spherical harmonics . This expression is given by Tamura and can be written in the centre-of-mass system in a general form as follows:

$$U = \sum_{\lambda} v_{\lambda}(r)(Q_{\lambda}.Y_{\lambda}) \qquad (5-1)$$

$Y_{\lambda}r)$ is a transition form factor when $\lambda \neq 0$, and Q_{λ} is an operator which allows transitions among states of the target nucleus. In the present work only $\lambda=2$ transitions are considered, since the calculations involve only 0^+ and 2^+ states for even-even nuclei. The first term ($\lambda=0$) in the above expression is just the usual spherical optical potential. The expression for the potential in eq. (5-1) is used to solve the eigenvalue equation:

$$(H - E)\ \psi = 0$$

Assuming that ψ can be separated into radial and angular components, then the radial coupled equations can be written as follows (Tamura 1965):

$$[-\hbar^2/(2m)\ d^2/dr^2 - l(l+1)/r^2 + E - E_I + V_{\lambda=0}]R^{J\pi}_c(r)$$

$$= \sum_{c',\lambda=2} V_{\lambda=2}(r) A(l,j,I,l',j',I',\lambda J) \langle I||Q_\lambda=2.||I'\rangle R^{J\pi}_{c'}(r)$$

In these coupled equations, A is a geometrical factor (Tamura 1965), $\langle I||Q_\lambda=2||I'\rangle$ is a nuclear reduced matrix element, and E_I is an eigenvalue of the target Hamiltonian.

In the harmonic vibrational model $\langle 0^+||Q_\lambda=2||2^+\rangle$ is just the quadrupole deformation β_2. In this picture the diagonal reduced matrix element $\langle 2^+||Q_\lambda=2||2^+\rangle$ is zero, while for the anharmonic vibrational model this diagonal matrix element (reorientation matrix element) differs from zero.

The analyses reported in this chapter deal with the inelastic scattering to low-lying excited states in Fe and Cu. The energy level diagrams for the lowest states for the isotopes of interest are plotted approximately to scale in figure 62.

5.1 ANALYSES OF DATA FOR IRON ISOTOPES

The CC analyses in the present work have been carried out using the computer code ECIS79 developed by J. Raynal (Raynal 1980). This code has the ability to find the best fit to elastic and inelastic scattering cross sections simultane-

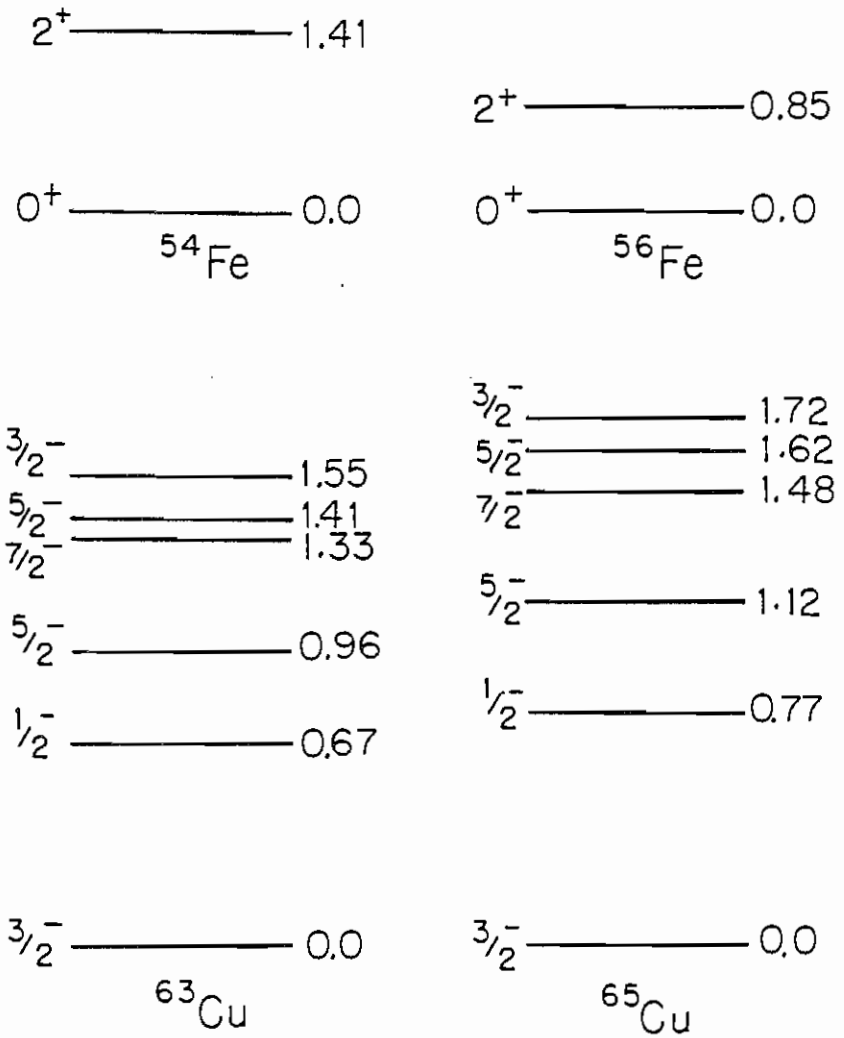

Figure 62 Energy level diagrams for the lowest states for Fe and Cu isotopes of the present work.

ously while the operator may prescribe constraints on the parameter space searched. In the present analyses we used a $(0^+,2^+)$ coupling scheme. The starting optical potential parameters for the CC calculations were taken from the global spherical optical potential deduced in the previous chapter. The search concentrated on the data between 10 and 14 MeV since at these energies the compound nucleus contributions to the cross sections are believed to be nearly negligible. The fitting was performed by assuming several values of β_2 ranging from 0.2 to 0.25 . The volume imaginary potential was set to zero since, in the course of the present work, it was found that its effect on the quality of the fits was very small .

In the first stage of these analyses, the following ambiguities were avoided:

$$V.r^n = \text{constant},$$

$$W_D.a_D = \text{constant},$$

$$W_D.\beta = \text{constant}.$$

As a result of the search on the potential geometry, it was found that slight modifications to the values given previously in table 12 were desirable. The geometry was then kept

fixed throughout the CC calculations and the search for V and W_D was carried out for each individual data set of the present work.

The values of V and W_D which gave the best fit are plotted vs. energy in figures 63 - 64. From the sensitivity of the search it has been found that the uncertainties attached to V and W_D are typically ~1% and ~10%, respectively. At 8 MeV incident energy, the estimated uncertainty on W_D is larger (~15%) since the compound nucleus component cannot be neglected. As can be seen, the energy variation of V can be well represented by a straight line.

Since the uncertainty on each individual value of W_D was high, it is more difficult to select a precise energy dependent representation of this potential. However it seems that W_D increases with increasing incident energy in the present work. It is possible therefore to represent W_D by either

$$W_D(E) = \alpha + \gamma E^{1/2} \qquad (5\text{-}2a)$$

or $$W_D(E) = \alpha' + \gamma' E \qquad (5\text{-}2b)$$

where α, α', γ, γ' are adjustable constants and E is the incident neutron energy.

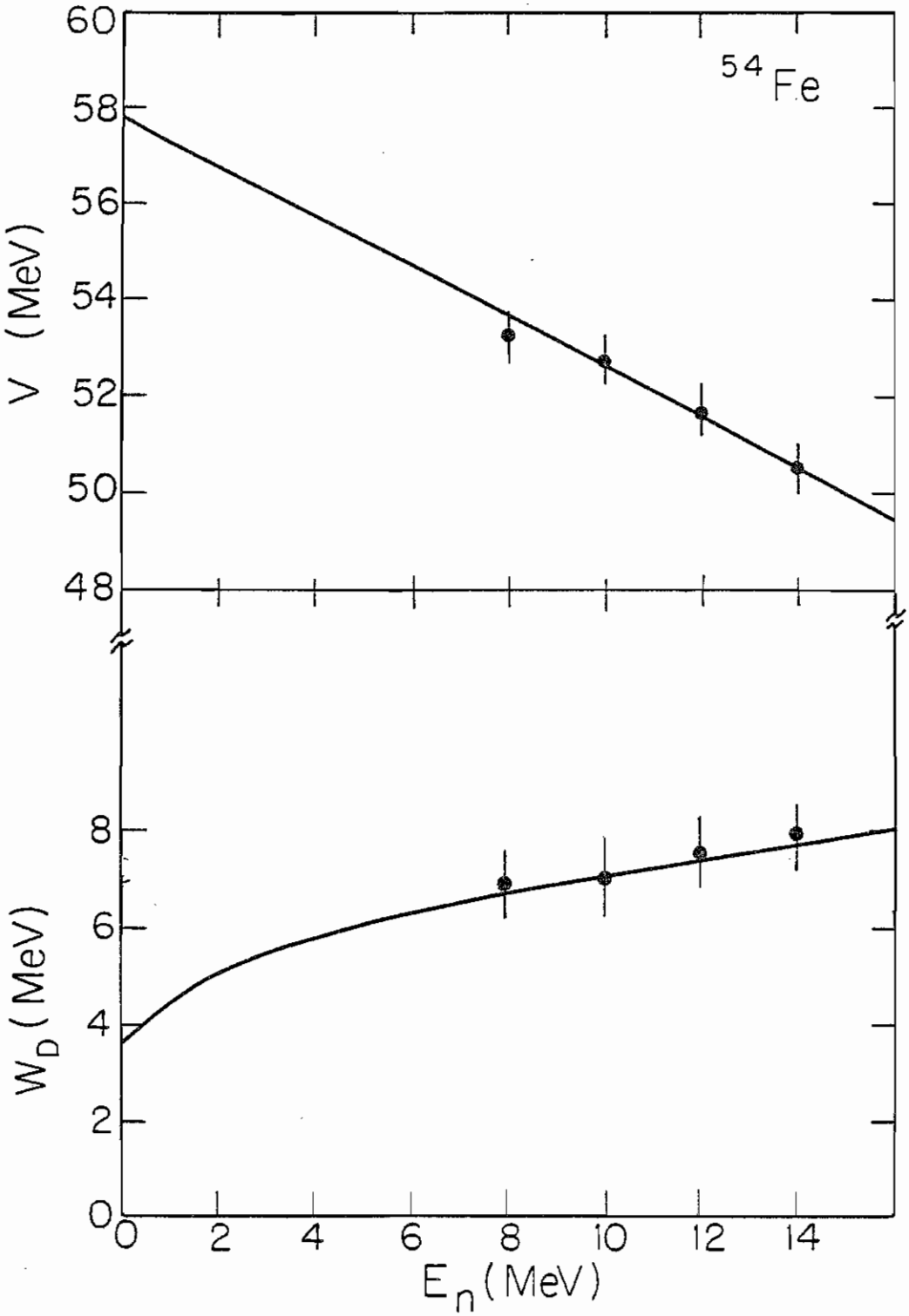

Figure 63 Energy variation of the real and imaginary potentials for ^{54}Fe from CC calculations.

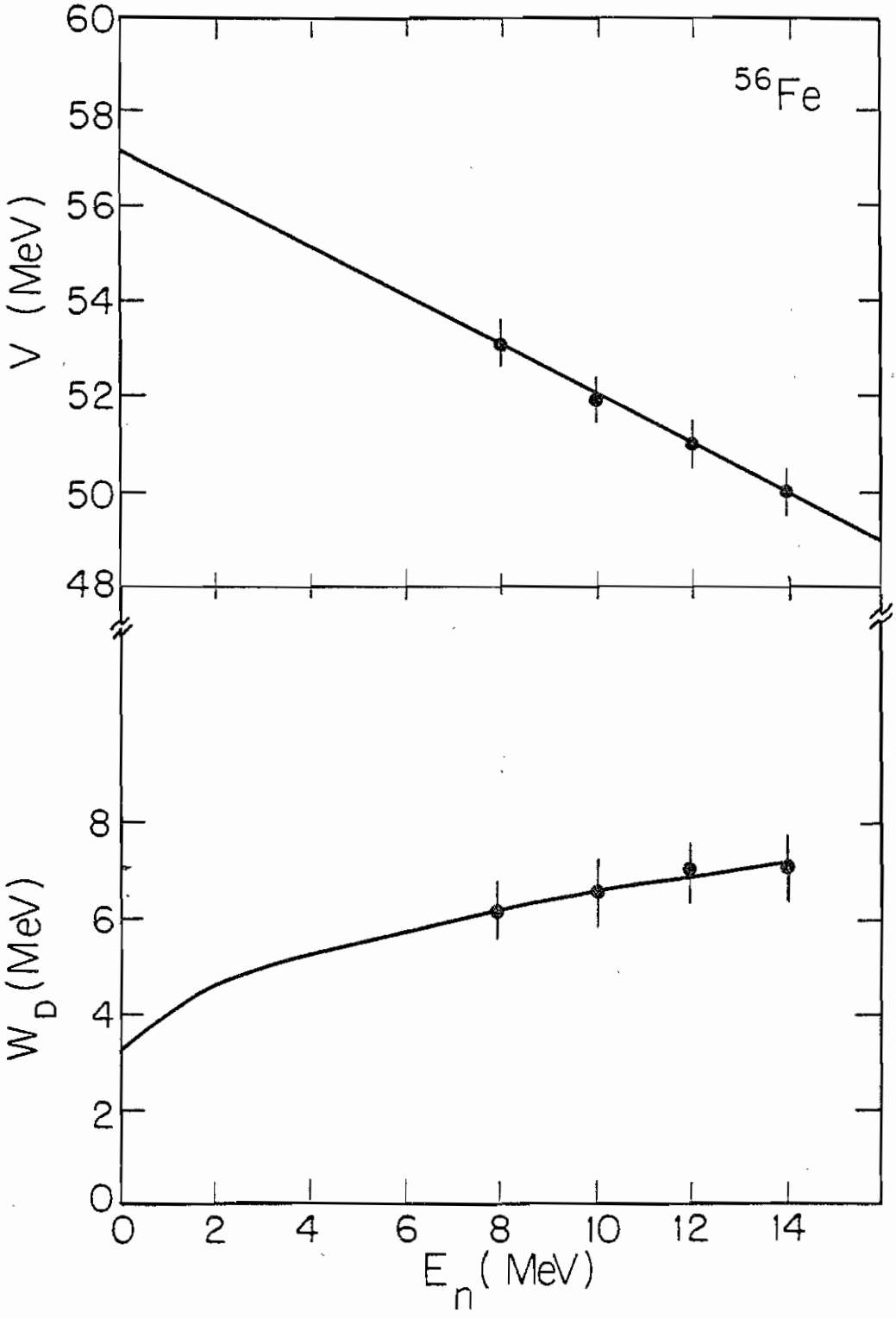

Figure 64 Energy variation of the real and imaginary potentials for ^{56}Fe from CC calculations.

Coupled channels calculations of total cross sections for ^{56}Fe using both parametrizations for $W_D(E)$ were performed for energies between 10 keV and 8 MeV. The agreement achieved between the experimental and the calculated total cross sections seems to be slightly better when the expression (5-2a) is used. The result of the CC calculations of total cross sections for ^{56}Fe obtained by using equation (5-2a) are compared to the total cross sections obtained from (BNL325 1976) in figure 65. In addition, the potential scattering radius (R') and the S-wave strength function (S_0) calculated at 100 keV have been compared with available data (BNL325 1973). The result of this comparison is given later in table 16

The specific aim of perfoming this part of the study was to check predictions from our model to those of others who used different methods to obtain the neutron data for strength function, potential scattering radius and the total cross section. At low incident energies, the prediction of such data are known to be sensitive to small variations of the potential as well as the deformation parameters. This complimentary analysis is just the reverse order of the technique for fitting data that is involved in the SPRT method (Delaroche et al. 1976). In this method the search procedures start by fitting the strength functions (S_0, S_1), potential scattering radius (R') and the energy variation of the total cross section (σ_T). In the SPRT method, by slight adjustment to the optimized optical potential and

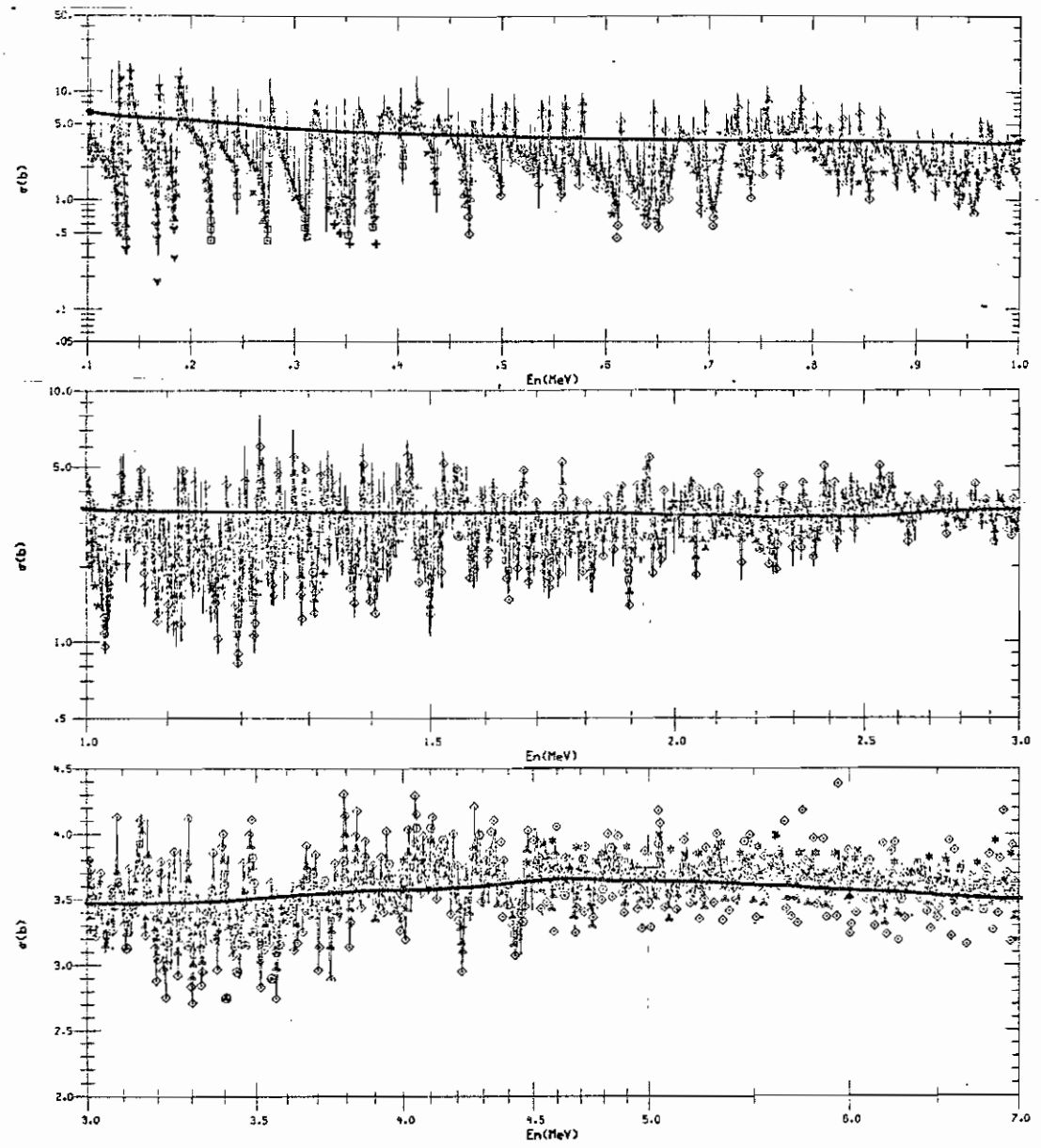

Figure 65 Comparison between the prediction of total cross section from present work for ^{56}Fe and the total cross section of natural Fe (see text).

deformation parameters, good fits for the differential elastic and inelastic scattering cross section can usually be obtained.

The optical potential parameters obtained for ^{54}Fe and ^{56}Fe are given in table 15. Coupled channels predictions using these parameters as well as the data of the present work for ^{54}Fe and ^{56}Fe are given in figures 66-69. The difference in the central potentials between the two Fe isotopes divided by the difference in their symmetry (N-Z)/A gives V_1, the real part of the Lane potential, and the corresponding ratio for the imaginary surface potential gives W_{D1}, the imaginary part of this potential. These terms are: $V_1 = 20 \pm 3$ MeV and $W_{D1} = 14 \pm 4$ MeV. The general expression then for the optical potential for ^{54}Fe and ^{56}Fe can be written from this analysis as:

$$V = 58.53 - 0.52E - 20(N-Z)/A$$

$$W_D = 4.1 + 1.1E^{1/2} - 14(N-Z)/A$$

The potential deformation parameters for ^{54}Fe and ^{56}Fe were determined with an estimated uncertainty of ~5%. The deformation lengths $\beta_2.r$ (r is the real central potential radius) obtained in present work were compared with corresponding Coulomb deformation lengths $\beta_c.r_c$ obtained from Cou-

TABLE 15

CC Optical Potential Parameters For ^{54}Fe and ^{56}Fe

	^{54}Fe	^{56}Fe
V	$57.8 - 0.52E$	$57.1 - 0.52E$
W_D	$3.6 + 1.1E^{1/2}$	$3.1 + 1.1E^{1/2}$
β_2	0.20	0.24

$r = 1.165$, $a = 0.656$, $r_D = 1.261$, $a_D = 0.593$

$V_{so} = 6.108$, $r_{so} = 1.017$, $a_{so} = 0.600$

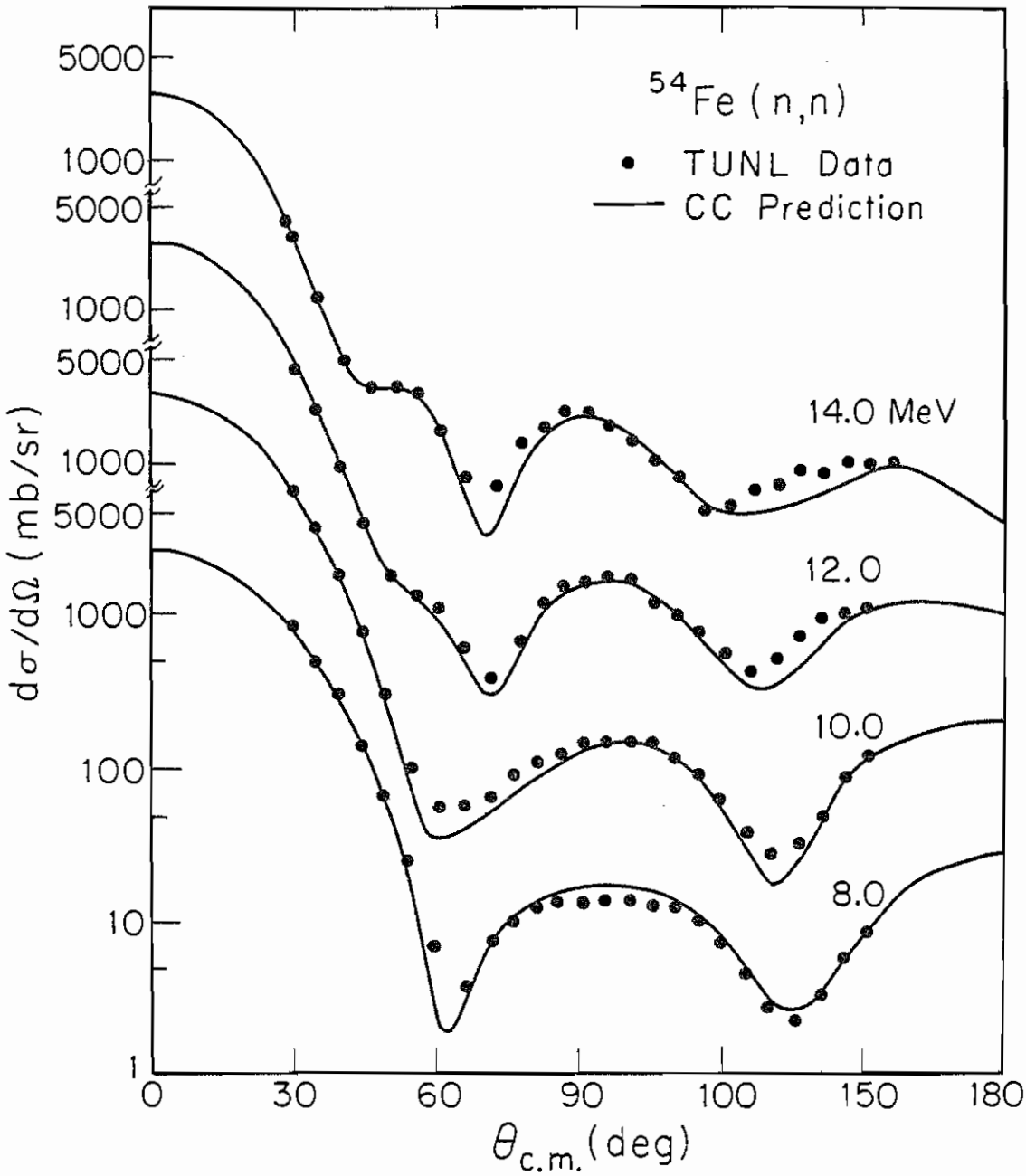

Figure 66 Coupled channels fit to the elastic scattering cross sections of ^{54}Fe.

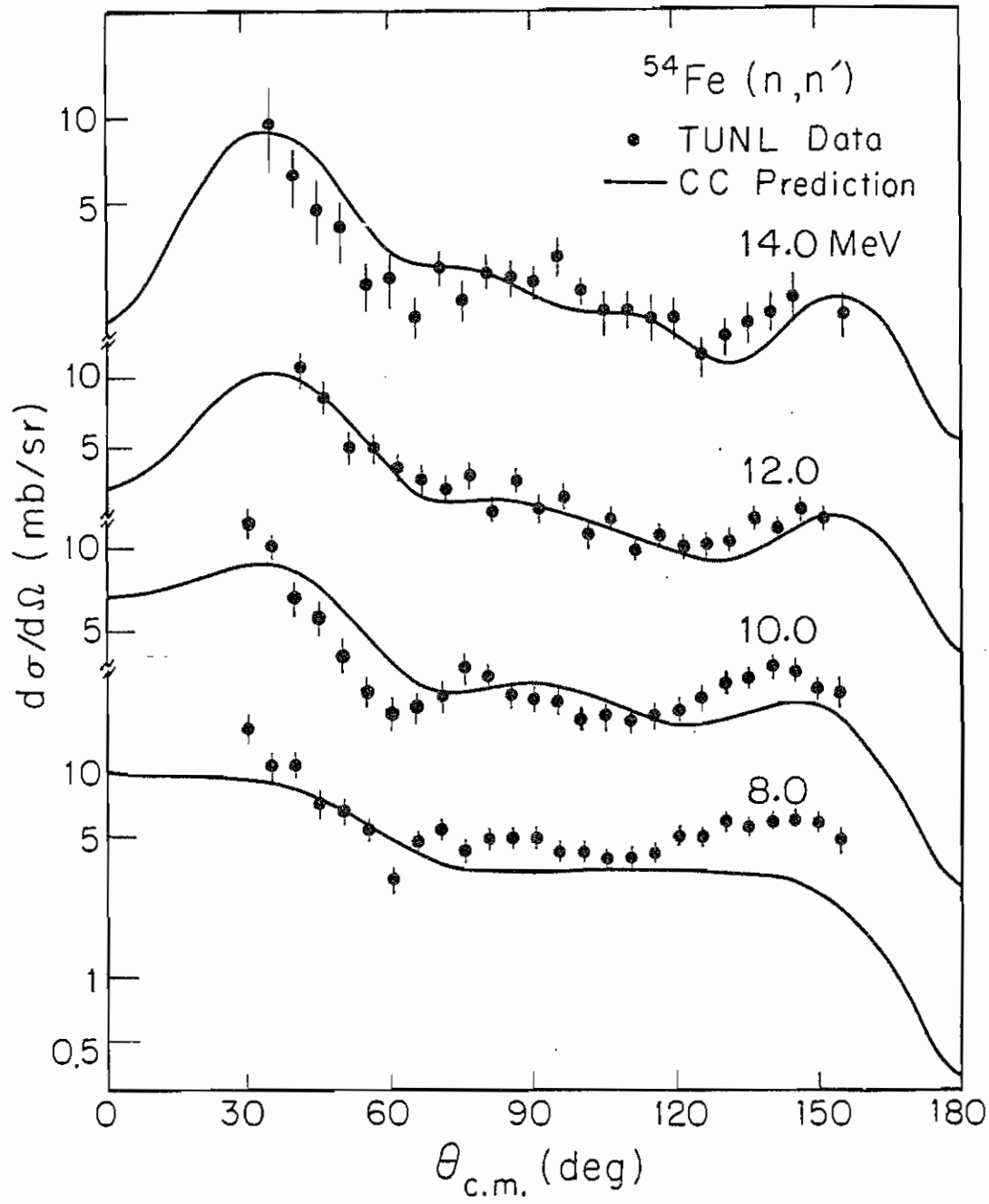

Figure 67 Coupled channels fit to the inelastic scattering cross sections of ^{54}Fe.

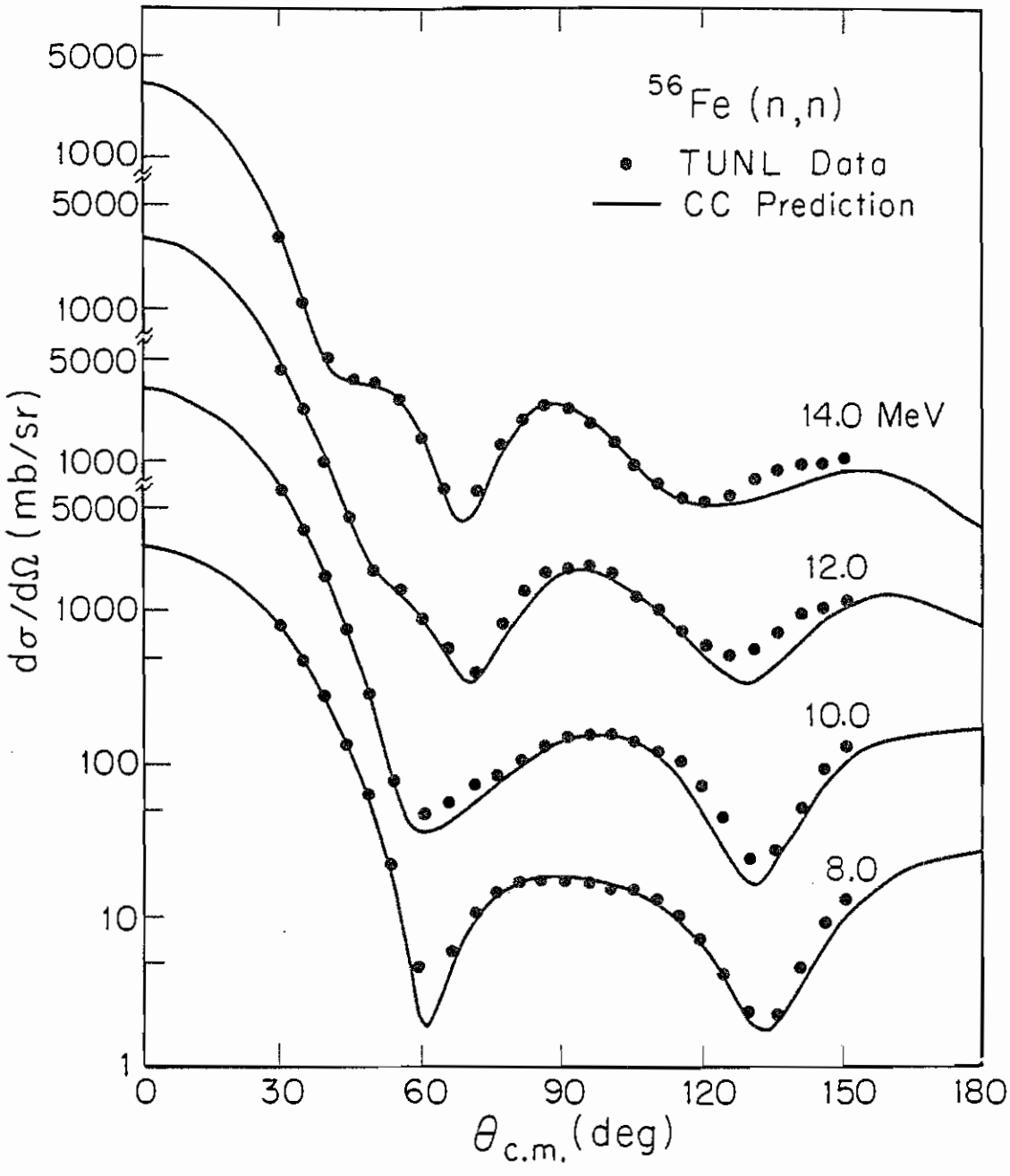

Figure 68 Coupled channels fit to the elastic scattering cross sections of ^{56}Fe.

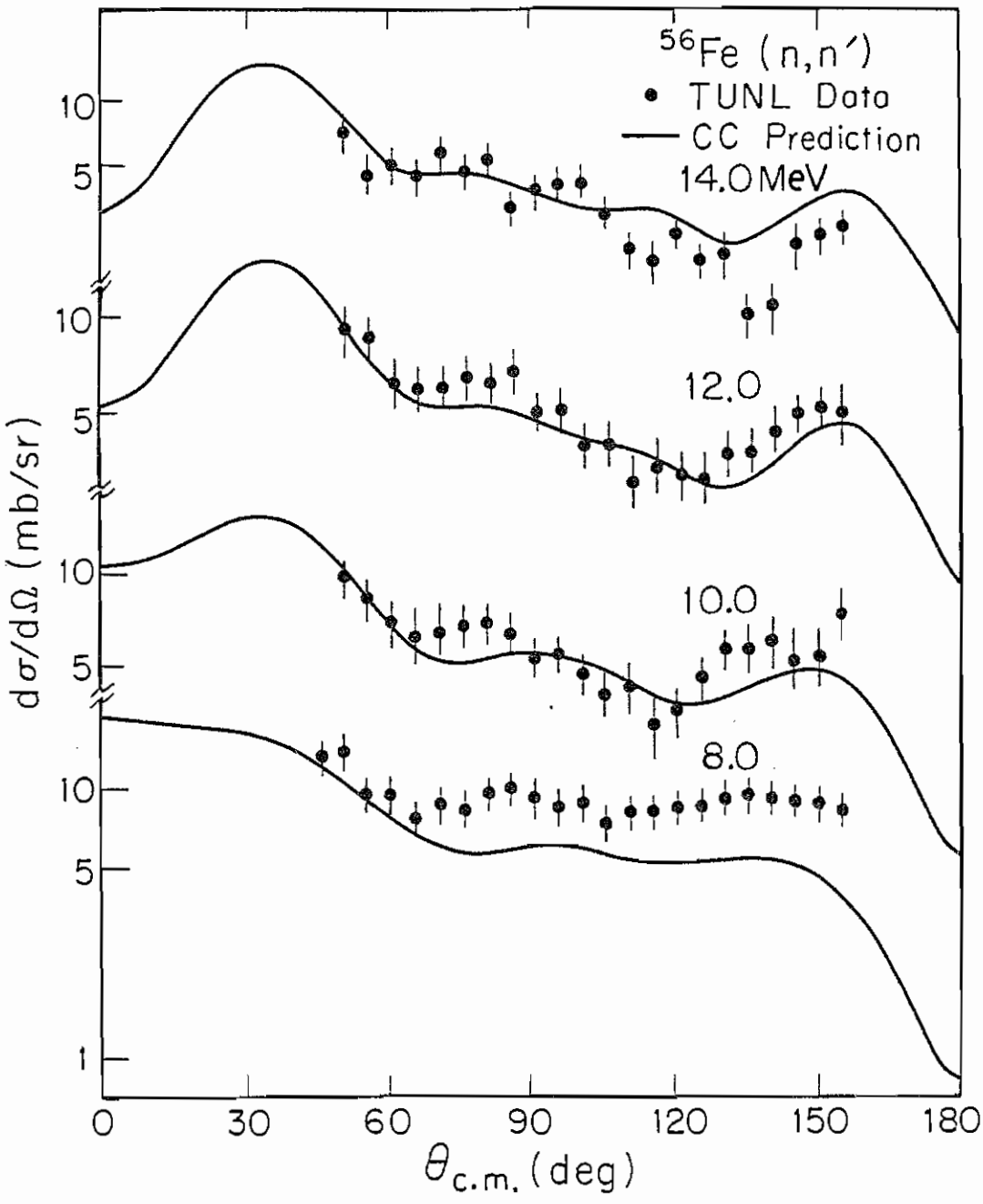

Figure 69 Coupled channels fit to the inelastic scattering cross sections of ^{56}Fe.

lomb excitation (CE) measurements (LeVine 1981). The results of this comparison are given in table 16. The agreement is very satisfactory except for the value of S_0 for ^{54}Fe which is about half the value obtained from the standard reference (BNL325). However, we believe that the experimental values of S_0 given in BNL325 for ^{54}Fe are too high, and possibly unreliable since large nonstatistical effects have been already obtained in the neutron interaction with this nucleus in the resonance region (Allen et al. 1977).

TABLE 16

Comparison of R', S_0, and $\beta.r$ with available data

	Present $\beta.r$	CE $\beta_c.r_c$	Present R'	BNL R'	Present S_0	BNL S_0
^{54}Fe	0.233	0.245	6.37	5.6±0.6	2.3	5.6±1.7
^{56}Fe	0.280	0.292	5.36	6.1±0.7	2.07	1.6±0.5

5.1. Anharmonicity effects on the predicted cross section of ^{56}Fe

In the previous calculation for both Fe isotopes, the harmonic vibrational model was assumed. This assumption seems to be good for ^{54}Fe since recent Coulomb excitation measurements (Levine 1981) have shown that the quadrupole moment $Q(2^+)$ is consistent with a value of zero. In contrast, the same measurements for ^{56}Fe have shown a consider-

able value of $Q(2^+)$. This difference between the nature of ^{54}Fe and ^{56}Fe is attributed to the fact that the experimental results for ^{56}Fe indicates that this nucleus can be considered as an anharmonic vibrator. Thus a reorientation matrix element $\langle 2^+||Q_{\lambda=2}||2^+\rangle$ deduced from this experimental quadrupole moment has been inserted in the CC calculations for this isotope. The model independent relationship between $Q(I^\pi)$ and $\langle I^\pi||Q_{\lambda=2}||I^\pi\rangle$ can be expressed (Kumar 1975) as:

$$Q(I) = (16\pi/5)^{1/2}[I(2I-1)/(I+1)(2I+1)(2I+3)]^{1/2}\langle I||Q_{\lambda=2}||I\rangle$$

Then, for a 2^+ state we get:

$$Q(2^+) = 0.758\langle 2^+||Q_{\lambda=2}||2^+\rangle$$

Figure 70 shows a comparison between the experimental data and the CC calculation at 14 MeV. The shadowed area in this figure shows the sensitivity of the CC calculations to the uncertainty in the measured value of $Q(2^+)$. The solid line is the CC calculation with $Q(2^+)=0$. As can be seen, the reorientation effect is important in predicting the 2^+ cross section at this incident energy. At lower incident energies the effect is less pronounced.

In contrast to the sensitivity shown in figure 70, the effect of the spin-orbit deformation on the predicted scattering angular distributions at 14 MeV is hardly noticeable. With the availability of polarization data from measurements in progress at TUNL, the effects of this parameter will be investigated more accurately.

5.2 ANALYSES OF DATA FOR CU ISOTOPES

The analyses of ^{63}Cu and ^{65}Cu scattering measurements are more difficult than those of Fe isotopes, since the inelastic scattering cross sections were only obtained for several unresolved states. In order to analyze such data we assume the simplest version of the weak particle-core coupling model (De Shalit 1961) in CC calculations. In this picture, the predicted inelastic scattering cross section to any of the quadruplet states (J) can be written as follows (Hodgson 1974):

$$\frac{d\sigma}{d\Omega}(J_p \longrightarrow J) = \frac{(2J+1)}{(2J_c+1)(2J_p+1)} \cdot \frac{d\sigma}{d\Omega}(J_0 \longrightarrow J_c)$$

where J_p is the angular momentum of the ground state and J_c is the angular momentum of the excited state of the even core. In the present case J_c is the angular momentum of the first excited state [$J_c^{\pi} = 2^+$], and $d\sigma/d\Omega$ (J_0--->J_c) is the direct inelastic scattering cross section to the first-ex-

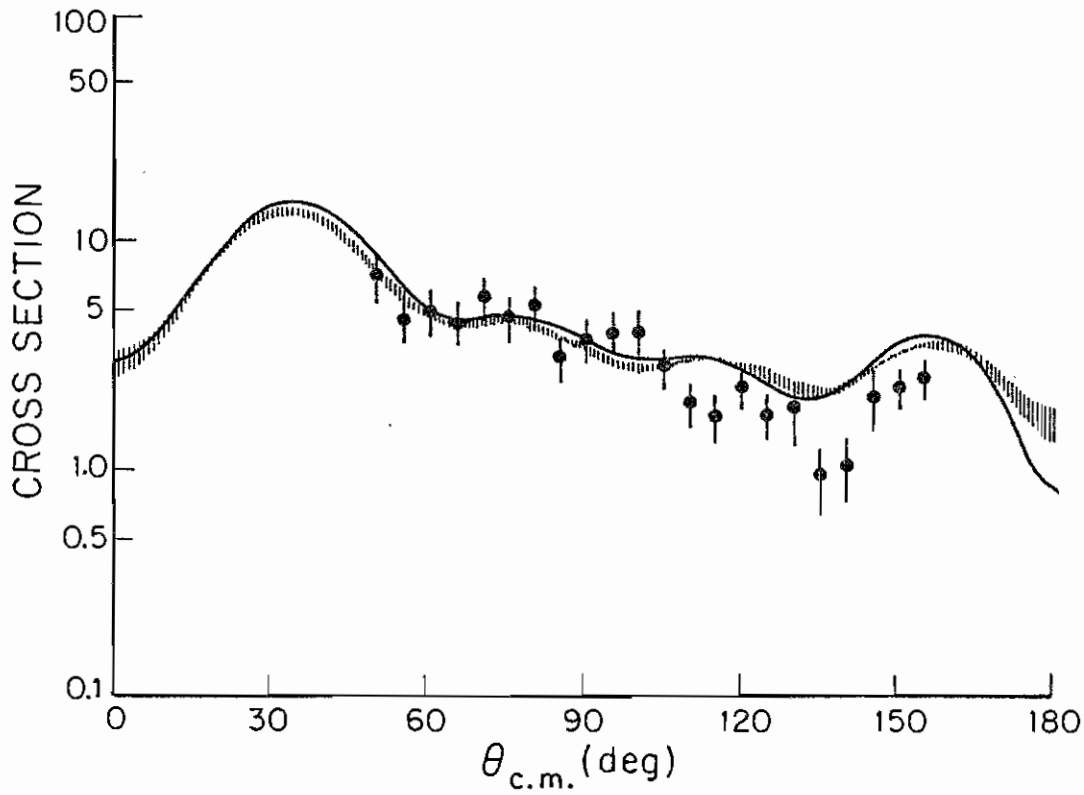

Figure 70 Anharmonicity effect on the prediction of the 2^+ cross section of ^{56}Fe.

cited state in the core, which in the present case is represented by $d\sigma/d\Omega$ $(0^+ \longrightarrow 2^+)$.

In the present work, the measured inelastic scattering cross sections at 8 and 10 MeV are most likely due to the excited states at 0.67 MeV $(1^-/2)$, 0.962 MeV $(3^-/2)$ and 1.327 MeV $(7^-/2)$ for ^{63}Cu and are due to the excited states at 0.771 Mev $(1^-/2)$, 1.116 MeV $(5^-/2)$ and 1.482 MeV $(7^-/2)$ for ^{65}Cu (see figure 62). For 12 and 14 MeV the measured inelastic scattering cross sections are due to all of the excited states lying below 2.0 MeV. In this excitation energy range there is an additional excited state at 1.412 MeV $(5^-/2)$ for ^{63}Cu and at 1.623 MeV $(5^-/2)$ for ^{65}Cu. This state does not belong to the quadruplet and has been considered to be collective since it was found to be ~29% of $d\sigma(3^-/2 \longrightarrow 7^-/2)/d\Omega$ for ^{63}Cu while it was found to be only ~22% of $d\sigma(3^-/2 \longrightarrow 7^-/2)/d\Omega$ for ^{65}Cu from reported (p,p') measurements (McCarthy et al. 1966). In the first stage of the analyses described here, the contributions of these states to the measured inelastic scattering cross sections was ignored.

The analyses of the Cu data started at 14 MeV, since the measured cross sections should compare in first approximation directly to the $d\sigma/d\Omega(0^+ \longrightarrow 2^+)$ cross sections of the respective cores. The CC calculations were performed assuming a $(0^+ \longrightarrow 2^+)$ coupling basis, in which the 2^+ state is

the first excited state of the neighboring even core which were to be assumed as vibrational nuclei (^{62}Ni and ^{64}Ni). The energy of the 2^+ state of ^{62}Ni is within one percent of the center of gravity of ^{63}Cu quadruplets. The energy of the 2^+ state of ^{64}Ni is also within one percent of the center of gravity of ^{65}Cu quadruplets.

In the CC analyses for the Cu isotopes, the geometry of the optical potential was assumed to be identical to that used previously for Fe isotopes. Then searching on the data with ECIS79, the quadrupole deformation parameters (β_2) as well as V and W_D were determined at 14 MeV. At lower incident energies the parameter (β_2) was kept constant while the values of V and W_D were adjusted in order to produce the best fit to the elastic and inelastic scattering cross sections. The inelastic scattering cross sections at 8 and 10 MeV then were compared with only 80% of the predicted $d\sigma/d\Omega(0^+ \longrightarrow 2^+)$ because the measured cross section at these energies do not include the $3^-/2$ state. The contribution of the second ($5^-/2_2$) excited state was considered at higher incident energies. In these cases, the measured inelastic scattering cross sections were compared to 1.12 $d\sigma(0^+ \longrightarrow 2^+)/d\Omega$ for ^{63}Cu and 1.08 $d\sigma(0^+ \longrightarrow 2^+)/d\Omega$ for ^{65}Cu which account for the percentages mentioned above.

The searches for V and W_D were carried out for each individual data set between 8 and 14 MeV for both ^{63}Cu and ^{65}Cu

in the same manner as for ^{54}Fe and ^{56}Fe. The values of V and W_D which gave the best individual fits are plotted vs. energies in figures 71 - 72. As seen in the figures, the energy variation of both V and W_D can be assumed linear. The optical potential parameters obtained for ^{63}Cu and ^{65}Cu are given in table 17. The CC predictions using these parameters are compared to the data of the present work in figures 73 - 76. The discrepancies between the data and the fits are believed to be in part due to the difficulty of separating the elastic from the inelastic peaks of the measured time-of-flight spectra (see chapter 3).

The symmetry terms V_1 and W_{D1} were then deduced and their values are:

$$V_1 = 25 \pm 3 \text{ MeV}, \qquad W_{D1} = 14 \pm 5 \text{ Mev}$$

These values agree very well with those obtained above for iron. The optical potential V and W_D can be expressed for ^{63}Cu and ^{65}Cu as:

$$V = 59.48 - 0.46E - 25(N-Z)/A$$

$$W_D = 3.71 + 0.37E - 14(N-Z)/A$$

TABLE 17

CC Optical Potential Parameters For ^{63}Cu and ^{65}Cu

	^{63}Cu	^{65}Cu
V	57.5 - 0.46E	56.8 - 0.46E
W_D	2.6 + 0.37E	2.2 + 0.37E
β_2	0.23	0.21

$r = 1.165$, $a = 0.656$ $r_D = 1.261$, $a_D = 0.593$

$V_{so} = 6.108$ $r_{so} = 1.017$ $a_{so} = 0.600$

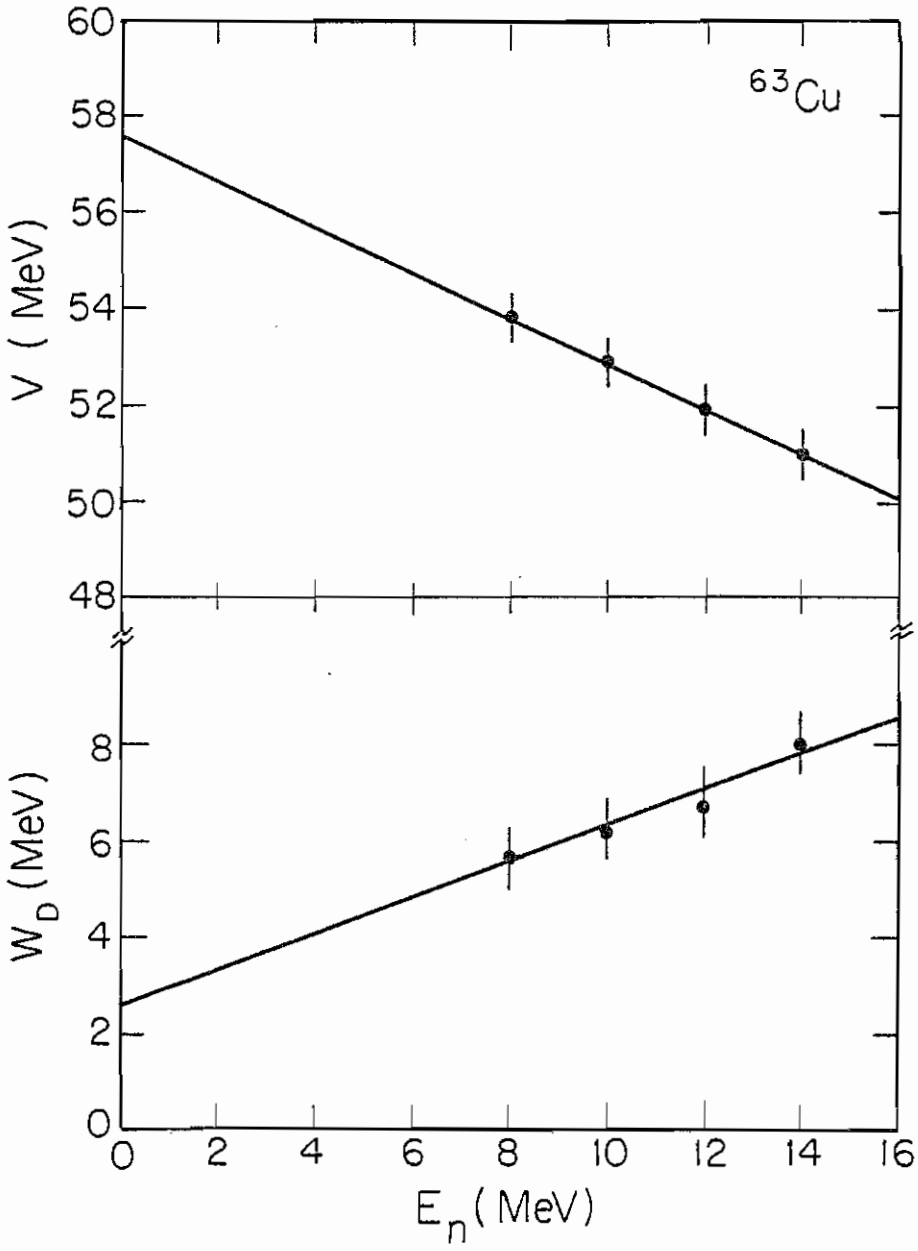

Figure 71 Energy variation of the real and imaginary potentials for ^{63}Cu from CC calculations.

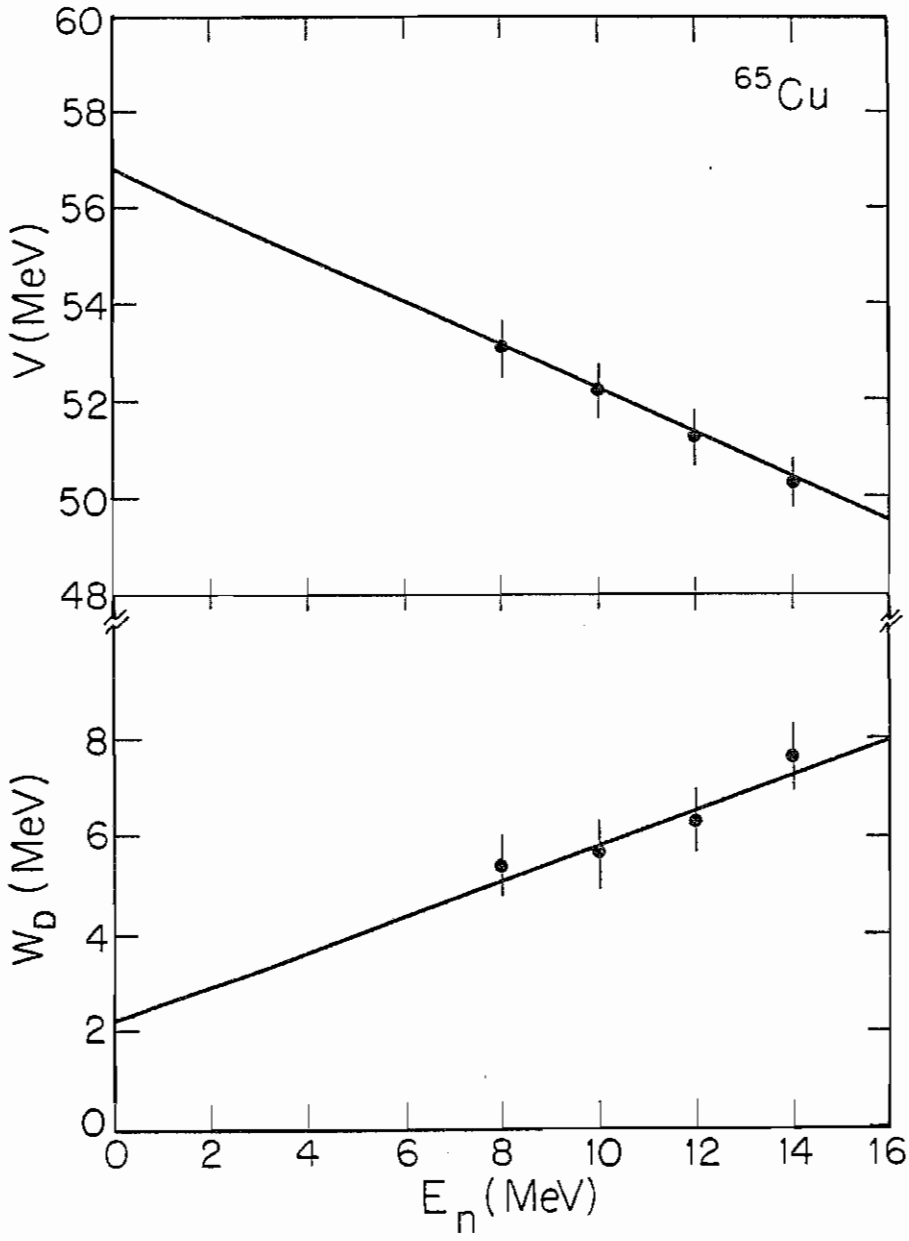

Figure 72 Energy variation of the real and imaginary potentials for ^{65}Cu from CC calculations.

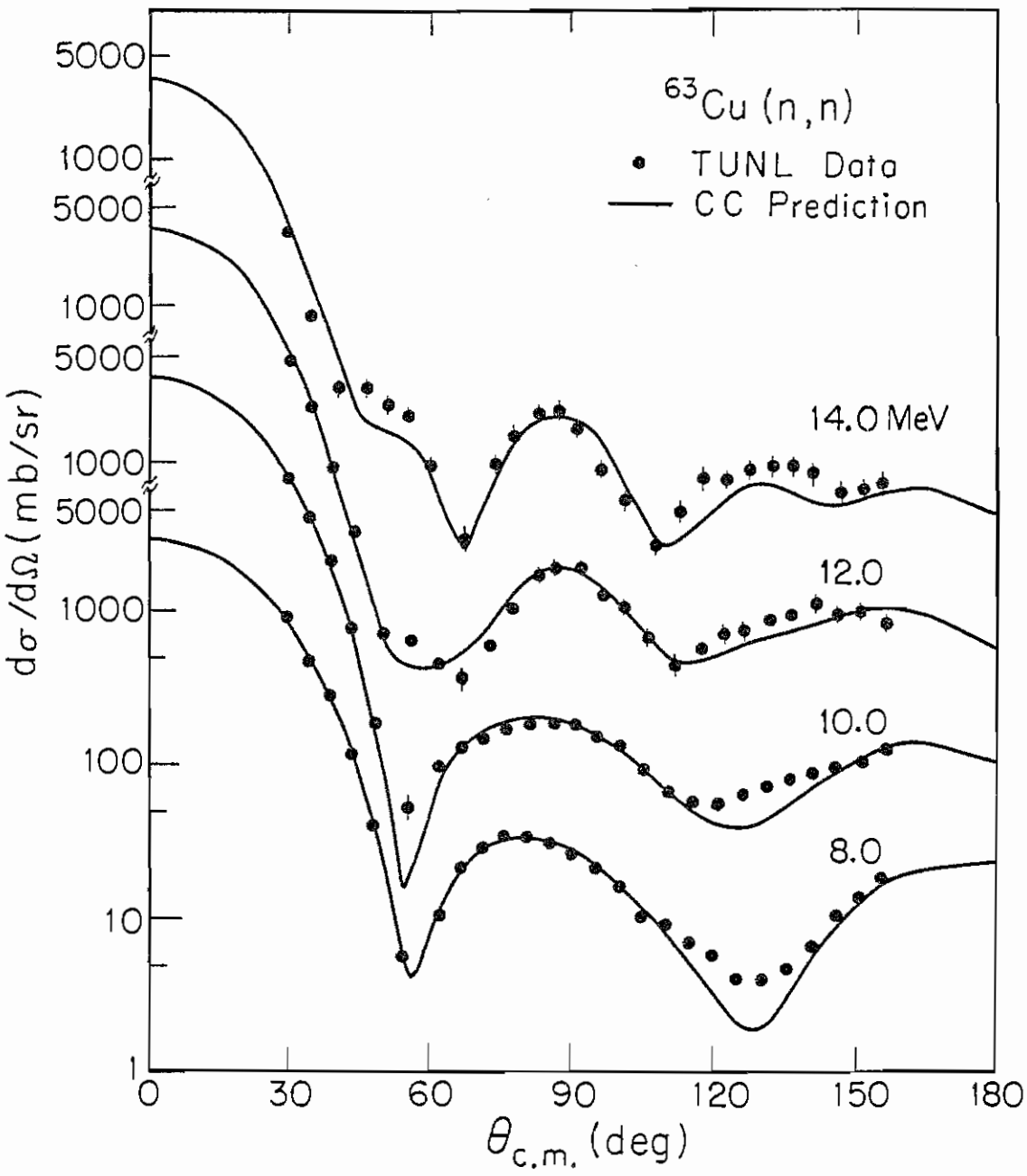

Figure 73 Coupled channels fit to the elastic scattering cross sections of ^{63}Cu.

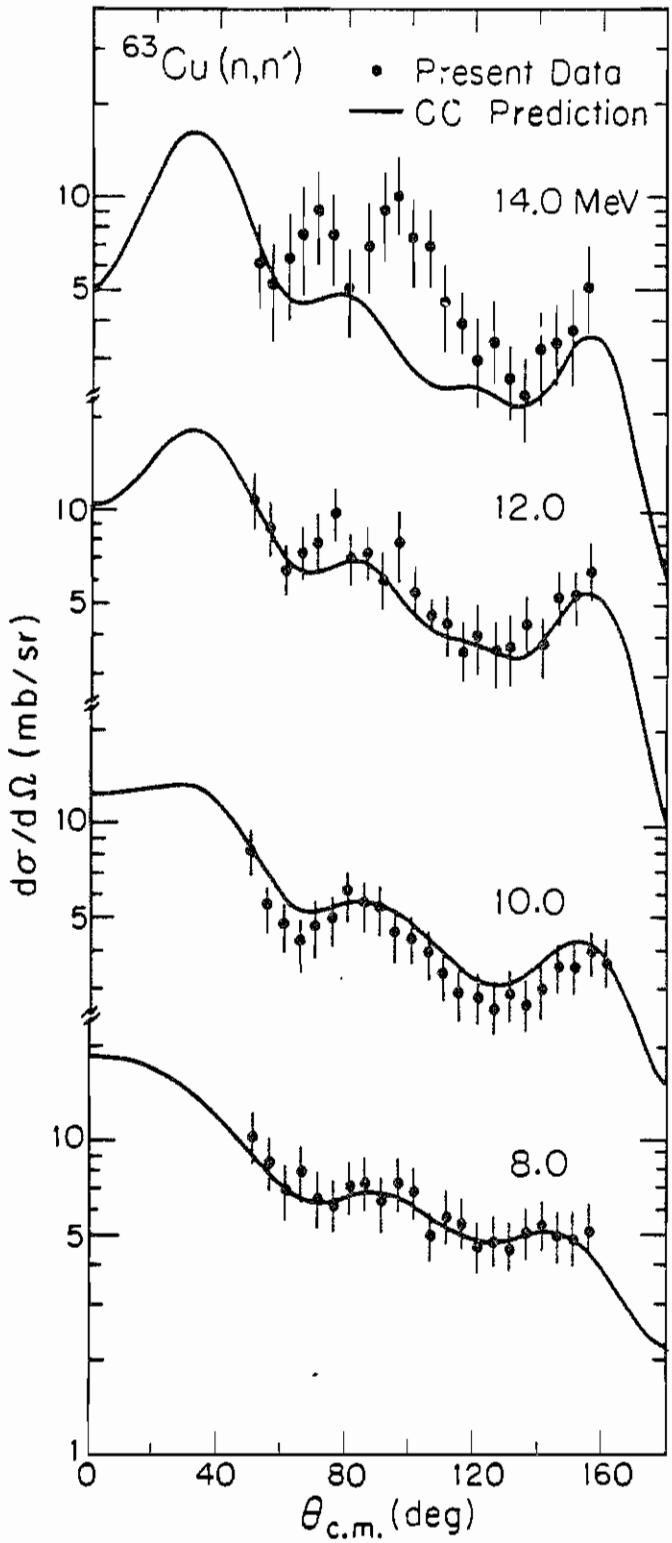

Figure 74 Coupled channels fit to the inelastic scattering cross sections of ^{63}Cu.

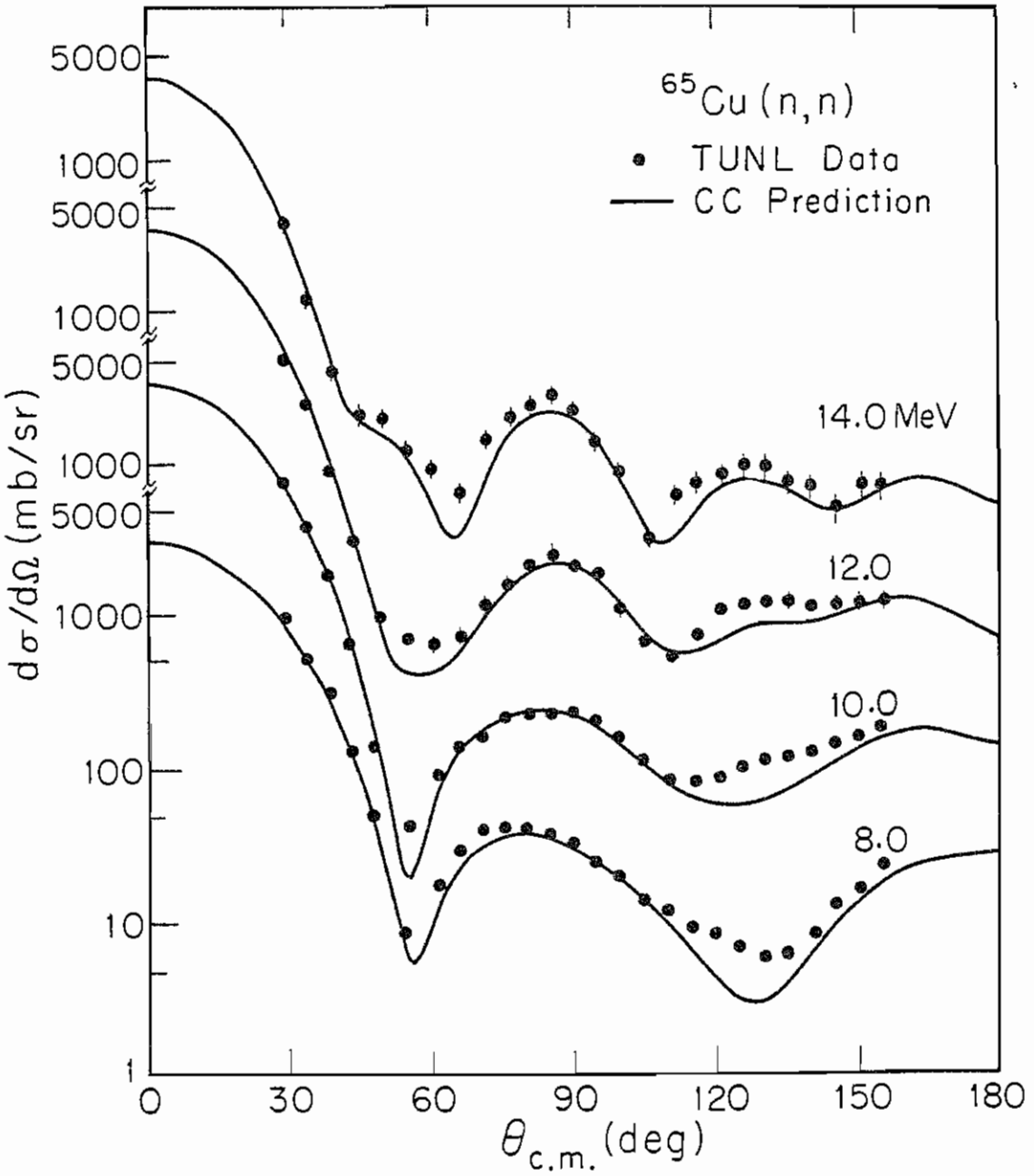

Figure 75 Coupled channels fit to the elastic scattering cross sections of ^{65}Cu.

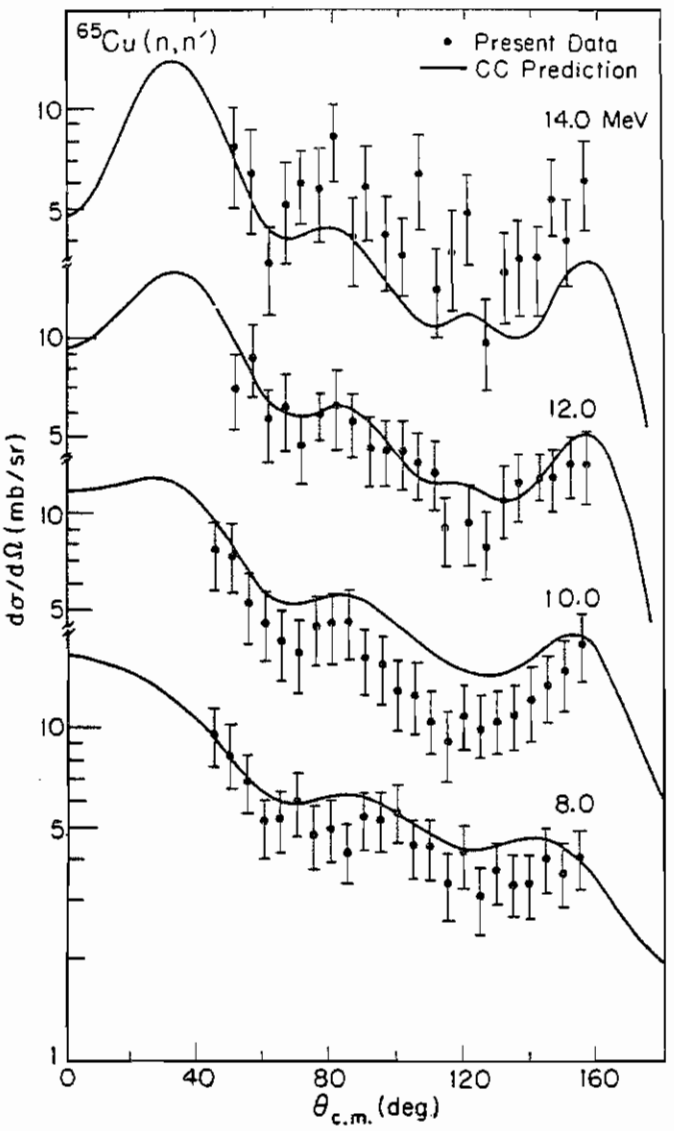

Figure 76 Coupled channels fit to the inelastic scattering cross sections of ^{65}Cu.

The expressions for V and W_D obtained in this section as well as in the preceeding one are based on data in the energy range between 8 and 14 MeV, and therefore are certainly valid in this energy region. To test the validity of the above energy variation of V and W_D as well as the geometry parameters, the total cross sections were calculated in the energy range between 0.01 and 14 MeV. Figure 77 shows the comparison between the present calculation and the total cross sections obtained from (BNL325 1976). As can be seen, the agreement is very good.

We took one further step and calculated the potential scattering radius (R') and the S-wave strength function (S_0) at 10 keV and compared them with the values given in (BNL325 1973). The results of this comparison are given in table 18 The value of R' obtained from BNL325 is for natural Cu. The table shows also the comparison of the present $\beta.r$ to $\beta_c.r_c$ obtained from coulomb excitation measurements for the neighboring Ni isotopes (Stelson et al. 1966).

As can be seen, even with simple approach and with the poor data above 10 MeV for the copper isotopes, the predicted elastic and inelastic cross sections fitted our data reasonably well. The values obtained for (R') and (S_0) are in good agreement with the available data. The value of $\beta.r$ for ^{65}Cu also agreed well with the corresponding value from Coulomb excitation measurments for ^{64}Ni. Even though the value of $\beta.r$ obtained for ^{63}Cu is slightly higher than the

TABLE 18

Comparison of R', S_0, and $\beta.r$ with available data

	Present $\beta.r$	CE $\beta_c.r_c$	Present R'	BNL R'	present S_0	BNL S_0
^{63}Cu	0.270	0.230	6.02	7.1±0.2	2.02	2.4±0.6
^{65}Cu	0.245	0.230	6.15	7.1±0.2	2.18	1.5±0.4

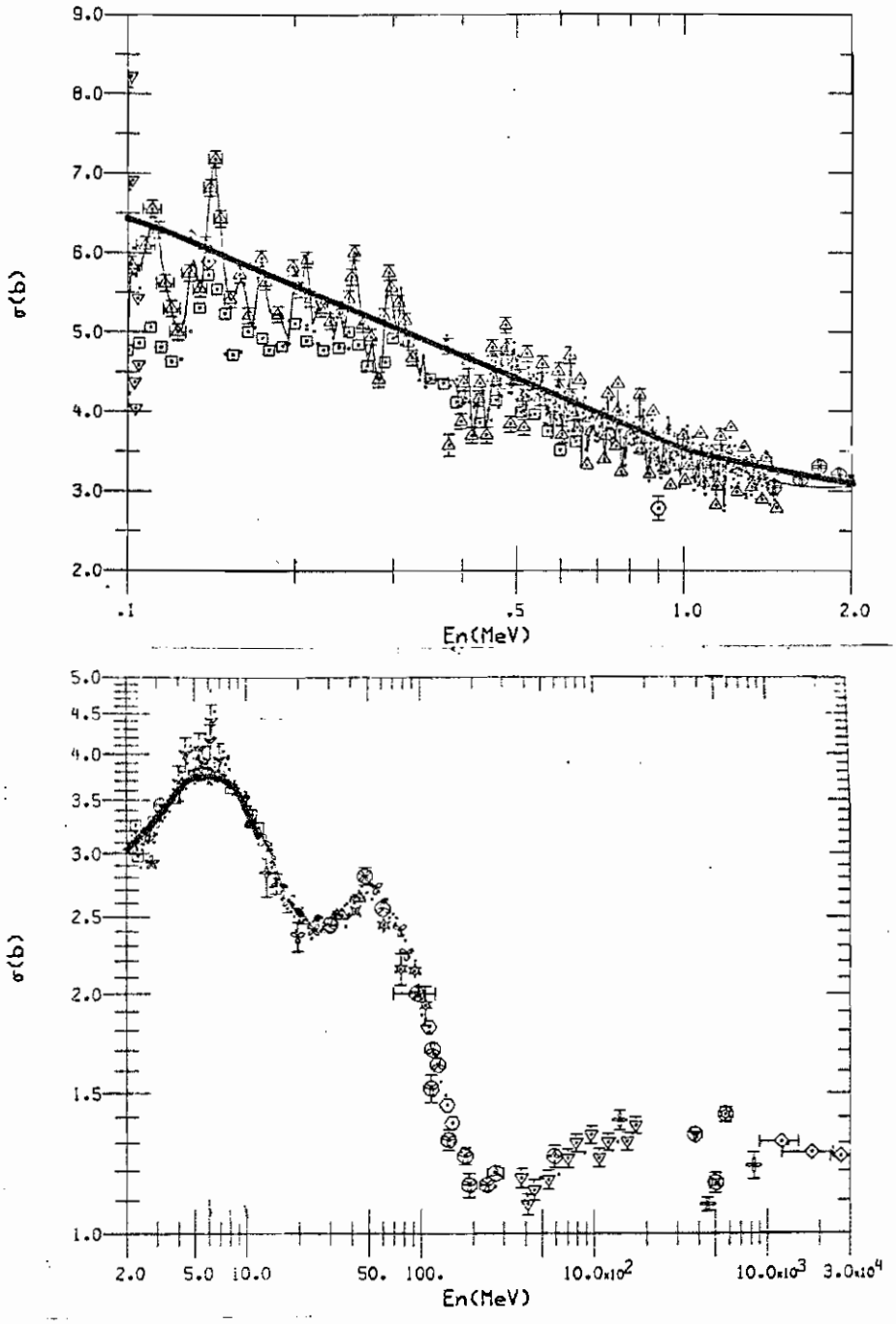

Figure 77 Comparison between the prediction of the total cross section from present work for ^{63}Cu and the total cross section of natural Cu (see text).

value of $\beta_c . r_c$ for ^{62}Ni from Coulomb excitation, the agreement is still considered to be reasonable because of the high uncertainty on the Coulomb excitation measurments.

Chapter VI

SUMMARY

Neutron elastic and discrete inelastic scattering data were obtained for ^{54}Fe, ^{56}Fe, ^{63}Cu and ^{65}Cu in the energy range between 8 and 14 MeV. The elastic scattering was analyzed using spherical optical model. Two global sets which provided reasonably good fit to the data of the present work were obtained. Not only will these sets be useful for calculating the cross section data in the vicinity the present work, but they also provide more information on OM parameters in a region of the periodic table where very little solid work had been performed for 8-14 MeV neutrons.

The volume integral per nucleon (J_v/A) of the real central potential as well as its rms radius $\langle r^2_R \rangle^{1/2}$ were calculated and the matter rms radius $\langle r^2_m \rangle$ were deduced from the rms radius of the central potential. The values found for these terms were in very good agreement with previous work.

Coupled channels (CC) calculations were performed for ^{54}Fe and ^{56}Fe to fit the elastic as well as inelastic scattering to the low-lying 2^+ excited state. The fits achieved were reasonably good. The quadrupole deformation parameters

obtained were in agreement with corresponding values from Coulomb excitation. The weak particle-core coupling scheme was assumed for analyzing the data of the Cu isotopes. Good fits were also obtained and the quadrupole deformation parameters were found to be comparable to previous results for neighboring Ni isotopes.

An extension of the work reported here would be to study the coulomb correction terms in the optical potential. This is usually done by converting the optical parameters obtained here to a proton parameters and fitting the proton data in the mass and energy ranges of the present work. Such a comparison may also provide information about the magnitude of the quadrupole deformation parameters as seen with proton and with neutrons.

Appendix A

NEUTRON CROSS SECTIONS DATA FOR ^{54}FE, ^{56}FE, ^{63}CU AND ^{65}CU.

Each page of the table gives center of mass values at two energies. The order is: scattering angle in degrees, $d\sigma/d\Omega$ in mb/sr, and percent error. The data sets included here for 12 MeV for ^{63}Cu and ^{65}Cu supersede those shown in the figures of the thesis. For these two listed sets, the values in the first minimum are noticeably larger and at the back angles are slightly larger; the error bars have been increased for these data in these angular regions.

54Fe			Elastic		
E(MeV)	7.96			9.94	
29.650	835.190	4.4	29.610	633.320	4.6
34.480	487.810	4.3	34.400	363.260	5.0
39.300	304.950	4.6	39.210	185.210	5.5
44.110	143.220	5.0	44.040	81.890	5.6
48.830	66.930	5.1	49.010	31.390	7.0
53.570	25.180	6.2	54.390	10.470	8.0
58.960	6.970	8.1	60.260	5.650	8.4
66.140	3.870	12.5	65.890	5.820	7.8
71.510	7.710	7.3	71.120	6.770	7.2
76.140	10.110	6.1	76.150	9.280	6.9
80.870	12.420	5.6	81.100	11.340	6.5
85.720	13.720	5.6	86.010	12.870	5.0
90.640	13.540	5.6	90.890	15.060	5.4
95.590	13.780	5.5	95.770	15.190	5.8
100.520	14.000	5.0	100.600	15.570	5.7
105.390	12.840	5.0	105.400	14.870	5.7
110.220	12.630	5.0	110.180	11.840	5.9
115.000	10.410	6.5	114.970	9.170	5.3
119.740	7.500	6.5	119.840	6.620	5.4
124.560	4.770	6.5	124.940	3.910	5.9
129.740	2.770	6.8	130.380	2.780	5.9
135.490	2.280	7.0	135.900	3.270	5.8
140.930	3.390	6.9	141.100	4.880	5.5
145.890	5.940	6.7	145.970	8.700	5.2
150.700	8.880	6.5	150.670	11.840	5.6
155.490	12.670	5.6	155.260	15.000	7.5

54Fe			Elastic		
E(MeV)	11.93			13.92	
29.450	404.040	5.3	27.350	395.630	7.5
34.210	218.240	5.8	29.020	314.510	8.0
39.080	91.060	6.3	34.040	128.120	8.0
44.280	40.170	6.8	39.590	50.130	8.9
49.920	18.800	6.8	45.430	34.020	9.0
55.210	13.740	7.3	50.460	33.900	9.2
59.960	11.680	7.9	54.970	30.700	9.2
64.770	6.260	7.8	59.650	18.800	8.8
70.710	3.920	8.4	65.000	8.700	9.8
76.730	6.670	7.0	71.370	7.590	13.0
81.600	12.090	6.5	76.550	14.420	9.8
86.210	15.360	7.1	81.300	18.110	8.9
90.870	16.800	6.9	85.870	23.270	8.5
95.600	18.120	6.9	90.640	22.480	7.5
100.410	17.330	6.4	95.430	18.410	8.0
105.260	12.050	6.5	100.260	14.430	6.6
110.130	10.020	7.1	105.120	10.850	8.5
115.030	7.860	6.7	110.160	8.360	8.0
120.120	5.490	6.9	115.320	5.020	12.0
125.570	4.240	7.2	120.640	5.540	7.2
130.970	5.100	7.2	125.790	7.130	8.5
135.910	7.290	7.8	130.790	7.580	7.2
140.610	9.580	6.5	135.540	9.400	8.2
145.300	10.130	6.4	140.470	9.080	11.5
150.120	10.890	6.0	145.440	10.580	12.3
155.200	10.730	6.8	150.190	9.850	10.6

54Fe		Inelastic			
E(MeV)	7.96			9.94	
30.180	16.370	15.4	30.180	12.620	15.5
35.140	10.740	14.7	35.120	10.600	15.5
40.130	10.620	15.2	40.090	6.710	15.6
45.180	6.980	15.9	45.140	5.680	14.5
50.240	6.460	15.1	50.210	4.060	14.6
55.370	5.240	12.4	55.380	3.000	13.6
60.540	2.990	16.5	60.620	2.510	14.3
65.660	4.570	11.7	65.800	2.640	13.2
70.700	5.210	11.0	70.890	2.900	12.4
75.700	4.150	11.9	75.880	3.690	11.8
80.690	4.670	11.3	80.830	3.430	12.0
85.670	4.790	10.9	85.760	2.970	12.7
90.640	4.720	11.9	90.690	2.890	12.7
95.610	4.140	11.3	95.650	2.800	12.9
100.610	4.100	11.8	100.650	2.430	12.2
105.610	3.780	12.0	105.690	2.490	12.9
110.640	3.820	13.1	120.750	2.380	13.0
115.660	4.030	11.3	125.790	2.500	12.9
120.660	4.840	11.1	120.800	2.570	12.9
125.610	4.820	10.6	125.760	2.870	12.4
130.530	5.760	10.2	130.670	3.280	12.9
135.430	5.460	11.1	135.530	3.460	13.0
140.290	5.690	10.7	140.370	3.850	12.8
145.110	5.880	10.4	145.180	3.660	13.0
149.920	5.720	10.9	149.970	3.180	12.1
154.700	4.740	14.5	144.720	3.060	14.0

54Fe		Inelastic			
E(MeV)	11.93			13.92	
30.160	14.990	13.2	29.980	13.500	22.5
35.120	14.950	16.5	35.030	9.740	22.5
40.140	9.530	16.3	40.040	6.200	16.0
45.180	7.490	15.1	45.130	4.620	17.0
50.290	4.900	14.3	50.320	4.000	17.0
55.430	4.740	15.2	55.550	2.390	22.0
60.570	4.020	15.8	60.660	2.540	16.0
65.680	3.730	15.8	65.750	1.850	20.0
70.750	3.370	15.6	70.770	2.810	17.0
75.750	3.810	15.8	75.800	2.120	20.0
80.740	2.780	14.7	80.820	2.700	15.0
85.710	3.590	15.3	85.830	2.600	18.0
90.680	2.820	13.5	90.820	2.460	17.9
95.650	3.100	13.5	95.750	3.130	20.0
100.620	2.270	13.6	100.710	2.310	15.0
105.600	2.580	14.6	105.520	1.960	20.0
110.590	1.970	14.3	110.540	2.000	15.0
115.600	2.250	13.1	115.340	1.850	20.0
120.610	2.050	14.3	120.120	1.880	20.5
125.620	2.090	13.3	125.540	1.340	20.5
130.600	2.130	14.1	130.630	1.600	16.9
135.540	2.620	14.7	135.680	1.820	19.5
140.440	2.430	14.4	140.360	1.980	17.0
145.320	2.890	15.6	145.270	2.290	20.0
150.170	2.610	14.8	150.040	2.140	15.0
154.990	2.710	15.0	155.680	1.920	17.0

56Fe			Elastic		
E(MeV)	7.96			9.94	
29.840	822.100	4.5	29.670	644.420	5.1
34.600	477.590	4.6	34.420	359.070	5.3
39.430	274.740	4.5	39.160	177.040	5.6
44.190	136.390	5.5	43.890	77.680	5.6
48.880	63.210	5.6	48.760	29.530	6.2
53.560	22.230	5.9	54.330	7.860	7.6
59.520	4.770	8.0	60.620	4.810	8.4
66.610	5.880	7.7	65.990	5.860	7.1
71.520	10.550	5.6	70.990	7.520	7.1
76.150	14.290	5.6	76.040	8.700	7.0
80.880	17.080	5.3	81.060	10.990	7.0
85.710	17.460	4.9	85.980	13.530	4.8
90.610	17.390	4.9	90.840	15.350	4.8
95.540	17.120	4.8	95.670	16.610	4.8
100.470	15.690	4.7	100.500	16.490	4.8
105.360	15.050	4.8	105.330	14.620	4.8
110.180	13.120	4.5	110.170	12.720	4.8
114.940	10.380	4.5	114.960	10.870	4.9
119.650	7.070	4.3	119.730	7.520	5.2
124.440	4.220	5.6	124.580	4.760	5.4
129.850	2.370	5.5	129.990	2.500	5.7
135.940	2.240	6.1	135.930	2.880	6.5
141.220	4.660	4.9	141.150	5.410	5.3
145.990	9.020	4.5	145.810	9.810	6.0
150.700	12.630	4.6	150.320	13.580	5.3
155.420	17.640	5.5	154.700	15.030	6.3

56Fe			Elastic		
E(MeV)	11.93			13.92	
29.580	402.010	5.4	29.180	303.780	5.6
34.300	223.470	5.4	34.110	113.540	6.4
39.120	97.660	6.3	39.690	49.280	6.9
44.270	43.340	7.1	45.460	35.510	6.9
49.850	18.370	7.7	50.420	33.290	7.7
55.130	14.460	7.9	55.020	26.690	8.1
59.940	9.420	7.7	59.650	14.630	7.6
64.980	6.130	10.0	64.920	6.880	11.0
71.110	4.060	11.1	71.240	6.460	11.4
76.750	8.510	9.4	76.570	12.880	8.5
81.490	13.830	7.3	81.240	18.930	7.1
86.110	18.510	6.8	85.870	24.230	6.4
90.790	19.200	6.4	90.560	22.140	6.2
95.530	19.820	6.5	95.310	18.100	5.8
100.330	17.920	6.8	100.140	13.750	7.7
105.200	12.750	7.2	105.120	9.700	9.4
110.130	10.520	8.6	110.270	7.510	15.3
115.140	7.530	9.7	155.440	5.960	15.1
120.240	6.260	11.0	120.510	5.730	14.9
125.440	5.240	11.3	125.530	6.240	11.4
130.650	5.830	11.4	130.530	7.830	16.0
135.690	7.420	9.4	135.470	8.870	14.0
140.530	9.580	8.7	140.300	9.540	13.3
145.300	10.450	8.2	145.070	9.790	12.0
150.130	11.410	8.1	149.890	10.890	16.3
155.120	11.890	12.7	154.920	12.700	14.5

56Fe Inelastic

E(MeV)	7.96			9.94	
45.950	13.060	16.0	50.410	9.420	17.1
50.650	13.620	16.8	55.500	8.190	17.4
55.380	9.550	16.1	60.580	6.910	19.8
60.370	9.430	16.3	65.630	6.210	21.7
65.590	7.710	16.5	70.650	6.310	17.6
70.840	8.670	15.5	75.640	6.630	17.6
75.890	8.270	15.7	80.600	6.770	17.5
80.770	9.470	15.7	85.550	6.210	17.7
85.630	9.870	15.4	90.510	5.180	18.0
90.540	9.210	15.5	95.470	5.310	17.9
95.540	8.450	15.8	100.460	4.650	18.0
100.590	8.760	15.9	105.460	3.930	18.1
105.620	7.330	15.7	110.510	4.250	20.9
110.590	8.060	15.5	115.530	3.160	22.7
115.550	8.090	15.9	120.550	3.520	18.2
120.530	8.430	15.9	125.540	4.500	17.6
125.510	8.570	15.3	130.490	5.570	17.2
130.460	9.180	15.5	135.370	5.540	20.1
135.330	9.460	16.0	140.250	5.850	20.0
140.160	9.060	15.3	145.100	5.010	20.3
145.000	8.880	15.5	149.940	5.320	22.6
149.970	8.610	15.5	154.770	7.200	19.7
155.130	8.210	16.0			

56Fe			Inelastic		
E(MeV)	11.93			13.92	
50.280	9.030	19.7	50.340	7.150	25.0
55.400	8.550	19.5	55.530	4.550	21.0
60.520	6.100	22.5	60.680	4.960	21.0
65.630	5.800	22.0	65.750	4.410	22.0
70.760	5.830	19.0	70.750	5.680	22.4
75.810	6.300	17.0	75.710	4.650	22.0
80.780	6.020	17.7	80.640	5.250	21.9
85.670	6.550	17.8	85.580	3.120	22.8
90.550	4.830	17.5	90.530	3.710	23.1
95.450	4.890	18.7	95.500	3.970	22.9
100.420	3.740	18.2	100.480	4.000	21.2
105.470	3.780	18.0	105.470	2.820	20.0
110.540	2.870	22.4	110.440	1.950	21.5
115.570	3.250	21.9	115.390	1.720	24.4
120.540	3.050	19.9	120.310	2.290	20.0
125.500	2.940	19.5	125.250	1.730	22.9
130.490	3.540	19.9	130.260	1.870	30.8
135.500	3.510	19.8	135.380	0.940	30.0
140.450	4.130	17.6	140.550	1.040	30.0
145.280	4.710	17.0	145.610	2.080	30.0
149.970	4.910	17.0	150.540	2.300	20.0
154.500	4.750	23.5	155.340	2.530	20.0

63Cu	elastic				
E(MeV)	7.96			9.94	
29.540	897.530	5.3	29.330	722.630	5.7
34.240	493.750	5.4	33.990	392.630	6.4
38.890	288.550	7.5	38.630	203.400	8.5
43.440	120.040	9.4	43.260	78.520	9.2
47.990	41.460	12.0	48.220	19.210	11.5
54.300	5.750	13.2	55.260	5.390	12.3
61.990	10.850	12.5	61.320	9.880	10.3
66.570	22.220	9.5	66.010	13.210	9.8
71.000	30.550	7.2	70.800	14.980	7.2
75.630	35.840	6.2	75.680	17.580	7.1
80.370	35.570	6.2	80.540	19.220	7.0
85.180	32.510	6.3	85.380	19.400	7.0
90.040	27.120	6.5	90.200	18.850	7.0
94.940	21.780	6.5	95.020	16.170	7.0
99.900	17.140	6.5	99.870	13.670	7.1
104.900	10.810	7.5	104.800	9.950	7.2
109.910	9.290	7.5	109.860	7.240	7.2
117.600	7.510	7.6	115.060	6.350	7.5
119.880	6.070	7.6	120.290	6.110	8.0
124.960	4.420	7.5	125.400	6.590	8.0
130.260	4.370	7.7	130.380	7.640	7.8
135.650	5.070	7.5	135.270	8.580	7.6
140.820	6.930	7.5	140.140	9.440	7.6
145.730	11.200	7.2	145.070	10.210	7.4
150.510	14.500	7.0	150.070	11.090	7.4
155.240	19.310	6.9	155.090	13.430	7.2

63Cu	Elastic				
E(MeV)	11.93			13.92	
29.320	453.350	8.2	28.540	334.360	8.7
33.960	233.740	8.6	33.520	94.620	9.5
38.630	92.930	8.1	39.750	31.730	11.3
43.530	39.310	16.8	45.330	31.200	14.3
49.270	10.170	24.5	49.870	24.410	18.6
55.080	8.530	17.4	54.310	20.200	16.9
60.240	5.830	16.0	59.210	9.300	16.5
65.720	5.660	25.3	65.900	3.450	18.0
71.440	7.070	11.4	71.860	9.690	17.8
76.450	11.480	8.6	76.450	15.480	15.6
81.110	18.190	10.6	80.890	21.320	11.5
85.690	22.330	9.9	85.330	22.240	13.5
90.300	19.450	9.6	89.770	17.160	11.4
94.950	15.950	9.6	94.250	9.680	13.0
99.720	11.660	10.9	99.310	5.700	15.2
104.770	7.840	12.4	105.720	2.870	18.4
110.270	5.100	12.8	111.120	4.880	18.4
115.690	7.000	12.6	115.770	7.800	20.0
120.700	7.750	12.4	120.560	7.870	11.6
125.610	9.400	15.0	125.480	8.840	15.3
130.460	10.730	14.0	130.260	9.280	17.3
135.250	11.270	13.0	134.860	9.190	13.1
140.110	11.820	12.5	139.630	8.080	19.1
144.910	10.930	14.5	145.110	6.110	19.3
150.720	10.690	12.3	150.350	6.580	16.9
154.590	9.080	13.1	153.810	7.260	19.3

63Cu	Inelastic				
E(MeV)	11.93			13.92	
49.690	9.830	24.0	51.600	6.080	29.7
55.240	7.180	24.0	56.240	5.200	34.2
60.690	5.810	23.1	60.700	6.290	38.8
65.780	6.810	24.4	65.350	7.650	41.9
70.700	7.790	20.4	70.240	8.890	33.8
75.590	10.000	19.1	75.480	7.480	33.4
80.490	7.180	18.5	80.840	5.100	30.5
85.420	6.710	20.2	85.940	6.980	33.6
90.370	6.740	19.5	90.790	9.050	32.2
95.330	6.790	21.4	95.530	9.920	29.5
100.280	5.410	19.9	100.240	7.340	31.6
105.230	4.230	18.2	104.960	6.920	29.7
110.170	4.530	18.2	109.740	4.570	35.3
115.140	2.940	26.4	114.750	2.890	34.4
120.150	4.040	18.2	120.110	3.040	32.1
125.230	2.630	32.5	125.480	3.440	33.1
130.380	2.680	30.5	130.480	2.580	35.6
135.500	3.370	33.3	135.250	2.280	31.5
140.510	3.530	22.4	140.060	3.150	31.8
145.430	4.400	24.5	145.160	3.420	30.5
150.300	5.170	22.5	150.520	3.730	34.0
155.130	6.070	22.5	155.690	5.100	33.0

63Cu Inelastic

E(MeV)	7.96			9.94	
50.280	10.570	18.5	49.940	8.310	19.2
55.290	8.830	19.1	55.140	5.540	19.6
60.310	7.080	18.0	60.380	4.850	19.8
65.400	8.050	19.2	65.530	4.320	20.1
70.480	6.660	19.3	70.590	4.820	19.9
75.550	6.440	19.5	75.570	5.070	19.8
80.580	7.340	18.3	80.490	6.160	18.0
85.550	7.510	18.0	85.410	5.670	19.8
90.490	6.620	19.1	90.330	5.530	20.0
95.400	7.530	18.8	95.240	4.630	20.3
100.320	7.050	18.2	100.180	4.420	20.0
105.260	5.050	19.0	105.140	3.980	18.1
110.240	5.950	18.5	110.120	3.370	18.5
115.270	5.650	18.0	115.130	2.950	20.9
120.320	4.730	18.5	120.170	2.940	20.8
125.330	4.930	18.8	125.200	2.720	20.8
130.300	4.660	19.4	130.220	3.020	20.3
135.210	5.330	19.5	135.210	2.800	20.5
140.110	5.510	18.1	140.170	3.130	20.4
145.010	5.090	19.1	145.110	3.650	19.9
149.920	4.970	19.6	150.000	3.680	20.5
154.830	5.300	19.6	154.850	4.130	19.7

65Cu	Elastic				
E(MeV)	7.96			9.94	
29.520	930.710	5.0	29.340	712.730	5.3
34.260	504.780	5.1	34.000	380.870	5.6
38.970	302.550	7.5	38.600	182.000	7.2
43.600	127.080	9.5	43.180	66.590	8.5
48.260	48.850	12.5	48.350	14.210	12.2
54.630	8.350	14.5	55.760	4.210	15.0
61.840	17.020	13.5	61.370	9.220	12.4
66.440	27.970	9.5	65.980	14.380	8.5
70.910	39.010	7.5	70.760	16.620	7.4
75.530	41.250	6.5	75.690	21.190	6.5
80.300	40.440	6.2	80.590	22.940	5.6
85.130	37.440	6.5	85.420	22.830	5.6
90.000	32.590	6.5	90.200	23.390	5.7
94.900	24.520	6.5	94.970	20.550	5.7
99.840	19.680	7.0	99.790	16.090	5.9
104.850	13.770	7.5	104.750	11.180	7.0
109.940	11.870	7.8	109.960	8.530	7.2
115.000	9.280	8.0	115.290	8.170	7.5
119.960	8.310	8.2	120.440	8.850	7.5
124.930	7.050	8.8	125.400	10.130	7.2
130.110	5.980	8.9	130.290	11.120	7.0
135.500	6.140	8.9	135.220	11.800	7.0
140.700	8.470	8.9	140.190	12.890	6.8
145.640	12.930	7.5	145.150	14.550	6.5
150.510	16.230	7.5	150.050	16.300	6.2
155.380	23.600	6.5	154.860	18.520	6.0

65Cu	Elastic				
E(Mev)	11.93			13.92	
29.320	466.100	6.5	28.690	372.770	13.5
33.900	249.600	7.6	33.580	120.280	13.6
38.520	93.170	8.0	39.140	45.250	13.9
43.400	37.970	15.0	44.850	22.520	14.5
49.500	8.340	20.0	49.870	20.980	14.9
55.500	9.150	18.8	54.680	12.660	12.2
60.520	6.850	9.7	59.970	9.650	13.2
65.780	8.100	8.0	65.980	6.640	18.1
71.250	10.800	10.0	71.490	14.600	21.0
76.250	16.840	7.4	76.250	20.500	17.6
80.940	22.200	6.0	80.800	24.850	16.0
85.540	25.930	5.9	85.320	29.140	15.2
90.130	22.140	6.4	89.810	22.680	15.0
94.770	19.860	6.9	94.290	14.440	15.2
99.560	10.960	7.6	99.230	9.260	15.5
104.860	7.790	9.7	105.300	3.350	16.2
110.550	6.180	10.0	110.930	6.290	15.8
115.830	8.610	10.0	115.720	7.520	18.5
120.700	10.790	9.8	120.490	8.340	17.5
125.500	12.160	9.0	125.350	9.970	17.6
130.330	12.360	7.7	130.180	9.850	18.4
135.240	13.770	8.0	134.810	7.740	18.5
140.000	12.260	8.4	139.630	7.390	19.4
144.830	12.690	8.0	145.210	5.260	25.0
149.970	11.000	8.0	150.580	7.490	25.0
155.320	13.140	8.0	154.710	7.490	25.0

65Cu	Inelastic				
E(MeV)	7.96			9.94	
45.090	9.510	21.0	45.620	7.610	23.6
50.150	8.380	21.0	50.660	7.400	23.5
55.240	6.860	21.1	55.730	5.320	24.1
60.340	5.250	23.0	60.790	4.600	24.2
65.420	5.290	21.2	65.860	4.050	24.1
70.490	6.020	21.0	70.890	3.750	24.1
75.510	4.750	21.6	75.880	4.500	23.8
80.510	4.960	21.1	80.860	4.610	23.8
85.490	4.180	21.0	85.820	4.660	23.7
90.450	5.430	21.0	90.780	3.570	23.5
95.390	5.290	21.0	95.730	3.420	24.6
100.330	5.560	20.5	100.680	2.910	24.4
105.260	4.390	21.0	105.630	2.830	24.4
110.200	4.420	20.4	110.580	2.300	25.0
115.160	3.390	23.0	115.550	1.990	25.5
120.140	4.150	21.4	120.540	2.360	25.0
125.150	3.070	22.7	125.530	2.190	24.9
130.180	3.680	22.0	130.500	2.320	24.4
135.180	3.390	22.0	135.430	2.400	24.6
140.140	3.350	20.0	140.330	2.730	24.3
145.060	4.140	22.0	145.210	3.040	24.0
149.940	3.710	21.0	150.080	3.270	24.5
154.760	4.100	20.3	154.910	4.030	23.5

65Cu	Inelastic				
E(MeV)	11.93			13.92	
49.840	8.330	22.5	49.530	7.490	33.8
55.140	7.000	25.0	54.980	6.290	34.3
60.300	5.520	21.4	60.570	3.320	31.8
65.340	5.130	21.0	65.830	5.030	33.0
70.360	5.100	21.0	70.830	5.790	26.0
75.430	5.240	22.0	75.680	5.600	31.8
80.520	6.370	20.0	80.510	8.060	31.4
85.600	5.750	20.0	85.370	3.970	30.8
90.550	4.440	21.0	90.340	5.640	31.7
95.530	4.210	21.0	95.180	3.870	33.2
100.310	4.690	21.0	100.290	3.440	28.9
105.250	3.200	25.0	105.280	6.070	33.1
110.660	3.300	20.0	110.310	2.660	32.1
115.330	1.690	30.0	115.300	3.950	30.3
120.620	2.550	24.4	120.320	4.640	31.0
125.650	1.920	24.0	125.160	1.860	33.3
130.500	3.320	22.0	130.170	3.030	31.1
135.010	3.000	22.4	135.190	3.250	33.9
140.260	3.660	21.5	140.290	3.250	34.3
145.100	4.300	33.0	145.370	5.010	34.9
149.960	5.280	20.4	150.380	3.660	32.6
154.840	4.600	30.0	155.260	5.670	32.6

Appendix B

LEGENDRE POLYNOMIAL COEFFICIENTS FOR IRON AND CU ISOTOPES OF THE PRESENT WORK

54Fe

Elastic

E (MeV)	7.96	9.94	11.93	13.92
a0	150.108	133.815	105.529	93.294
a1	383.967	343.362	267.687	227.554
a2	530.739	489.700	388.306	336.081
a3	556.499	539.297	444.196	383.448
a4	493.122	51.395	439.999	409.865
a5	343.533	395.311	366.750	356.110
a6	216.079	279.265	278.530	301.524
a7	109.948	174.289	196.924	223.743
a8	48.0767	88.987	117.081	167.249
a9	18.700	39.997	51.046	80.626
a10	6.818	13.372	16.692	34.186
a11		3.683		

Inelastic

a0	6.385	4.534	4.853	3.764
a1	4.719	4.463	5.889	4.506
a2	6.867	5.890	6.459	5.260
a3	6.484	5.658	5.003	4.901
a4	4.144	3.942	3.752	4.188
a5	3.943	3.360	2.005	1.870

63cu

Elastic

E (MeV)	7.96	9.94	11.93	13.92
a0	166.984	149.138	130.838	104.980
a1	419.650	383.067	337.440	407.549
a2	582.018	549.033	499.141	407.549
a3	627.247	610.234	577.589	470.087
a4	598.216	591.526	586.326	523.903
a5	449.493	475.002	507.441	476.296
a6	281.867	331.144	390.512	433.832
a7	141.840	196.775	268.239	325.627
a8	62.173	102.685	175.207	272.404
a9	24.703	36.768	81.367	164.441
a10	6.217	8.824	27.473	96.431
a11				29.051
a12				13.853

Inelastic

a0	9.743	7.688	7.677	6.459
a1	10.442	10.007	6.932	4.367
a2	10.822	11.039	6.386	2.735
a3	9.740	9.813	3.868	2.211
a4	7.399	8.708	6.479	5.723
a5	3.371	3.830	2.189	0.998

65Cu

Elastic

E (MeV)	7.96	9.94	11.93	13.92
a0	172.475	153.709	134.495	115.350
a1	421.350	389.413	340.380	288.687
a2	580.991	564.143	505.924	436.711
a3	607.872	635.562	582.593	507.486
a4	576.037	626.334	598.655	559.076
a5	408.145	516.326	516.047	501.070
a6	244.261	367.847	399.895	438.274
a7	95.584	231.900	267.550	318.481
a8	28.930	130.766	178.827	259.297
a9		58.165	83.339	153.021
a10		18.969	28.425	85.363
a11		6.612		25.452
a12		2.658		15.231

inelastic

a0	6.628	5.585	7.883	6.642
a1	6.119	6.389	10.274	6.853
a2	6.134	6.969	11.991	8.017
a3	4.684	4.704	8.701	5.928
a4	3.854	4.654	8.851	6.624
a5	0.685	1.956	4.211	2.725

56Fe

Elastic

E (MeV)	7.96	9.94	11.93	13.92
a0	155.283	133.789	112.385	97.509
a1	395.728	338.940	283.575	242.944
a2	548.294	485.814	413.524	356.199
a3	583.103	535.955	472.298	418.039
a4	526.958	510.846	472.605	442.068
a5	379.128	394.269	392.101	401.807
a6	241.355	280.093	300.190	338.367
a7	135.275	174.966	210.134	273.117
a8	62.109	89.592	129.605	203.672
a9	32.017	41.827	56.941	123.308
a10	11.760	15.974	19.059	58.018
a11	4.057	5.815		22.073
a12		3.189		7.151
a13				3.941

Inelastic

a0	12.060	8.846	7.965	6.634
a1	9.546	9.787	9.499	10.292
a2	11.616	11.492	10.291	11.378
a3	11.277	8.505	7.252	9.499
a4	7.256	6.997	6.621	9.989
a5	5.127	4.72	3.600	4.727
a6				2.916

BIBLIOGRAPHY

Allen B. J., Musgrove A. R. de L., Boldeman J. W. and Macklin R. L. Nucl.Phys. A283(1977)37

Bechetti F. D. and Greenlees G. W. Phys.Rev. 182(1969)1190

Beyerle A. G. et al. Nuclear cross sections for technology ed. Fowler J. L., Johnson C. H. and Bowman C. D., NBS SP 594 p537.

Beyerle A. G. Unpublished PhD dissertation, North Carolina State University (1980).

Borkowski F., Simon G. G., Walther V. H., and Wendling R. D.

Boyd R. N., Fenton J., Williams M., Kruse T. and Savin W. Nucl.Phys. A162(1971)497 Z.Physik A 275(1975)29

Brissaud I. Nucl.Phys. A 191(1973)145

Byrd R. Unpublished PhD dissertation Duke University (1978) and private communication.

De Jager C. W., De Vries H., and De Vries C. Atomic Data and Nuclear Data Tables volume 14, number 5-6 p479.

Delaroche J. P., Lagrange Ch. and Salry J. Nuclear Theory in Neutron, in Nuclear Data Evaluation (IAEA, Vienna, 1976), Vol. II,p.251

Delaroche J. P. private communication 1980

De Shalit A. Phys. Rev. 108(1957)1300

Drosg M. Nuc.Inst.Meth. 105(1972)573

Drosg M. Nuc.Sci.Eng. 67(1978)190

Dukarevich Yu. V., Dyumin A. N. and Kaminkev D. M. Nucl.Phys. A92(1967)433

Eastgate R. J., Thompson W. J. and Hardekopf R. A. Comp.Phys.Commun. 5(1973)69

Ferrer J. C., Carlson J. D. and Rapaport J. Nucl.Phys. A 275(1977)325

Feshbach H. Ann.Rev.Sci. 8(1958)49

Finlay R. W. et al. Private communication 1980

Floyd C. Private Communication 1980

Glasgow D. W., Velkley D. E., Brandenberger J. D., McEllistrem M. T., Henneck H. J. and Breitenbecher D. V. Nucl.Inst.Meth. 114(1974)521

Glendinning S. G. Elastic and inelastic neutron scattering cross-sections for ^{10}B, ^{11}B and ^{16}O unpublished PhD dissertation, Duke University (1980).

Greenlees G. W., Pyle F. G. and Tang Y. C. Phys.Rev. 171(1968)1115

Guss P. G. et al. Private Communication 1980

Hodgson P. E. Nuclear reaction and nuclear structure Clarendon Press. Oxford 1971

Hogue H. H. Elastic and inelastic scattering of fast neutrons by ^{6}Li, ^{7}Li, ^{9}Be and ^{12}C unpublished PhD dissertation, Duke University (1977).

Holmqvist B. Ark.Fys. 38(1968)403

Holmqvist B. and Weilding T. Atomenergi,Studsvik, Sweden, Report AE-303 (1967)μ BNL 400, TID-4500 (1970)EANDC(us)-138 ''U''.

Holmqvist B. and Wielding T. Nucl.Phys. A 188(1972)24

Kenney W. E. Nuc.Inst.Meth. 83(1970)103

Kumar K. In the Electromagnetic Interaction in Nuclear Spectroscopy, ed. Hamilton W. D. (North Holland, Amsterdam,1975) p.55

Leshchenko B. E., Gurtovoi M. E., Kukhlenko A. S., and Strizhak V. I. Excitation of collective states of some medium nuclei by 14-Mev neutrons Soviet Journal of Nuclear Physics Volume 15, Number 1(1972)5

Levine M. J., Warburton E. K. and Schwalm D. Phys. Rev. C Volume 23 No 1(1981)244

Liskien H. and Paulsen H. Nuclear Data Tables, Vol. 11, No 7, 1973

McCarthy and Crawley G. M. Phys.Rev. 150(1966)935

Menet J. J. H. et al. Phys.Rev. C4(1971)1114

Negele J. W. Phys.Rev C1(1970)1260

Newson H. W., Bilpuch E. G., Purser F. O., Boyce J. R. and Clegg T. B. Nucl.Inst.Meth. 122(1974)99

Perey F. G. Phys.Rev. 131(1963)745

Perey C. M. and Perey F. G. Atomic Data and Nuclear Data Tables 13(1974)293

Rapaport J., Cheema T. S., Bainum D. E., Finlay R. W. and Carlson J. D. Nucl.Phys. A296(1978)95

Rapaport J., Cheema T. S., Bainum D. E., Finlay R. W. and Carlson J. D. Nucl.Phys. A313(1979)1

Rapaport J., Kulkarni V. and Finlay R. W. Nucl.Phys. A330(1979)15

Raynal J. Private communication 1980

Seagondollar L. W. et al. Nuclear cross sections for technology ed. Fowler J. L., Johnson C. H. and Bowman C. D., NBS SP 594 p537

Stelson P. H. and Grodzins L. Nuclear Data Section A Volume 1 Number 1(1966)21

Thomas G. L., Cinha B. C. and Duggan F. Nucl.Phys. A 203(1973)305

Velkley D. E., Brandenberger J. D., Glasgow D. W. and McEllistrem M. T. Nuc.Inst.Meth. 129(1975)231

Watson B. A., Singh P. P. and Segel R. E. Phys.Rev. 182(1969)977

Wilmore D. and Hodgson P. E. Nucl.Phys. 55(1964)673

Tamura T. Rev.Mod.Phys. Volume 37, Number 4(1965)679